A lensless approach to EUV metrology with a high harmonic generation source and its experimental challenges

Weerdenburg, S.

DOI
10.4233/uuid:a01b7649-0e6c-47a7-ad28-c4befc674fbe

Publication date
2025

Document Version
Final published version

Citation (APA)
Weerdenburg, S. (2025). *A lensless approach to EUV metrology with a high harmonic generation source: and its experimental challenges*. [Dissertation (TU Delft), Delft University of Technology]. https://doi.org/10.4233/uuid:a01b7649-0e6c-47a7-ad28-c4befc674fbe

Important note
To cite this publication, please use the final published version (if applicable).
Please check the document version above.

A LENSLESS APPROACH TO EUV METROLOGY WITH A HIGH HARMONIC GENERATION SOURCE

AND ITS EXPERIMENTAL CHALLENGES

A LENSLESS APPROACH TO EUV METROLOGY WITH A HIGH HARMONIC GENERATION SOURCE

AND ITS EXPERIMENTAL CHALLENGES

Proefschrift

ter verkrijging van de graad van doctor
aan de Technische Universiteit Delft,
op gezag van de Rector Magnificus prof. dr. ir. T.H.J.J. van der Hagen,
voorzitter van het College voor Promoties,
in het openbaar te verdedigen op 10 februari 2025 om 17.30 uur

door

Sven WEERDENBURG

Master of Science in Applied Physics,
Technische Universiteit Delft, Nederland,

geboren te Zoetermeer, Nederland.

Dit proefschrift is goedgekeurd door de

promotor: Prof. dr. W.M.J.M. Coene
promotor: Em. prof. dr. H.P. Urbach

Samenstelling promotiecommissie:

Rector Magnificus,	voorzitter
Prof. dr. W.M.J.M. Coene,	Technische Universiteit Delft, promotor
Em. Prof. dr. H.P. Urbach,	Technische Universiteit Delft, promotor
Onafhankelijke leden:	
Prof. dr. A. Mosk	Universiteit Utrecht, Netherlands
Dr. ir. C.L. Porter,	ASML Research, Netherlands
Prof. dr. M.D. Ackermann	Universteit Twente, Netherlands
Dr. Y. Ekinci,	Paul Scherrer Institute, Switzerland
Prof. dr. ir. J. Hoogenboom,	Technische Universteit Delft, Netherlands
Prof. dr. S. Stallinga,	Technische Universiteit Delft, reservelid

Keywords: EUV microscopy, Ptychography, Lensless imaging, High Harmonic Generation, Metrology, Semiconductors, Phase retrieval, Automatic differentiation

Printed by: proefschriftenprinten.nl

Cover: S. Weerdenburg (**Front**: Photo of the EUV light source, **Back**: a ptychographic reconstruction of a full semiconductor die.)

ISBN 000-00-0000-000-0

An electronic version of this dissertation is available at
http://repository.tudelft.nl/.

CONTENTS

SUMMARY

With the continuously growing transistor density in the semiconductor industry, where smaller features and tighter tolerances in the nanometer scale are the norm, there is a growing demand for more advanced metrology tools during manufacturing. While optical metrology in the visible range is the main workhorse, such as scatterometry, its performance is limited by the wavelength. Moving beyond the visible spectrum to extreme ultraviolet (EUV) and soft X-ray (SXR) wavelengths promises higher resolutions, but not without challenges. In this wavelength regime traditional microscopy struggles due to the non-availability of high numerical aperture optics for EUV and SXR at reasonable costs, failing to fully make use of the potential benefits of the shorter wavelength.

This thesis covers an alternative route to traditional microscopy through advanced lensless imaging or **coherent diffractive imaging** (CDI) techniques, particularly focusing on **ptychography** within the EUV and soft X-ray ranges demonstrated on a designed EUV beamline. Before we go into details about the setup we start with the basics of diffraction, coherent imaging, and ptychography in chapter 2. In chapter 3 we cover the generation of coherent EUV and SXR light from various sources, ranging from large scale facilities like synchrotrons to table-top **High Harmonic Generation** (HHG) setups.

From this point we cover the design and construction of a table-top EUV lensless imaging beamline in chapter 4, which has been designed and built from scratch at the Optics Research Group at the Delft University of Technology as part of this thesis. This section covers the design, optimization, and assembly of the beamline tailored for lensless imaging of industry relevant samples in a reflection configuration using EUV and soft X-rays from HHG sources. The beamline is split into several subsystems, a high intensity femtosecond fiber laser, the HHG EUV source, optical components for spectral filtering and illumination, and optomechanical systems required for ptychography which are individually covered in the chapter.

In chapter 5 we demonstrate one of the first ptychography reconstructions obtained on the EUV beamline, as presented in chapter 4, by illuminating an object with EUV light at 17.3 nm and 17.9 nm in a grazing reflection orientation of 20 degrees. The object, a silicon substrate which has been patterned with a 20 nanometer thick gold layer with feature sizes from a few microns down to 15 nanometers, has been reconstructed. This reconstruction has been generated with an in-house developed ptychography algorithm, based on automatic differentiation, for the ptychography reconstruction process. The experimental results demonstrate the feasibility of achieving high resolution reconstructions. Line features down to 50 nanometers were retrieved with this method, close to the diffraction limit given an imaging NA of 0.17 at 18 nm wavelength. A reconstructed structure height of 23.6 ± 0.62 nm agrees well with the 20 nm nominal design value and the height retrieved from an atomic force microscope (AFM) measurement of 22.8 ± 1.45

nm.

The results in chapter 5 are quite promising, though there are certain challenges which need to be solved to further improve the reconstruction quality. One of these challenges are intensity stability issues which are typically associated with EUV sources based on high harmonic generation. Chapter 6 proposes a simple computational method to mitigate intensity fluctuations during ptychography scans by introducing a scanning position dependent multiplication factor. The algorithm effectively corrects for power fluctuations, enabling object reconstruction even in the presence of significant intensity variations up to 50 percent during the overall scan.

Chapter 7 presents a compact schlieren (from the German word 'streak') imaging system integrated within the HHG EUV source, enabling quantitative density retrieval of the gas jet used to drive the high harmonic generation process. Schlieren imaging provides a straightforward alternative to vibration sensitive techniques like interferometry and can be used as a standardized tool for HHG sources, allowing for a better comparison among different HHG setups and for the optimization of HHG light sources.

In summary, this thesis does not only cover the field of lensless EUV microscopy but also covers the design process of such a beamline and the challenges associated with HHG EUV sources. This work presents a starting point for experimental EUV metrology within the Optics Research Group at the Delft University of Technology and enables future academic research relevant for the semiconductor industry.

SAMENVATTING

Met de voortdurend groeiende transistor dichtheid in de halfgeleiderindustrie, waar kleinere structuren en toleranties op nanometerschaal de norm zijn, is er een groeiende vraag naar meer geavanceerde meettechnieken tijdens het productie proces. Hoewel optische metrologie met zichtbaar licht de huidige standaard is (zoals scatterometrie), wordt deze methode beperkt door de golflengte van het licht. De transitie naar het extreme ultraviolet (EUV) en zachte röntgen (SXR) straling met zijn kortere golflengtes maakt hogere resoluties mogelijk, maar niet zonder uitdagingen. In dit golflengtegebied is het erg lastig om traditionele microscopie toe te passen vanwege het gebrek aan optiek met een hoge numerieke apertuur (NA) voor een aanvaardbare prijs, waardoor niet volledig gebruik wordt gemaakt van de potentiële voordelen van de kortere golflengte.

Dit promotiewerk behandelt een alternatieve route naar traditionele microscopie via geavanceerde lensloze beeldvorming of **coherente diffractieve beeldvorming** (CDI) technieken, met name gericht op **ptychografie** binnen EUV en zachte röntgenstraling, gedemonstreerd op een nieuw ontworpen EUV/SXR opstelling. Voordat we ingaan op de details van de opstelling, beginnen we met de basisprincipes van diffractie, coherente beeldvorming en ptychografie in hoofdstuk 2. In hoofdstuk 3 behandelen we de generatie van coherente EUV en zachte röntgenstraling uit verschillende bronnen, van grootschalige faciliteiten zoals synchrotronbronnen tot compacte bronnen gebaseerd op **generatie van hogere harmonische golflengtes** (HHG).

Met dit als basiskennis behandelen we het ontwerp en de opbouw van een tafelmodel EUV lensloze beeldvormingsopstelling in hoofdstuk 4, die - volledig nieuw, "vanaf nul- is ontworpen en gebouwd bij de Optics Research Group aan de Technische Universiteit Delft als onderdeel van het promotieonderzoek. Dit gedeelte behandelt het ontwerp, de optimalisatie en de assemblage van de opstelling voor lensloze beeldvorming van voor de industrie relevante objecten in een reflectieconfiguratie met behulp van EUV en zachte röntgenstraling van HHG bronnen. De opstelling is onderverdeeld in verschillende subsystemen waarvan een hoog vermogen femtoseconde glasvezellaser, de HHG EUV bron, optische componenten voor spectrale selectie en belichting, en optomechanische systemen die nodig zijn voor ptychografie. Elk subsysteem wordt afzonderlijk behandeld in het hoofdstuk.

In hoofdstuk 5 tonen we een van de eerste ptychografie reconstructies die verkregen is op de EUV opstelling, zoals besproken in hoofdstuk 4, door een object te belichten met EUV licht bij 17.3 nm en 17.9 nm in reflectie onder een hoek van 20 graden ten opzichte van het oppervlak. Het object, een silicium substraat met een gestructureerd 20 nanometer dikke laag goud waarvan structuren variëren van grootte van een paar micrometers tot 15 nanometer, is gereconstrueerd via ptychografie. Deze reconstructie is gegenereerd met een ptychografie algoritme gebaseerd op automatische differentiatie. De experi-

mentele resultaten demonstreren reconstructies met een hoge resolutie. Met deze methode zijn lijnen tot 50 nanometer afgebeeld dichtbij het diffractie-limiet is met een NA van 0.17 bij een golflengte van 18 nm. Met deze methode was het mogelijk om de laag dikte van het goud te meten met als resultaat een dikte van 23.6 ± 0.62 nm. Dit komt goed overeen met de verwachtte waarde van 20 nm en een referentie meting met een atomaire kracht microscoop (AFM) waar een waarde van 22.8 ± 1.45 nm is gevonden.

De resultaten in hoofdstuk 5 zijn veelbelovend, maar er zijn bepaalde uitdagingen die moeten worden opgelost om de kwaliteit van ptychografie reconstructies verder te verbeteren. Een van deze uitdagingen is de instabiliteit van de brondie typisch zijn voor EUV bronnen gebaseerd op hoge harmonische generatie. Hoofdstuk 6 stelt een eenvoudige computationele methode voor om de effecten van intensiteitsfluctuaties tijdens ptychografie scans te verminderen door een scanningspositie afhankelijke vermenigvuldigingsfactor te introduceren in het reconstructie algoritme. Het algoritme corrigeert deze fluctuaties, waardoor een reconstructie zelfs mogelijk is met significante variaties in de intensiteit tot 50 procent tijdens de gehele ptychografie scan.

Hoofdstuk 7 demonstreert een compacte schlieren (van het Duitse woord 'streep') beeldvormingssysteem geïntegreerd in een HHG EUV bron, waarmee de druk in een gas jet van een hoog harmonische generatie EUV bron kan worden gemeten. Een schlieren methode is een simpel alternatief voor trillings gevoelige technieken zoals interferometrie. Daarnaast kan deze methode worden gebruikt als een gestandaardiseerde methode voor optimalisatie van HHG bronnen en om verschillende HHG opstellingen met elkaar te kunnen vergelijken.

Dit promotiewerk gaat dus niet alleen over lensloze EUV microscopie, maar ook over de uitdagingen die gepaard gaan met HHG EUV bronnen en het ontwerpproces van een dergelijke opstelling, ook wel "EUV beamline"genoemd. Dit werk biedt een startpunt voor experimentele EUV metrologie binnen de Optics Research Group aan de Technische Universiteit Delft en maakt toekomstig academisch onderzoek mogelijk dat relevant is voor de halfgeleiderindustrie.

1

INTRODUCTION

1

1.1. IMAGING AND MICROSCOPY

Imaging and microscopy have a long history dating back to around 700 BC. A piece of rock crystal found in Assyria (modern-day Iraq), also called the Nimrud lens, is speculated to be one of the first optics used as a magnifying lens [1]. Taking a giant leap from 700 BC to the 16th century, Dutch spectacle makers Hans and Zacharias Janssen invented the first compound microscope [2].

Meanwhile, not much later in Delft, Antoni van Leeuwenhoek invented a new single-lens microscope with an impressive 270 times magnification. This innovation marked the beginning of microbiology. He made significant discoveries with this microscope, including blood cells, various freshwater micro-organisms, spermatozoa, and bacteria [3]. From this point, many improvements were made to the microscope, both optically and mechanically.

In 1873, Ernst Abbe (while working for Carl Zeiss) established the concept of the physical resolution limit in imaging systems due to diffraction [4]. He formulated that the smallest feature, denoted as r, is approximately equal to the wavelength λ of the illumination source. This relation is furthermore influenced by the opening angle of the optics called the numerical aperture (NA), leading to the equation

$$r = \frac{\lambda}{2NA}, \tag{1.1}$$

also known as the diffraction limit. With the great value of microscopes, academia and industry try to reach this limit resolving even smaller details by reducing the wavelength and increasing the NA. Maximizing the resolution of optical systems is found to be quite important for the semiconductor industry.

1.2. OPTICAL METROLOGY WITH EXTREME UV FOR SEMICONDUCTOR INDUSTRY

The semiconductor industry continuously pushes to miniaturize feature sizes in state-of-the-art chips and to increase transistor density on silicon wafers (following the well known Moore's Law [5]). Lithography is a crucial step in this manufacturing process that largely determines the minimum feature size. With the current industry-standard lithography techniques such as deep UV (DUV, λ = 193 nm, NA = 1.35) and extreme UV (EUV, λ = 13.5 nm, NA = 0.33), and the recent high numerical aperture (high-NA, NA = 0.55) EUV scanners from ASML, the industry is going towards structures of few nanometers (denoted as the 2-nanometer node[1]) and is projected to reach the 2 Å-node (or 0.2 nanometer) in 2036 according to Imec [6]. In order to monitor these processes requires advanced metrology techniques which must also keep up with Moore's Law.

Optical microscopy or acoustical imaging is sufficient for larger-scale metrology, such as for packaging or through-silicon vias (TSV). More advanced imaging techniques, like scanning electron microscopes (SEM) and atomic force microscopes (AFM), must be

[1] The "2-nanometer node" does not imply that the transistors are 2 nanometers in size. Typical dimensions for gate and metal pitches are approximately 48 and 21 nanometers, respectively. [5]

used to visualize smaller structures like random access, non-volatile memory (RAM and VNAND), and logic gates. The high spatial and depth resolution of an AFM comes at the cost of a slow throughput. SEMs have their limitations to retrieve 3D information (such as depth/height) from a target, therefore transmission electron microscopes (TEM) are usually used during the R&D phase of chip development to acces the third dimension. This approach however requires a destructive sample preparation through ion beam milling after which the sample is scanned with a TEM, which is a rather slow process.

Optical methods in the visible regime, such as sub-wavelength scatterometry [7], single-molecule localization methods (SMLM) [8, 9] or Stimulated emission depletion (STED) microscopy [10] can still be used to retrieve parameters below the diffraction limit and at a throughput which is ideal for the industry. However, these can only be applied to specific periodic samples with the use of prior information (Coherent Fourier Scatterometry) or require the introduction of fluorescent material (e.g. into photo-resist materials which is not a preferred way forward).

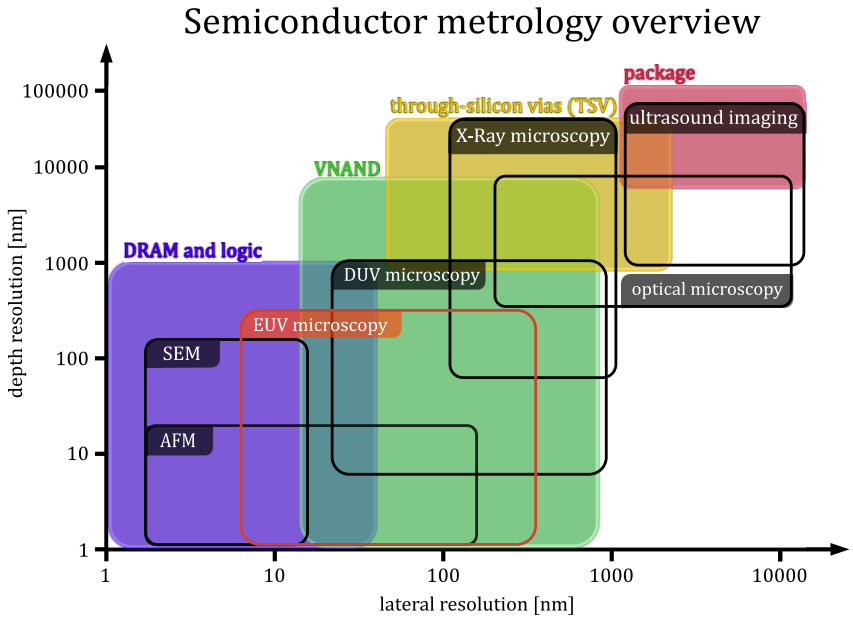

Figure 1.1: Semiconductor devices have a large range of lateral dimensions going from dynamic random-access memory (DRAM) and logic circuits [11, 12] with features in the nanometer regime, to microscopic non-volatile memory (VNAND) [13, 14], and to macroscopic semiconductor packaging [15, 16], each requiring different metrology needs. For larger-scale or high-speed applications, acoustical imaging and optical techniques such as microscopy, reflectometry, and scatterometry are typically employed. Tools like scanning or transmission electron microscopy (SEM, TEM) and atomic force microscopy (AFM) are often used at the nanoscale. Extreme UV (EUV) metrology, the main focus of this thesis, is projected to sit between these two regimes. Image reproduced from [17].

Instead, shorter wavelengths could open up the possibility of higher resolution imaging, according to Eq. 1.1. Short wavelength microscopes, such as X-ray microscopes [18–21], offer several advantages over optical microscopes, with their ability to achieve higher

imaging resolution while having decent penetration depth. Unfortunately, the refractive indices of most materials are close to one, which makes it very difficult to make high NA imaging optics for these wavelengths. Although short wavelength optics do exist, such as reflective and diffraction-based optics as will be covered in Chapter 4, having them with both high numerical aperture and throughput is very costly. Therefore the impact of using shorter wavelengths is lost for many applications.

In order to still benefit from the shorter wavelengths, we can omit the limiting imaging optics and let the light directly propagate towards a camera. Unlike conventional imaging systems, the maximum NA is now limited by the camera size (or acceptance angle) as it captures the scattered light from the object. This is specifically interesting for cases where high NA optics are not available. However, we still need a way to replace the functionality of the lens, as an image of the sample has yet to be formed. The field of lensless computational imaging or Coherent Diffractive Imaging (CDI) aims to achieve this. In this thesis, we focus on a specific type of CDI, called ptychography, to further progress on lensless imaging with EUV for industry relevant targets as will be further discussed in Chapters 2, 5 and 6.

The name, Coherent Diffractive Imaging, already implies that some form of coherent light is needed. Initially, this could only be produced using large-scale facilities like synchrotrons for the EUV and Soft X-Ray regimes. However, two significant advances in laser technology (resulting in two Nobel prizes) enabled table-top EUV light sources. With Chirped Pulse Amplification (Nobel Prize 2018 [22, 23]) and the generation of attosecond light pulses (Nobel Prize 2023 [24, 25]), it was possible to produce sufficiently coherent EUV light using High Harmonic Generation (HHG) in a relatively small form factor for the source in a ptychography-based imaging concept. This topic will be further discussed in Chapter 3.

1.3. THESIS OUTLINE

This thesis covers the development and design of a table-top EUV lensless imaging beamline at a high photon flux, targeting industry-relevant samples and addressing the associated experimental challenges. The core content of the thesis is presented in Chapters 4 to 7.

The thesis kicks off with two introductory chapters on lensless imaging in the extreme UV regime. In Chapter 2 we cover some basics of wave propagation, the phase problem, and various lensless imaging techniques. Chapter 3 introduces short wavelength sources ranging from synchrotrons to table-top High Harmonic Generation (HHG) sources.

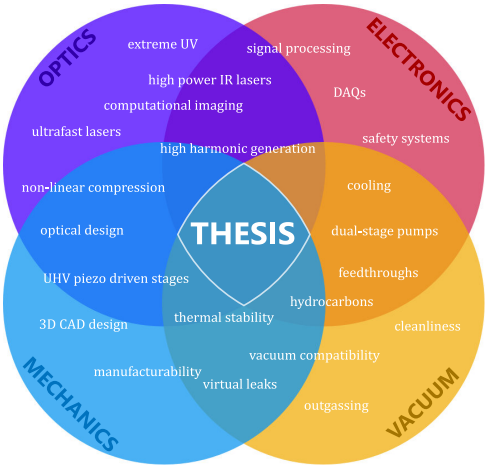

Figure 1.2: A diverse range of competences had to come together in the development of the table-top EUV lensless imaging beamline and thus in this thesis, including fields such as computational imaging, optics, signal processing, electronics, mechanics, and vacuum technology.

Chapter 4 focuses on the HHG-based EUV beamline tailored for lensless imaging. This chapter describes the process of designing, constructing, and testing the beamline from scratch. It required the integration of diverse competences, from high-power femtosecond lasers and high harmonic generation to high vacuum technology. Many competences were new to the Optics Research Group at the Delft University of Technology and had to be learned and adopted during the project.

Eventually, hardware meets software. The experimental results obtained with the reflection mode ptychography set-up are presented in Chapter 5. The processing pipeline of the data is also presented in Chapter 5, using an innovative automatic differentiation (AD) ptychography framework which has been given the name PtychoFlow[2]. PtychoFlow will be introduced in Chapter 5. Appendix C.1 demonstrates a 'gallery' of ptychography reconstructions both with EUV light and visible light using PtychoFlow.

[2]The majority of PtychoFlow's development has been carried out by Dr. Ir. Yifeng Shao (Optics Research Group, Delft University of Technology) and Dr. Ir. Jacob Seifert (Debye Institute for Nanomaterials Science, University of Utrecht) as part of the LINX project.

Chapter 6 presents a method to compensate for intensity fluctuations during a ptychography scan. High Harmonic Generation systems often have low photon fluxes, leading to lengthy experiments where source stability can become an issue. This chapter shows how a computational correction can be applied within a ptychography framework to address these issues and this concept is demonstrated on a ptychography set-up using visible light.

Finally, Chapter 7 introduces a technique to determine the density profile of a gas jet in an HHG system using schlieren imaging. Estimations of the number of atoms interacting with the laser field can be made, providing a more reproducible approach when comparing different HHG systems.

BIBLIOGRAPHY

1. De Villiers, G. & Pike, E. R. *The limits of resolution* (CRC press, 2016).
2. Haden, R. L. The origin of the microscope. *Annals of Medical History* **1,** 30 (1939).
3. Van Leeuwenhoek, A. *The select works of anthony van leeuwenhoek: containing his microscopical discoveries in many of the works of nature* (translator, 1800).
4. Abbe, E. Beitrage zur Theorie des Mikroskops und der mikroskopischen Wahrnehmung. *Archiv fur mikroskopische Anatomie* **9,** 413–468 (1873).
5. Moore, M. *et al.* International roadmap for devices and systems. *Accessed: Jan* (2020).
6. imec. *Smaller, better, faster: imec presents chip scaling roadmaps* https://www.imec-int.com/en/articles/smaller-better-faster-imec-presents-chip-scaling-roadmap [Accessed: (03-12-2023)].
7. Siaudinyte, L. & Pereira, S. F. Far-field sectioning for the retrieval of subwavelength grating parameters using coherent Fourier scatterometry. *Measurement Science and Technology* **31,** 104005 (2020).
8. Nguyen, D. T. *et al.* Super-Resolution Fluorescence Imaging for Semiconductor Nanoscale Metrology and Inspection. *Nano Letters* **22,** 10080–10087 (2022).
9. Mau, A., Friedl, K., Leterrier, C., Bourg, N. & Lévêque-Fort, S. Fast widefield scan provides tunable and uniform illumination optimizing super-resolution microscopy on large fields. *Nature communications* **12,** 3077 (2021).
10. Hell, S. W. & Wichmann, J. Breaking the diffraction resolution limit by stimulated emission: stimulated-emission-depletion fluorescence microscopy. *Optics letters* **19,** 780–782 (1994).
11. Zhu, J., Liu, J., Gu, H., Jiang, H. & Liu, S. *Optical Wafer Inspection at Advanced Technology Nodes* in *2023 Photonics & Electromagnetics Research Symposium (PIERS)* (2023), 1157–1166.
12. *KLA Axion T2000 Product Factsheet* https://www.kla.com/wp-content/uploads/KLA_Axion_T2000_ProductFactSheet.pdf [Accessed: (02-01-2024)]. KLA Tencor.
13. Zhang, W., Xu, J., Wang, S., Zhou, Y. & Mi, J. Metrology challenges in 3D NAND flash technical development and manufacturing. *J. Microelectron. Manuf* **3,** 1–8 (2019).
14. Onto. *X-Ray metrology - Aspect System* https://ontoinnovation.com/products/aspect-system [Accessed: (02-01-2024)]. Onto Innovation.
15. Bruker. *FilmTek 2000M TSV* https://www.bruker.com/en/products-and-solutions/semiconductor-solutions/filmtek-specialized-semi-solutions/filmtek-2000m-tsv.html [Accessed: (02-01-2024)]. Bruker.

16. Onto. *Acoustical metrology - Echo System* https://ontoinnovation.com/products/echo-film-metrology [Accessed: (02-01-2024)]. Onto Innovation.

17. Yang, Y. *Past, Present, and Future of Metrology and Inspection Technologies in Semiconductor* in *Samsung Electronics, IMC20 Conference, Busan, South Korea* (2023).

18. Kirz, J., Jacobsen, C. & Howells, M. Soft X-ray microscopes and their biological applications. *Quarterly reviews of biophysics* **28,** 33–130 (1995).

19. Sayre, D. & Chapman, H. X-ray microscopy. *Acta Crystallographica Section A: Foundations of Crystallography* **51,** 237–252 (1995).

20. Chao, W., Harteneck, B. D., Liddle, J. A., Anderson, E. H. & Attwood, D. T. Soft X-ray microscopy at a spatial resolution better than 15 nm. *Nature* **435,** 1210–1213 (2005).

21. Bragg, W. L. The X-ray microscope. *Nature* **149,** 470–471 (1942).

22. Strickland, D. & Mourou, G. Compression of amplified chirped optical pulses. *Optics communications* **55,** 447–449 (1985).

23. https://www.nobelprize.org/prizes/physics/2018/summary/.

24. Lewenstein, M., Balcou, P., Ivanov, M. Y., L'huillier, A. & Corkum, P. B. Theory of high-harmonic generation by low-frequency laser fields. *Physical Review A* **49,** 2117 (1994).

25. https://www.nobelprize.org/prizes/physics/2023/summary/.

2

FUNDAMENTALS OF LENSLESS IMAGING AND PTYCHOGRAPHY

This chapter covers the fundamental concepts essential for understanding lensless imaging and ptychography. It begins with an introduction to the Maxwell equations, which are the starting point for any light-material interaction. The chapter further explores field propagation, diffraction, phase retrieval algorithms, coherent diffraction imaging (CDI), ptychography, and considerations associated with lensless imaging. By the end of this chapter, readers will have a better understanding of how lensless imaging works and its potential applications.

2.1. INTRODUCTION

As mentioned in the previous chapter, an imaging technique that omits the use of imaging optics offers an alternative for wavelength regimes, such as extreme UV, soft x-rays and hard x-rays, where conventional imaging systems are not practically feasible. This chapter covers fundamental concepts essential for grasping lensless imaging, which includes field propagation, diffraction, phase retrieval algorithms, coherent diffraction imaging (CDI), ptychography, and considerations associated with lensless imaging. However, before we explore these areas, we begin at the most fundamental part of any optical problem, the Maxwell equations [1–3] as a starting point:

$$\nabla \cdot \varepsilon \mathbf{E} = 0, \tag{2.1}$$

$$\nabla \cdot \mu \mathbf{H} = 0, \tag{2.2}$$

$$\nabla \times \mathbf{E} = -\mu \frac{\partial \mathbf{H}}{\partial t}, \tag{2.3}$$

$$\nabla \times \mathbf{H} = \varepsilon \frac{\partial \mathbf{E}}{\partial t}, \tag{2.4}$$

where $\mathbf{E}$ and $\mathbf{H}$ represent the electric field and magnetic field respectively with μ and ε being the permeability and permittivity of the medium the fields reside in. Note that this is without any free charge present and μ and ε are considered constants, which implies an isotropic and non-dispersive medium.

By applying the curl operator on both sides of Eq. 2.3 (Faraday's law) and substitute the right-hand side with Eq. 2.4 (Ampère's law) we can find, after some simplification through using a vector identity [2, 4],

$$\nabla^2 \mathbf{E} - \varepsilon \mu \frac{\partial^2 \mathbf{E}}{\partial t^2} = 0, \tag{2.5}$$

but more commonly written as

$$\nabla^2 \mathbf{E} - \frac{n^2}{c^2} \frac{\partial^2 \mathbf{E}}{\partial t^2} = 0. \tag{2.6}$$

Here n is the (complex) refractive index[1] which is the square root of the relative permittivity ε_r, which equals $\varepsilon/\varepsilon_0$ with ε_0 being the permittivity of vacuum, and c being the speed of light defined by $1/\sqrt{\mu_0 \varepsilon_0}$. This equation can be recognized as the wave equation and holds for all components of E which satisfy Eq. 2.1. Therefore it can be approximated to a scalar wave equation

$$\nabla^2 \psi(\mathbf{r}, t) - \frac{n^2}{c^2} \frac{\partial^2 \psi(\mathbf{r}, t)}{\partial t^2} = 0, \tag{2.7}$$

with $\mathbf{r}$ being a point in Cartesian space (x, y, z). If $\psi(\mathbf{r}, t)$ is a time-harmonic field with angular frequency ω, it can be demonstrated that it has to follow the time-independent Helmholtz equation [2],

$$(\nabla^2 + k^2)\psi(\mathbf{r}) = 0. \tag{2.8}$$

[1] Where the real part describes phase velocity and the imaginary part absorption.

Generally speaking we talk about time-harmonic plane waves of which the electric field can be described as,

$$\psi(\mathbf{r}, t) = Be^{i[\mathbf{k}\cdot\mathbf{r}-\omega t]}, \tag{2.9}$$

with B being the fields amplitude and $\mathbf{k}$ being the wave vector whose magnitude in a medium equals $2\pi n/\lambda$. From this basis, we can proceed to wave propagation and diffraction based on these underlying principles.

2.2. WAVE PROPAGATION AND DIFFRACTION

For lensless imaging experiments our main goal is to create an image of the object using the diffraction patterns captured with a camera, as will be further discussed in Section 2.3. To make sense of it all, we need to understand how light travels from one plane to another or in terms of a lensless imaging framework, from the object to the camera.

ANGULAR SPECTRUM PROPAGATION

The angular spectrum method is a technique used in optics to describe a wavefield in space. In this method, a wavefront is decomposed into its plane wave components, each traveling at a different angle (hence the name angular spectrum), and each plane wave component is propagated separately. The wavefront at some other cross-section in the space is calculated by summing up contributions from all the plane wave components.

The angular spectrum (A) of a wave is given by the 2D Fourier transform of the wave's spatial distribution, as described in [2]:

$$A(k_x, k_y, z_0) = \int\int \psi(x, y, z_0) e^{-i(k_x x + k_y y)} \,\mathrm{d}x\,\mathrm{d}y \tag{2.10}$$

where k_x and k_y are the spatial frequencies in the x and y directions, and $\psi(\mathbf{r})$ is the wave distribution at $z = z_0$. The propagated field at distance z_1 is given by:

$$\psi(x, y, z_1) = \int\int A(k_x, k_y, z_0) e^{i(k_x x + k_y y + k_z \Delta z)} \,\mathrm{d}k_x\,\mathrm{d}k_y \tag{2.11}$$

where $\Delta z = z_1 - z_0$. Or in a simplified manner:

$$\hat{\psi}(k_x, k_y, z_1) = \hat{\psi}(k_x, k_y, z_0) e^{ik_z z}, \tag{2.12}$$

where $\hat{\psi}$ represents field ψ in frequency space which is multiplied by a factor $e^{ik_z z}$, which is called the free space propagator in reciprocal space. Propagation of the angular spectrum provides a generally applicable method to calculate the diffracted field of a wave at different positions in space along the propagation direction.

RAYLEIGH-SOMMERFELD PROPAGATION

The Rayleigh-Sommerfeld integral is based on the Huygens-Fresnel principle [5–7] where each point in the (x, y, z_0) plane emits a spherical wave. When we look at the field in a different plane at z_1 these are all added together accordingly [2],

$$\psi(x, y, z_1) = \frac{1}{i\lambda} \int\int \psi(x', y', z_0) \cos\theta \frac{\Delta z e^{ik\sqrt{(x-x')^2 + (y-y')^2 + \Delta z^2}}}{\sqrt{(x-x')^2 + (y-y')^2 + \Delta z^2}} \,\mathrm{d}x'\,\mathrm{d}y', \tag{2.13}$$

with $\cos\theta = \frac{\Delta z}{\sqrt{(x-x')^2+(y-y')^2+\Delta z^2}}$. For simplicity, we denote the term $\sqrt{(x-x')^2+(y-y')^2+\Delta z^2}$ as the distance r from here on.

FRESNEL PROPAGATION

The Rayleigh-Sommerfeld diffraction equation, Eq. 2.13, can be approximated when the propagation distance Δz of the field is sufficiently large such that difference between Δz and r becomes minimal, i.e. $\Delta z \approx r$. By following the derivations as described in [2, 8], the fraction $\Delta z/r$ in the Rayleigh-Sommerfeld integral becomes close to unity such that,

$$\psi(x,y,z_1) = \frac{1}{i\lambda\Delta z}\int\int \psi(x',y',z_0)e^{ik\sqrt{(x-x')^2+(y-y')^2+\Delta z^2}}\,\mathrm{d}x'\,\mathrm{d}y'. \tag{2.14}$$

The exponent can be further simplified through Taylor expansion to reach the Fresnel approximation ,

$$\psi(x,y,z_1) = \frac{e^{ik\Delta z}}{i\lambda\Delta z}\int\int \psi(x',y',z_0)e^{i\frac{k}{2\Delta z}[(x-x')^2+(y-y')^2]}\,\mathrm{d}x'\,\mathrm{d}y'. \tag{2.15}$$

The Fresnel integral is valid for moderate to large propagation distances.

FRAUNHOFER PROPAGATION

The exponent in the Fresnel equation, Eq. 2.15, can be further approximated for larger propagation distances. The curvature of the wavefront can be ignored in this far field regime when the term $x'^2 + y'^2$ becomes insignificant compared to Δz. This approximates to the Fraunhofer diffraction integral [8],

$$\psi(x,y,z_1) = \frac{e^{ik\Delta z}}{i\lambda\Delta z}e^{\frac{ik(x^2+y^2)}{2\Delta z}}\int\int \psi(x',y',z_0)e^{-i\frac{k}{\Delta z}(x\cdot x'+y\cdot y)}\,\mathrm{d}x'\,\mathrm{d}y'. \tag{2.16}$$

For a monochromatic field with wavelength λ in an aperture with a diameter D, then the Fraunhofer approximation is valid when $\Delta z >> \frac{D^2}{\lambda}$. The Fraunhofer diffraction integral is a rather convenient model as it behaves like a Fourier transform applied to the field at z_0, making it a very simple to implement a far field propagation model.

In conclusion, we have defined a few regimes where different propagation models for propagating waves can be used depending on the propagating distance and the required accuracy. In the remainder of the thesis we will define which propagation method is used or refer to either angular spectrum (AS) method, Fresnel propagator or Fraunhofer propagator (far field).

2.2.1. PHASE PROBLEM

When an object is illuminated by a source with a certain wavelength λ, the light gets scattered by the object which results in a scattered field very close to the object. This scattered near field (or the exit field) propagates further away from the object. Imagine that we could measure the full field $\psi(x,y)$ (i.e. both amplitude and phase) after a certain propagation distance z. In the previous section we have demonstrated that we can just propagate this measured field to any other location in space using a chosen propagator

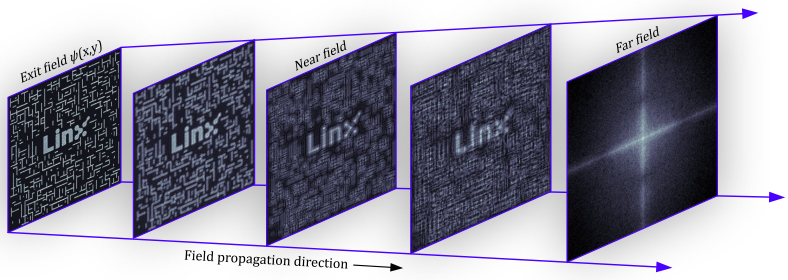

Figure 2.1: The exit field right behind the object can be propagated using different propagation models e.g. angular spectrum method, Fresnel and Fraunhofer propagation. The different planes shown are obtained by applying the Fresnel and Fraunhofer approximation on the exit field, depending on the propagation distance.

depending on the propagation distance. Back-propagation of this measured field by a distance $-z$ would retrieve the exit field (apart from the evanescent waves). If the object is thin and the first Born approximation is valid (i.e. weak scattering of the object) and the incoming field is uniform, we would be able to retrieve the object[2] directly by using back-propagation.

The most common way to measure these scattered fields (or diffraction patterns) is through a charge couple device (CCD) or a complementary metal oxide semiconductor (CMOS) camera. Unfortunately, these devices only record the intensity $|\psi|^2$ of these complex-valued diffraction patterns making the measurement incomplete. In fact, there are no devices available capable of measuring the amplitude and phase simultaneously due to the high frequencies associated with optical regime, hence only the amplitude can be retrieved. This is known as the 'phase problem' which is an underdetermined problem as we have fewer knowns (N knowns, measured intensities) than unknowns ($2N$ unknowns, the full complex field with amplitude and phase). A lot of effort has been put to try to find ways to retrieve the phase either computationally or experimentally, for example, through interferometry[3].

2.3. COHERENT DIFFRACTIVE IMAGING

A variety of phase retrieval techniques have been developed to address the phase problem, some of which we will explore in this section. Broadly speaking, phase retrieval methods can be categorized into iterative and non-iterative methods. Non-iterative methods will not be covered in this thesis and we will mainly focus on the iterative forms of phase retrieval. Notably, we will emphasize Coherent Diffractive Imaging (CDI) and

[2] In this thesis we often refer to 'the object', which in most cases should be interpreted as the 2D-spatial transmission or reflection function of the object.

[3] EUV and SXR interferometry is possible but high quality beamsplitters in this regime without high throughput losses are not readily available.

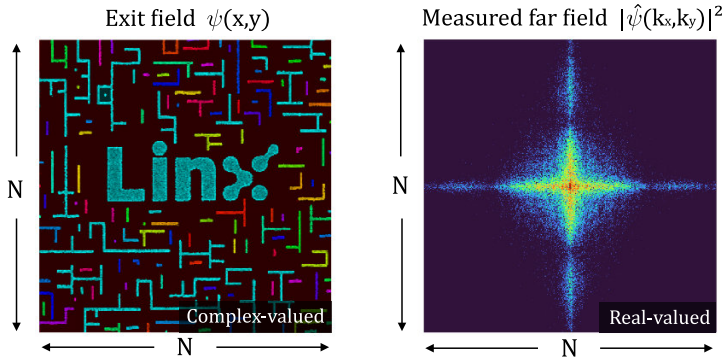

Figure 2.2: When the scattered field originating from a complex-valued object is measured we lose the phase information and only measure the amplitude. This underdetermined problem is known as the phase problem, which in this example shown in the figure is undetermined by a factor of two.

in particular on ptychography, as discussed in Section 2.4.

For the fundamental principles of CDI we start with a complex-valued transmissive object $O(x,y)$ in real space, which is assumed to be thin with respect to the wavelength to satisfy the thin sample requirement. The object is illuminated with a finite complex-valued probe $P(x,y)$. The field of the probe interacts with the object resulting in a field $\psi(x,y)$ near the object:

$$\psi(x,y) = O(x,y)P(x,y). \tag{2.17}$$

As discussed before this field can be propagated to the far field through a Fourier transform $\mathcal{F}$ of the object and the probe[4],

$$\hat{\psi}(k_x,k_y) = \mathcal{F}\{O(x,y)P(x,y)\}, \tag{2.18}$$

which can be interpreted as the convolution between the object $\hat{O}(k_x,k_y)$ and probe $\hat{P}(k_x,k_y)$ in the frequency domain,

$$\hat{\psi}(k_x,k_y) = \hat{O}(k_x,k_y) * \hat{P}(k_x,k_y). \tag{2.19}$$

In imaging problems one would like to retrieve the object one way or another. In CDI a camera measures the intensity $|\hat{\psi}(k_x,k_y)|^2$ in the far field. As stated before this leads to an underdetermined problem as there are twice as many unknowns as knowns. As pointed out by Sayre [9] in 1952, one can in principle solve this problem by oversampling the diffraction patterns as visually demonstrated in the Fig. 2.4. A camera with a relatively higher pixel density result in an extended FOV with zeroes padded around an isolated object. This way we can go from an underdetermined problem to a determined problem, enabling phase retrieval. One could also reduce the number of pixels describing the object to meet the requirement.

[4]The Fourier transform of a function is distinguished by a hat above said function, e.g. $\hat{O}$ and $\hat{P}$.

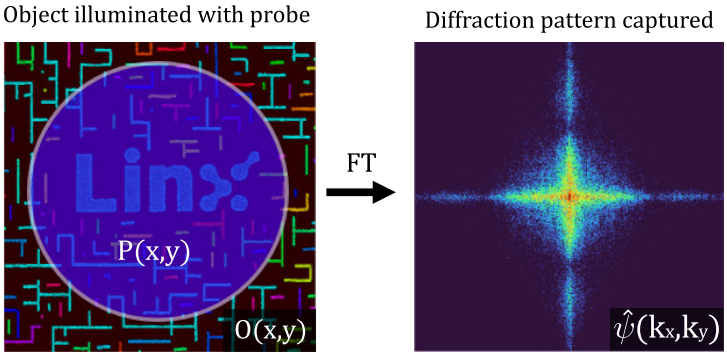

Figure 2.3: A complex-valued object function $O(x, y)$ is illuminated with a finite probe $P(x, y)$. The resulting field from the multiplication of the probe and object is propagated to the far field through a Fourier transform. In the frequency domain this could be seen as a convolution of the probe and object in reciprocal space.

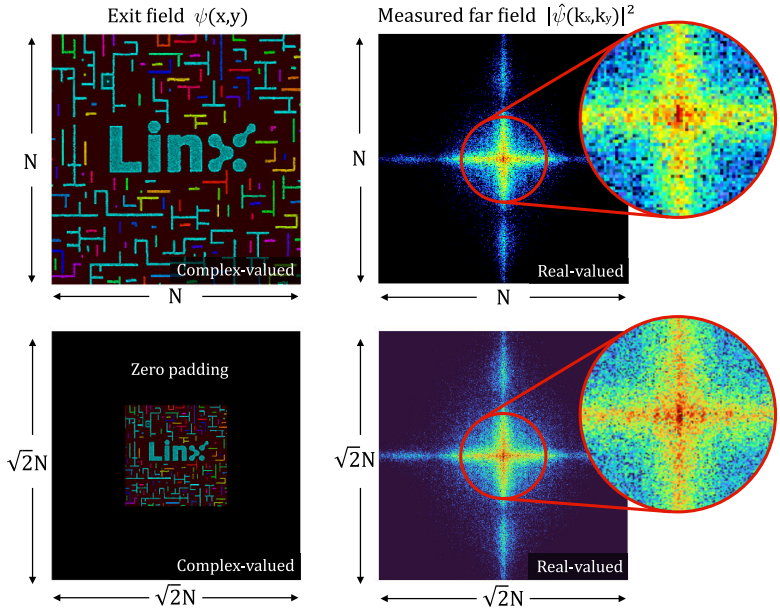

Figure 2.4: When the field $\psi(x, y)$ at the object is divided in N by N pixels we have in total N^2 complex-valued unknowns associated with the object, which translates to $2N^2$ real valued unknowns when considering amplitude and phase separately. However measuring the diffracted field, for instance in the far field, we only measure N^2 values, resulting in a underdetermined problem. One way to address this is by isolating the object (zero-padding the object) or equivalently oversampling the far-field diffraction pattern.

GERCHBERG-SAXTON ALGORITHM

In 1972 the first demonstration of a phase retrieval method was performed by Gerchberg and Saxton [10], about twenty years after Sayre pointed out to the oversampling issue. In this iterative Gerchberg-Saxton (GS) algorithm, a random initial phase of the object is

guessed as a starting point together with a measured intensity both in the object/image plane and the camera/far field plane. In simple terms the GS algorithm works accordingly,

1. Measure intensity at the image plane and far field plane.
2. Start with a random initial guess of the phase $e^{i\phi}$ for the measured intensity of far field $|\psi(x,y)|$.
3. Propagate the field back to image plane (via inverse Fourier transform).
4. Replace the retrieved amplitude by the measured amplitude of the field in the image plane.
5. Propagate the field forward to the far field plane (via Fourier transform).
6. Replace the retrieved amplitude with measured amplitude of the far field.
7. Go back to step 3.

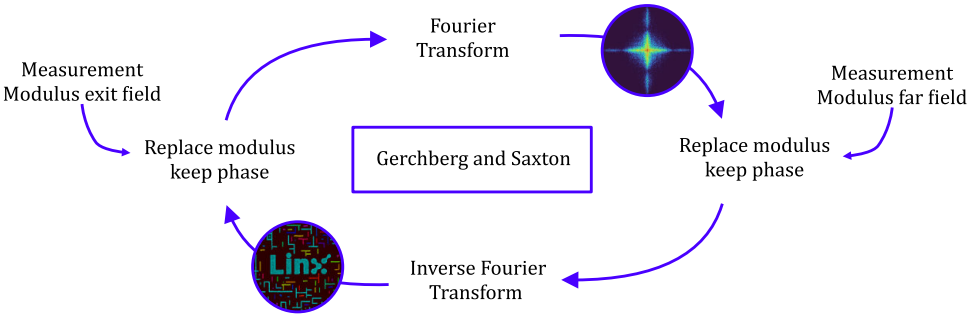

Figure 2.5: The GS algorithm starts with a measured intensity at image plane (near field/exit field) and the camera plane (far field). A random initial phase is multiplied with the amplitude (square-root) of the measured intensity in the far field. After an inverse Fourier transform we arrive at the image plane. The resulting amplitude is replaced with the measured amplitude in the image plane. After a forward Fourier transform we arrive back at the camera plane (far field), where we replace the amplitude with the measured amplitude in the far field. This process is repeated.

The Gerchberg-Saxton algorithm is usually not the best solution for a lensless microscope application, as it requires a measurement of the intensity at the image plane. In a practical application, like in EUV microscopy, this is usually unknown or not possible to measure.

ERROR REDUCTION AND INPUT OUTPUT APPROACH

In 1978, Fienup [11] continued on the Gerchberg-Saxton algorithm by introducing a significant modification to omit the need of an additional measurement in the real space of an image plane. In this modification the importance of isolating the object itself is key, often referred to as the support constraint which is defined as,

$$\psi(x,y) = 0 \quad \text{if} \quad (x,y) \notin S, \tag{2.20}$$

with S being the support function of the object which is assumed to be known. This modified GS algorithm was named Error Reduction (ER) [12]. To put it in perspective of the step-by-step pseudo algorithm, the support constraint would be applied in step 5, replacing the measurement constraint of the object intensity, i.e.

$$\psi_{k+1}(x,y) = \begin{cases} \psi_k(x,y) & \text{if} \quad (x,y) \in S \\ 0 & \text{if} \quad (x,y) \notin S \end{cases} \tag{2.21}$$

with k being the iteration number. After ER, new approaches were developed quickly with work by Rodenburg [13], Chapman [14] and Fienup himself, leading to faster convergence. A few of them being the so called input-output (IO) algorithm, hybrid input-out (HIO) and Relaxed Averaged Alternating Reflector (RAAR).

2.4. PTYCHOGRAPHY

All the CDI approaches as mentioned in the previous section are concerned with objects which are bounded and are based on a single measurement of a diffraction pattern (or two in the case for Gerchberg-Saxton algorithm as it requires the intensity at the image plane as well). This is quite effective in terms of data acquisition, but these approaches are limited in terms of robustness. On top of that for cases where the object is much larger than the probe size, it can be rather problematic to use single-shot CDI approaches. To tackle these extended objects, multiple diffraction patterns are acquired at different positions of the illuminating probe with respect to the object with the requirement that each spot is partially overlapping with a neighbouring spot. This method is called ptychography [15–18] and is the main phase retrieval method covered in this thesis.

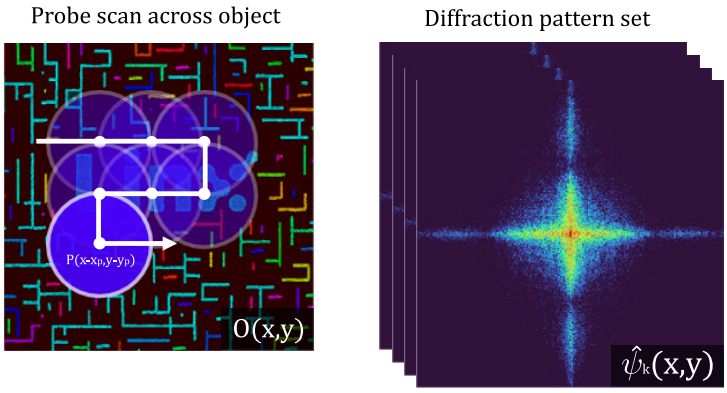

Figure 2.6: In ptychography, as opposed to traditional CDI, we collect a series of diffraction patterns. Each of these patterns stems from a distinct region of the object dictated by the probe size and probe location on the object. Every region is illuminated with a finite probe $P(x-x_p, y-y_p)$ which partially overlaps with adjacent probe locations. This partial overlap results in diffraction patterns with shared redundant information, a characteristic of ptychography that is leveraged extensively for robustness.

This approach adds a very powerful real space constraint, the overlap constraint, leading to faster algorithm convergence and an increased robustness to noise. The object

is updated at different illumination positions and these object areas are no longer independent but are linked to neighbouring scan positions as they share information in the recorded diffraction pattern, i.e. each object update benefits from the improvement of neighbouring updates. We start with Eq. 2.17 but instead we shift the probe laterally across the sample by x_p and y_p,

$$\psi(x,y) = O(x,y)P(x-x_p, y-y_p), \tag{2.22}$$

or in the far field (through a Fourier transform),

$$\hat{\psi}(k_x,k_y) = \mathcal{F}\{O(x,y)P(x-x_p, y-y_p)\}. \tag{2.23}$$

The concept of ptychography was introduced in 1969 [16, 17] by Hoppe as a technique to enhance the resolution in electron microscopy. Twenty years later it was shown, through deconvolution via a Wigner distribution approach, that reconstruction of an aperiodic structure is possible [13, 19, 20]. A few years later, Rodenburg [21] and Chapman [14, 22] revisited and demonstrated this idea using transmission electron microscopy (TEM). Nowadays, ptychography is a matured technique for scanning TEMs (STEM) reaching resolutions down to the regime of few tens of picometers [23].

2.4.1. PTYCHOGRAPHICAL ITERATIVE ENGINE AND ITS EXTENSIONS

In 2004, the group of Rodenburg proposed a new improved iterative method based on a gradient descent, called "Ptychographic Iterative Engine" (PIE) [24]. This method has many extensions with ePIE [25] being one of the most popular implementations of ptychographic CDI. There are many PIE flavours to solve different problems such as retrieving the angle of incidence (aPIE) [26], autofocusing (zPIE) [27], multi-slice for 3D (3PIE)[28], partially coherent case (pcPIE) and so on. The overlap constraint is exploited extensively in ptychography through the redundancy in the measured diffraction patterns. This enables the optimization and retrieval of experimental parameters [29–32], as the names of the different flavours of PIE already hinted at, but also it relaxes the strict conditions and a priori knowledge which is needed in conventional CDI. However, most of these algorithms are based on the two most popular cases PIE and ePIE which we will cover briefly in this section.

The pseudo-code of ptychography is very similar to those of ER and IO but with the addition of scanning positions x_p and y_p as shown in Eq. 2.22. We take a look at a single iteration, for iteration number k, in the ptychography process at a single probe position (x_p, y_p) with a total number of scanning positions N_p:

1. Start with an initial guess of the object $O_k(x,y)$
2. At scanning position (x_p, y_p), calculate the exit field $\psi_{k,p}$ of a region of the object by using the probe $P(x-x_p, y-y_p)$,

$$\psi_{k,p}(x,y) = O_k(x,y)P(x-x_p, y-y_p). \tag{2.24}$$

3. Propagate the field to the detector plane.

4. Replace the resulting amplitude with the measured amplitude (square root of measured intensity).
5. Propagate back to the object plane.
6. Update the object according to the update function described in [24] in the area which is illuminated by the probe.
7. If p < N_p, go to the next probe position $p+1$ and return to step 2. If not, go to the next step.
8. Go to the next iteration $k+1$ and start at step 2 with the first probe position $p = 0$.[5]

In the case of PIE the illuminated field, i.e. the probe, is assumed to be known. In practice however, the field of the probe is barely known besides a rough estimate of its size. Therefore an extended version of PIE, ePIE [25], was developed to deal with this problem by including the probe $P(x, y)$ as a variable and find a solution for it at the same time, exploiting the redundant information coming from the overlap in the scanning illumination probes. In this version of PIE, which is called extended PIE or ePIE, the probe has its own update rule. This extension allows for phase retrieval with a fairly unknown imaging system, where only measurements of the diffraction patterns and an approximate knowledge of the relative scanning positions are used. With ePIE, one effectively corrects for a given aberrated probe profile that is being produced by the illumination system.

2.5. COHERENCE REQUIREMENTS FOR COHERENT DIFFRACTIVE IMAGING

The CDI method, including ptychography, requires some degree of coherence. Coherence is a measure how well a wave correlates with itself. The mutual coherence function γ of a wave $\psi(\mathbf{x}, t)$ is defined as the correlation at two points in space and two moments in time $(\mathbf{x}_0, t_0)$ and $(\mathbf{x}_1, t_1)$, which can be defined as

$$\gamma(\mathbf{x}_0, t_0, \mathbf{x}_1, t_1) = \frac{\langle \psi(\mathbf{x}_0, t_0)\psi^*(\mathbf{x}_1, t_1)\rangle}{\sqrt{\left\langle |\psi(\mathbf{x}_0, t_0)|^2 \right\rangle \left\langle |\psi(\mathbf{x}_1, t_1)|^2 \right\rangle}}, \tag{2.25}$$

where the brackets $\langle ... \rangle$ denote the statistical average. The resulting value for γ gives the degree of coherence for the field $\psi(\mathbf{x}, t)$, which ranges between 0 and 1, where $\gamma = 0$ for fully incoherent and where $\gamma = 1$ for fully coherent light. We will look at the spatial coherence and temporal coherence separately.

[5] For every iteration k, the order of the scanning positions may be scrambled in the procedure to introduce variability in the updates. This can help to avoid local minima.

2.5.1. SPATIAL COHERENCE

The spatial coherence of a light source is defined as the degree to which a wave correlates with itself in space. It is characterized by the distance over which the mutual coherence function decays, usually at a factor $1/e$ from the maximum value, which is referred to as the spatial coherence length L_c. In the context of single-frame coherent diffraction imaging (CDI), the field within the support function or $P(x, y)$ must be sufficiently spatially coherent. This means that the spatial coherence length should be larger than $\sqrt{2}D$, with D being the size of the object. This constraint can be relaxed in the case for ptychography, where D is replaced by the probe size instead of the size of the object. Additionally, ptychography can accommodate partially coherent light to some extent by leveraging multiple spatial modes, as described in [33]. This aspect will be discussed further in Chapter 5.

2.5.2. TEMPORAL COHERENCE

Temporal coherence can be found in a similar fashion compared to its spatial counterpart. It is characterized by how a wave correlates with itself over time, between t_0 and t_1 at the same position in space. The mutual coherence function decays with increasing time difference. Temporal coherence is linked to the spectral bandwidth $\Delta\lambda$ of the source. A narrower spectral bandwidth (i.e., a more monochromatic source) results in higher temporal coherence and vice versa. The temporal coherence length is proportional to $\lambda_0^2/\Delta\lambda_0$.

A non-zero spectral bandwidth results into blurring of the diffraction pattern and should be minimized such that the blurring remains within a single pixel on the CCD. Imagine two monochromatic fields with wavelength λ and $\lambda + \Delta\lambda$ respectively, which illuminate an object with size D. After interaction with the object the exit field propagates to the CCD where, according to Equation 2.16, the diffraction patterns in the far field are rescaled respectively with the wavelength.

Suppose we have a spatial frequency in the object with a given real space distance of d. For longer wavelengths, the diffraction angle related to this specific spatial frequency is smaller than for shorter wavelengths (as results naturally from Bragg's law for diffraction). Given a wavelength λ, the slightly longer wavelength $\lambda + \Delta\lambda$ is effectively a factor $(\lambda + \Delta\lambda)\lambda)$ closer to the center of the detector (assuming that the latter coincides with the specular reflection). For the largest angle as captured by the detector with N_x pixels with pixel size p_x, which equals $1/2\ N_x p_x$, this shift should be smaller than p_x, i.e.

$$\begin{aligned} \frac{1}{2} N_x p_x \Big(\frac{\lambda + \Delta\lambda}{\lambda} - 1 \Big) &\leq p_x, \\ \Delta\lambda &\leq \frac{2\lambda}{N_x}. \end{aligned} \tag{2.26}$$

Note that the number of pixels N_x is coupled to maximum diffraction angle, so we can replace $\frac{1}{2} N_x p_x$ by taking maximum diffraction angle $\theta_{\max}$ and multiply this by the dis-

tance to the camera z in order to rewrite this expression in a more generic manner,

$$\begin{aligned} z\theta_{\max}\left(\frac{\lambda+\Delta\lambda}{\lambda}-1\right) \leq p_x = \frac{\lambda z}{2D} \\ 2\theta_{\max}D \leq \frac{\lambda^2}{\Delta\lambda} \quad \Rightarrow \quad \Delta\lambda \leq \frac{\lambda^2}{2\theta_{\max}D}, \end{aligned} \tag{2.27}$$

where D is the diameter of the probe as incident on the object. The effects of the temporal coherence is quite a bit more constraining compared to the spatial coherence, as this constraint puts a limit on the size of camera ($N_x p_x$), which is directly related to the maximum obtainable resolution. That being said, polychromatic ptychography is still possible with discrete wavelengths [34–36] to some extent as will be discussed in Chapter 5.

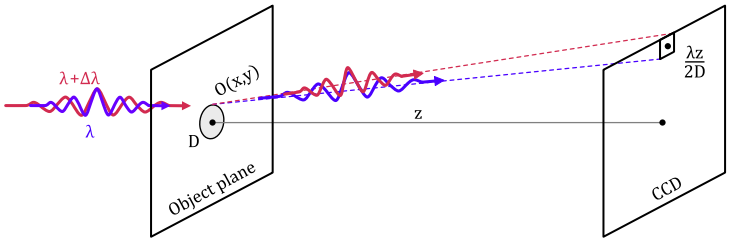

Figure 2.7: The degree of temporal coherence for the illumination source should be sufficiently low, such that the blurring caused by the spectral bandwidth $\Delta\lambda$ remains within a pixel on the camera for a CDI experiment.

2.6. GEOMETRICAL CONSIDERATIONS FOR LENSLESS IMAGING IN REFLECTION

Until now we always have assumed a normal incidence for the illumination. In reality there is a large subset of samples which are opaque for EUV light and can only be measured in a reflection orientation. This is especially true for samples one would typically find in the semiconductor industry, such as thick opaque wafers or highly reflective reticles (with multi-layer Bragg reflectors). Therefore we have to take a look at a different imaging geometry in reflection and how it impacts the measured diffraction patterns.

The interaction of light with a periodic sample can be described by using the concept of elastic scattering. Elastic scattering refers to the incident light which is scattered in the sample without any loss of energy. This means the wavelength of the scattered light remains the same as that of the incident light.

We represent the incoming beam and the scattered beam as vectors $\mathbf{k_i}$ and $\mathbf{k_s}$, respectively, with $|\mathbf{k_i}| = |\mathbf{k_s}| = 2\pi/\lambda$. Since the magnitude of $\mathbf{k_s}$ is fixed, it must lie somewhere on a sphere around the sample, also known as the Ewald sphere [37] as shown in Fig 2.8. The Ewald sphere represents all possible points which satisfy the Bragg condition [38, 39]. The edge of the Ewald sphere where the outgoing vector $\mathbf{k_o}$ intersects the sphere is set at the origin. The rotation of the sphere around this origin depend on the angle of the incoming k-vector k_i. The points where the surface of the sphere intersects the

reciprocal lattice points or rods represent the possible directions of diffraction where the diffraction conditions [39] are met.

In transmission and under normal incidence we can see (in Fig. 2.8) that the measured diffraction orders are projected on a detector plane as you would expect for a linear grating. In a reflection geometry or when we change the angle of incidence of the illumination, the position of the centre point of the Ewald sphere rotates around the origin of the reciprocal lattice (which remains fixed). This changes which reciprocal lattice points intersect with the sphere as shown in Fig. 2.9. The projection of these intersections from the Ewald sphere to the detector plane results in a non-linear mapping of the diffraction orders.

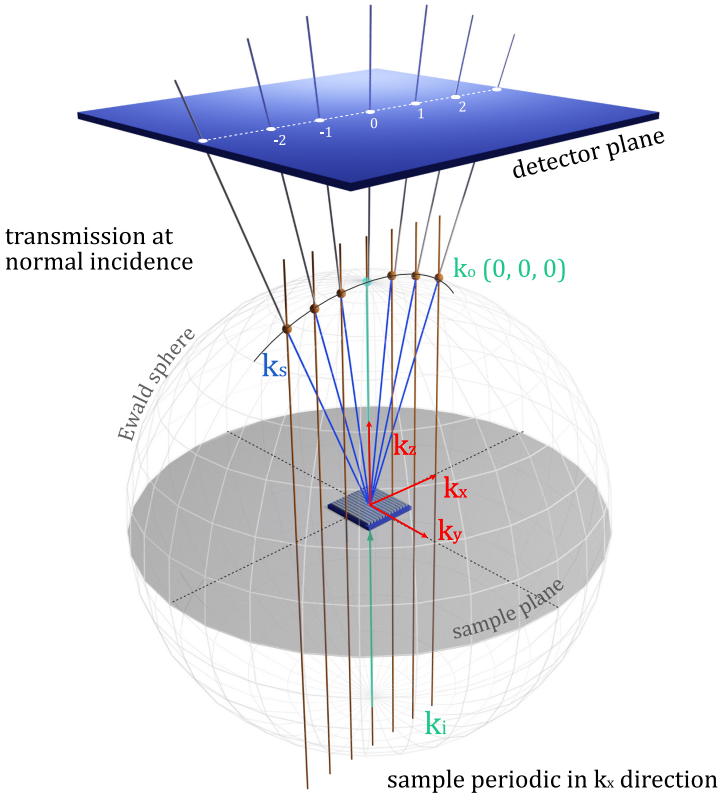

Figure 2.8: A one-dimensional periodic sample with its lines oriented in the y-direction is illuminated from below by an incident beam described by the vector k_i. In reciprocal space (Fourier space or k-space), the (infinitely thin in the z-direction) periodic structure is represented by a 1D periodic array of parallel lines (shown in brown/orange) in the (k_x, k_z) plane. The sphere around the sample, known as the Ewald sphere, represents all scattering directions and has a radius of $k = 2\pi/\lambda$. Possible scattering directions (all starting from the center of the sphere) can be measured at the points in k-space where the brown/orange lines (representing the sample in reciprocal space) intersect with the Ewald sphere. The diffraction directions originating from the center of the sphere are intersecting the flat detection plane giving rise to the recorded diffraction pattern. The vector k_o (light green) always originates from the center of the sphere and points to the origin (light green dot at the top of sphere).

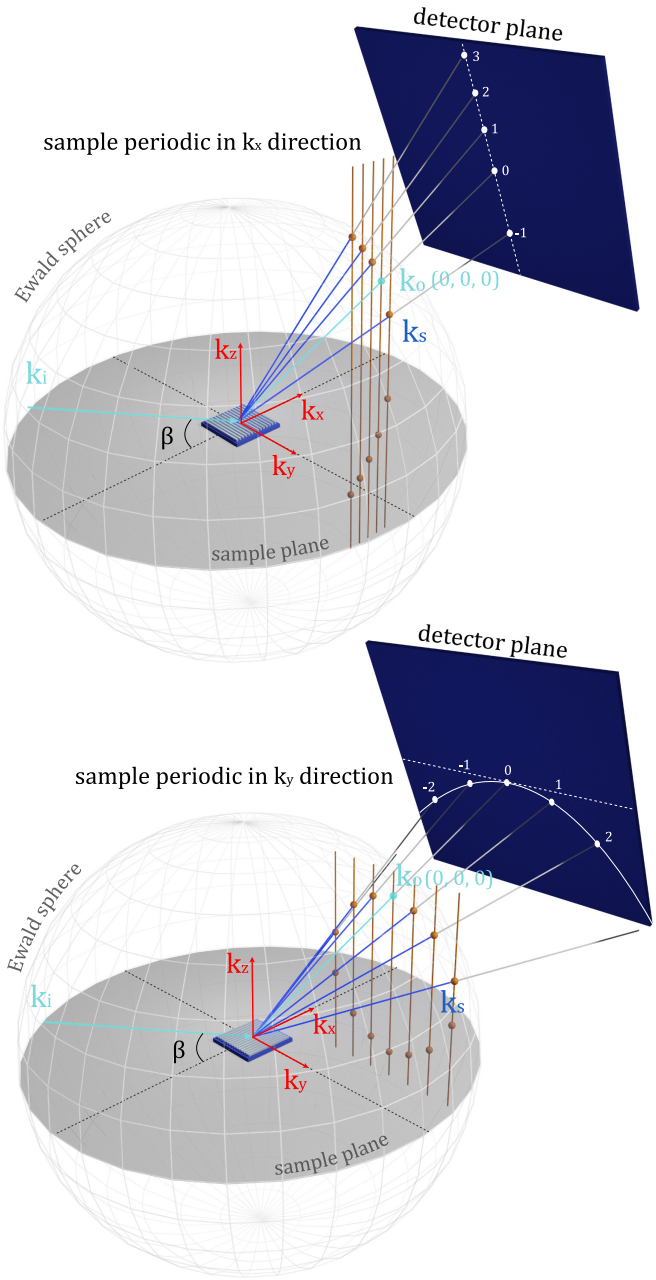

Figure 2.9: When illuminating the target at an oblique angle β (in this case, in a reflection orientation), different intersections between the Ewald sphere and the sample representation in k-space are observed. The projection of these intersections from the Ewald sphere to the detector plane results in a non-linear mapping of the diffraction orders. The bottom figure shows the same illumination geometry but with the sample rotated by 90 degrees in the (x,y)-plane.

As mentioned before, most reconstruction algorithms base their propagation model on a linearly sampled Fourier transform. This approach is not valid anymore when diffraction patterns are measured in a reflection geometry, due to the 'distortion' of diffraction patterns at oblique illumination. Therefore a non-linear interpolation is required via the rotation matrix. Here allow the sample to be rotated in three ways: titling α for rotation around the x-axis, angle of incidence β for rotation around the y-axis and azimuth γ for rotation around the z-axis,

$$R_x(\alpha)R_y(\beta)R_z(\gamma) = \begin{bmatrix} 1 & 0 & 0 \\ 0 & \cos\alpha & \sin\alpha \\ 0 & -\sin\alpha & \cos\alpha \end{bmatrix} \begin{bmatrix} \cos\beta & 0 & -\sin\beta \\ 0 & 1 & 0 \\ \sin\beta & 0 & \cos\beta \end{bmatrix} \begin{bmatrix} \cos\gamma & \sin\gamma & 0 \\ -\sin\gamma & \cos\gamma & 0 \\ 0 & 0 & 1 \end{bmatrix} \tag{2.28}$$

of which we take the inverse [40] to compute the new reciprocal coordinates. This method is often referred to as Tilted Plane Correction (TPC) in the ptychography community [26, 41–44]. Reflection-mode ptychography at relatively large angle of incidences with respect to the normal is significantly more difficult compared to the transmission case, as all three angles α, β and γ have to be known to a certain extent in order to reach an accurate representation of the mapped diffraction patterns.

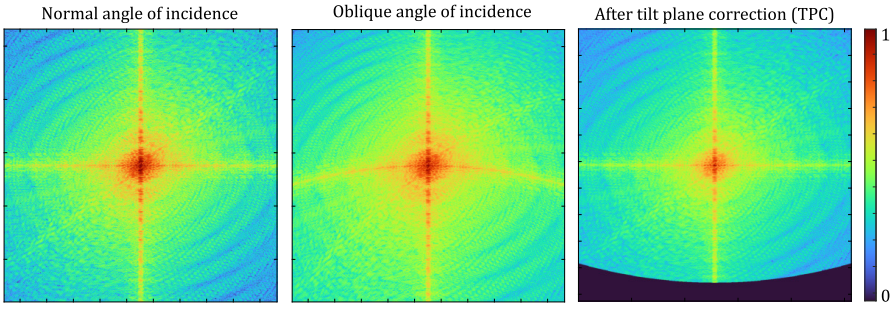

Figure 2.10: **Left:** An example of a diffraction pattern captured under normal incidence. **Center:** When a sample is illuminated under an angle we start to observe conical diffraction in the tilt direction which is observed as a distortion on a 2D flat camera. **Right:** Tilted plane correction is performed to re-map the diffraction pattern. The dark blue areas have a value of zero which are outside the detection NA of the camera after correction. This results in a reduced detection NA in the tilt direction (vertical) compared to the non-tilt direction (horizontal) when measuring in reflection.

2.7. COMMON PHASE RETRIEVAL AMBIGUITIES

In CDI methods (ptychography included) certain inherent ambiguities exist, some stemming from the Fourier characteristics of lensless imaging. Ptychography involves the product of a confined probe $P(x,y)$ and an object $O(x,y)$, as shown in Eq. 2.22. Ambiguities can pop up by, for example, a relative scaling between the probe and object, for instance, if the reconstructed values for the probe are reduced by a factor of 0.5, then the reconstructed object might need to be amplified by a factor of two to produce an equivalent diffraction pattern. This can lead to reflection or transmission functions of

the object higher than one, i.e. the retrieved values are not quantitative. The photon flux of the source can be measured before the sample to fixate the total power in the probe during reconstruction or to re-adjust it in post processing [45].

Ptychography will have a hard time reconstructing infinitely periodic structures. Note that periodic structures in this context imply objects with a pitch which is small enough that several periods are present within a single probe field. When the probe is scanned across the sample, all the diffraction patterns look identical as there is no phase information present in the measured patterns.

Periodicity in the scanning grid of the probe can also be a source of ambiguities. This could happen when, for example, a basic periodic scanning pattern is used like a raster grid scan. The resulting issue is often referred to as 'raster grid pathology' [46, 47]. This can be avoided by using non-periodic scanning patterns either by adding random noise onto each scanning position, use a Fermat spiral scan approach, or Poisson Disc sampling, see Appendix A.

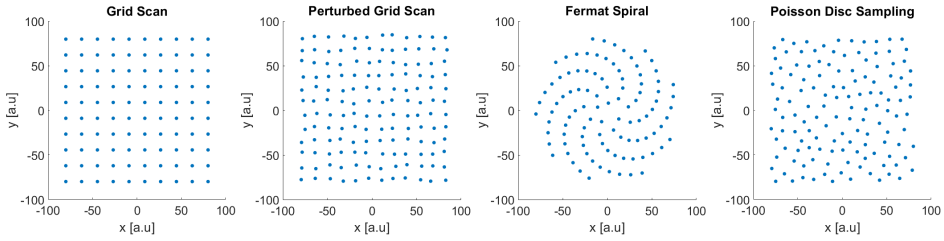

Figure 2.11: A standard grid scan can lead to artefacts in the reconstruction due to ambiguities caused by the periodicity in the scanning positions. Therefore different scanning patterns are used such as perturbed grid scan (PGS), Fermat spiral or the uniformly Poisson Disc sampling (PDS) method. Although the PGS and PDS look quite similar in this comparison, unlike PGS, PDS ensures that the average overlap between points is more uniform. This becomes more obvious if the pertubation in PGS is significantly increased.

When an object is shifted in real space it results in a linear phase ramp in Fourier space. Fortunately this ambiguity does not affect the intensity and will therefore not influence the reconstruction quality neccesarily. A resulting effect is that there are multiple solutions to the phase retrieval problem where objects can be reconstructed in a shifted position. The other way around, when the diffraction patterns are shifted, i.e. the zero order is not centered, it will result in a phase ramp in the reconstructed object. This is usually not so problematic as it can usually be removed in post processing.

BIBLIOGRAPHY

1. Maxwell, J. C. A Dynamical Theory of the Electromagnetic Field. *Philosophical Transactions of the Royal Society of London* **155,** 459–512. ISSN: 02610523. http://www.jstor.org/stable/108892 (2023) (1865).
2. Goodman, J. W. Introduction to Fourier optics. *Introduction to Fourier optics, 3rd ed., by JW Goodman. Englewood, CO: Roberts & Co. Publishers, 2005* **1** (2005).
3. Hecht, E. *Optics* 4th (Addison-Wesley, 1998).
4. Weisstein, E. *Vector Laplacian* https://mathworld.wolfram.com/VectorLaplacian.html (2023).
5. Freude, W. & Grau, G. Rayleigh-Sommerfeld and Helmholtz-Kirchhoff integrals: application to the scalar and vectorial theory of wave propagation and diffraction. *Journal of Lightwave Technology* **13,** 24–32 (1995).
6. Lucke, R. L. Rayleigh-Sommerfeld diffraction vs Fresnel-Kirchhoff, Fourier propagation, and Poisson's spot. *Defense Technical Information Center* **30** (2004).
7. Born, M. & Wolf, E. *Principles of optics: electromagnetic theory of propagation, interference and diffraction of light* (Elsevier, 2013).
8. Konijnenberg, S., Adam, A. J. L. & Urbach, H. P. *BSc Optics* (TU Delft Open, 2021).
9. Sayre, D. The squaring method: a new method for phase determination. *Acta Crystallographica* **5,** 60–65 (1952).
10. Gerchberg, R. & Saxton, W. A practical algorithm for the determination of phase from image by 103.240. 126.9 on 10/21/18. Re-use and distribution is strictly not permitted, except for Open Access articles. and diffraction plane pictures,". *Optik* **35,** 227–246 (1972).
11. Fienup, J. R. Reconstruction of an object from the modulus of its Fourier transform. *Optics letters* **3,** 27–29 (1978).
12. Fienup, J. R. Phase retrieval algorithms: a comparison. *Applied optics* **21,** 2758–2769 (1982).
13. Rodenburg, J., McCallum, B. & Nellist, P. Experimental tests on double-resolution coherent imaging via STEM. *Ultramicroscopy* **48,** 304–314 (1993).
14. Chapman, H. N. Phase-retrieval X-ray microscopy by Wigner-distribution deconvolution. *Ultramicroscopy* **66,** 153–172 (1996).
15. Rodenburg, J. M. Ptychography and related diffractive imaging methods. *Advances in imaging and electron physics* **150,** 87–184 (2008).
16. Hegerl, R. & Hoppe, W. Phase evaluation in generalized diffraction (ptychography). *Proc. Fifth Eur. Cong. Electron Microscopy*, 628–629 (1972).

17. Hoppe, W. Beugung im inhomogenen primärstrahlwellenfeld. i. prinzip einer phasenmessung von elektronenbeungungsinterferenzen. *Acta Crystallographica Section A: Crystal Physics, Diffraction, Theoretical and General Crystallography* **25,** 495–501 (1969).

18. Hoppe, W. *et al.* Trace structure analysis, ptychography, phase tomography. *Ultramicroscopy* **10,** 187–198 (1982).

19. Bates, R. & Rodenburg, J. Sub-Ångström transmission microscopy: a Fourier transform algorithm for microdiffraction plane intensity information. *Ultramicroscopy* **31,** 303–307 (1989).

20. McCallum, B. & Rodenburg, J. Two-dimensional demonstration of Wigner phase-retrieval microscopy in the STEM configuration. *Ultramicroscopy* **45,** 371–380 (1992).

21. Nellist, P., McCallum, B. & Rodenburg, J. M. Resolution beyond the'information limit'in transmission electron microscopy. *nature* **374,** 630–632 (1995).

22. Chapman, H. N. Phase-retrieval x-ray microscopy by Wigner-distribution deconvolution: signal processing. *Scanning Microscopy* **11,** 67–80 (1997).

23. Pennycook, T. J. *et al.* Efficient phase contrast imaging in STEM using a pixelated detector. Part 1: Experimental demonstration at atomic resolution. *Ultramicroscopy* **151.** Special Issue: 80th Birthday of Harald Rose; PICO 2015 – Third Conference on Frontiers of Aberration Corrected Electron Microscopy, 160–167. ISSN: 0304-3991. https://www.sciencedirect.com/science/article/pii/S0304399114001934 (2015).

24. Rodenburg, J. M. & Faulkner, H. M. A phase retrieval algorithm for shifting illumination. *Applied physics letters* **85,** 4795–4797 (2004).

25. Maiden, A. M. & Rodenburg, J. M. An improved ptychographical phase retrieval algorithm for diffractive imaging. *Ultramicroscopy* **109,** 1256–1262 (2009).

26. De Beurs, A. *et al.* aPIE: an angle calibration algorithm for reflection ptychography. *Optics Letters* **47,** 1949–1952 (2022).

27. Loetgering, L., Du, M., Eikema, K. S. & Witte, S. zPIE: an autofocusing algorithm for ptychography. *Optics letters* **45,** 2030–2033 (2020).

28. Maiden, A. M., Humphry, M. J. & Rodenburg, J. M. Ptychographic transmission microscopy in three dimensions using a multi-slice approach. *JOSA A* **29,** 1606–1614 (2012).

29. Maiden, A., Humphry, M., Sarahan, M., Kraus, B. & Rodenburg, J. An annealing algorithm to correct positioning errors in ptychography. *Ultramicroscopy* **120,** 64–72 (2012).

30. Batey, D. *et al.* Reciprocal-space up-sampling from real-space oversampling in x-ray ptychography. *Physical Review A* **89,** 043812 (2014).

31. Zhang, F. *et al.* Translation position determination in ptychographic coherent diffraction imaging. *Optics express* **21,** 13592–13606 (2013).

32. Harada, T., Nakasuji, M., Nagata, Y., Watanabe, T. & Kinoshita, H. Phase imaging of extreme-ultraviolet mask using coherent extreme-ultraviolet scatterometry microscope. *Japanese Journal of Applied Physics* **52,** 06GB02 (2013).

33. Thibault, P. & Menzel, A. Reconstructing state mixtures from diffraction measurements. *Nature* **494,** 68–71 (2013).

34. Huijts, J. *et al.* Broadband coherent diffractive imaging. *Nature Photonics* **14,** 618–622 (2020).

35. Yao, Y. *et al.* Broadband X-ray ptychography using multi-wavelength algorithm. *Journal of Synchrotron Radiation* **28,** 309–317 (2021).

36. Goldberger, D. *et al.* Spatiospectral characterization of ultrafast pulse-beams by multiplexed broadband ptychography. *Optics Express* **29,** 32474–32490 (2021).

37. Ewald, P. P. Die Berechnung optischer und elektrostatischer Gitterpotentiale. *Annalen der Physik* **369,** 253–287. eprint: https://onlinelibrary.wiley.com/doi/pdf/10.1002/andp.19213690304. https://onlinelibrary.wiley.com/doi/abs/10.1002/andp.19213690304 (1921).

38. Bragg, W. L. The X-ray microscope. *Nature* **149,** 470–471 (1942).

39. Kittel, C. & McEuen, P. *Introduction to solid state physics* (John Wiley & Sons, 2018).

40. Matsushima, K. *Introduction to Computer Holography: Creating Computer-Generated Holograms as the Ultimate 3D Image* (Springer Nature, 2020).

41. Gardner, D. F. *et al.* Subwavelength coherent imaging of periodic samples using a 13.5 nm tabletop high-harmonic light source. *Nature Photonics* **11,** 259–263 (2017).

42. Porter, C. L. *et al.* General-purpose, wide field-of-view reflection imaging with a tabletop 13 nm light source. *Optica* **4,** 1552–1557 (2017).

43. Porter, C. L. *Complex Extreme Ultraviolet Imaging Reflectometry: Quantitative Lensless Imaging with Short-Wavelength Light in Reflection Geometries* (University of Colorado at Boulder, 2019).

44. Seaberg, M. D. *et al.* Tabletop nanometer extreme ultraviolet imaging in an extended reflection mode using coherent Fresnel ptychography. *Optica* **1,** 39–44 (2014).

45. Shanblatt, E. R. *et al.* Quantitative Chemically Specific Coherent Diffractive Imaging of Reactions at Buried Interfaces with Few Nanometer Precision. *Nano Letters* **16,** 5444–5450. https://doi.org/10.1021/acs.nanolett.6b01864 (Sept. 2016).

46. Thibault, P., Dierolf, M., Bunk, O., Menzel, A. & Pfeiffer, F. Probe retrieval in ptychographic coherent diffractive imaging. *Ultramicroscopy* **109,** 338–343 (2009).

47. Huang, X. *et al.* Optimization of overlap uniformness for ptychography. *Optics Express* **22,** 12634–12644 (2014).

3

COHERENT EUV AND SOFT X-RAYS

In this chapter, we provide an overview of coherent Extreme Ultraviolet (EUV) and Soft X-Ray (SXR) light sources and its challenges. First, we cover the significant power requirements required for traditional lasers in the EUV and SXR regimes. Then we continue with the basics of large facility sources such as synchrotrons and Free Electron Lasers (FELs). From large-scale facilities we move on to more accessible, laboratory-scale setups based on High Harmonic Generation (HHG) which is driving most of the experimental work presented in this thesis.

3.1. INTRODUCTION

In the higher-energy end of the electromagnetic spectrum, we find photons ranging from Extreme UV (EUV), Soft X-Ray (SXR), Hard X-Rays (commonly referred to as just X-Rays), all the way to Gamma Rays. This thesis is concentrated on the overlap regime between the EUV and SXR bands, roughly from 18 nanometers (68 eV) to 13.5 nanometers (92 eV). A more accepted definition of the SXR regime starts at the K-edge of carbon [1] at 5 nanometers (250 eV), but within the context of this thesis, the terms EUV and SXR are considered as synonymous and are used interchangeably.

Generation or the presence of EUV light does not naturally occur on Earth due to the absorptive properties at this wavelength regime. Although it is generated by the sun in large quantities, the atmosphere does a pretty good job at protecting us from it. Specialized equipment and techniques are required to generate EUV light on Earth closed off in vacuum vessels.

One of the most successful methods for generating EUV light (specifically at 13.5 nanometers) is through the use of a laser-produced plasma (LPP) source, which is used in industrial applications such as EUV lithography for semiconductor manufacturing. In this method, for example, a tin (Sn) droplet is rapidly heated to form a plasma using a high power CO_2 laser, resulting in a broadband light source at various wavelengths, including 13.5 nm. Another source type is the so called discharge produced plasma (DPP) source where a tin vapour is generated with a (relatively) low power laser in between a cathode and anode, which is turned into a plasma to emit EUV light. While these light sources can emit high levels of power (several hundreds of Watts), the light generated is incoherent. This characteristic is not favorable for lensless imaging techniques, which requires (partially) coherent light.

When coherent light is required, the search of a light source often leads to the use of lasers, i.e. amplification through stimulated emission. First, let's start with a basic example of conventional lasing. We have an arbitrary atom in a ground state, with an associated energy E_0. The atom can be put into an excited state E_1 by putting energy into the atom either via light, electrically or chemically. Either through spontaneous or stimulated emission a photon is released putting the atom back to its ground state, as depicted in Fig. 3.1.

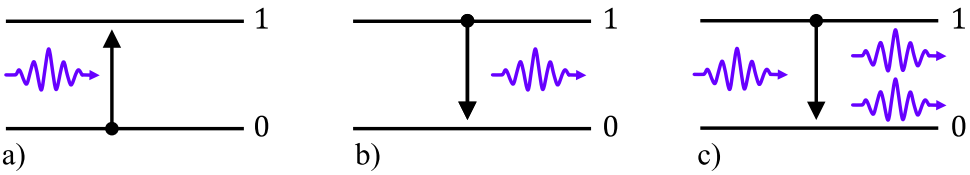

Figure 3.1: From left to right: absorption, spontaneous emission and stimulated emission of a photon by an atom.

Now, in order to get stimulated emission for EUV light, the difference in energy of the ground state and excited state of the atom must be at minimum or higher than the energy

of an EUV photon, lets say 92 eV for 13.5 nanometer. These energy ranges are more than enough to ionize the atom for valence electrons.

To achieve amplification through stimulated emission we have to ensure that the majority of atoms in a volume are pumped into an excited state first, such that the generated photons trigger other atoms through stimulated emission. This is called population inversion. Usually this is achieved by making use of fast decaying levels to (relatively) stable sub-levels, as shown in Fig. 3.2.

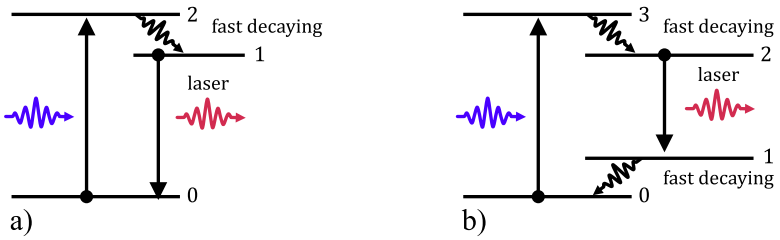

Figure 3.2: In the previous figure, a two-level system was depicted, but to achieve population inversion, three or four-level systems are needed [2]. An atom is driven to an elevated energy state and then promptly decays to a reduced energy level without photon emission, often through interactions with phonons. Following this, a lasing transition takes the atom either to the ground state (a) or an intermediate state (b), where it once again rapidly decays, ultimately reaching the ground state which allows for population inversion.

In order to maintain population inversion there is a continuous pumping power P needed. This minimum threshold power can be estimated [1] as,

$$P = \frac{\text{lasing photon energy} * \text{atoms in exicited state}}{\text{life time}} = \frac{\hbar\omega n_{\mathrm{u}} F V}{\tau}, \tag{3.1}$$

with $\hbar\omega$ being the photon energy of the emitted photon as a result of stimulated emission, n_u the amount of atoms in an exited state per unit of volume, F density inversion factor, V a gain volume and τ is the life time of the energy transition associated with the stimulated emission. Now this can be rewritten in terms of intensity, according to the theory in [3] as:

$$I = \frac{P}{A} = \hbar\omega n_{\mathrm{u}} F A_{21} L = \frac{16\pi^2 c^2 \hbar (\Delta\lambda/\lambda) G L}{\lambda^4}, \tag{3.2}$$

where the life time is replaced by the inverse of the Einstein coefficient A_{21} and the volume V is replaced by multiplication of the length L and the surface A of the gain volume and a gain factor G. Ignoring the efficiency of the pumping mechanism we can already tell that the required power scales with λ^{-4}. In this case we also ignore any influence of the spectral line width $\Delta\lambda/\lambda$, leading to a power scaling of λ^{-5}. This means that while a visible light laser might only require a few milliwatts for pumping, a continuous EUV laser would need on the order of terawatts, and for the case of X-ray lasers even petawatts.

Due to these enormous power requirements, U.S. scientists proposed utilizing nuclear warheads [4] as a pumping mechanism to create an X-Ray laser, as part of a military project called 'Project Excalibur.' In this Cold War-era project it was suggested that the nuclear bomb would be detonated in space, and the resulting x-ray laser would be directed at an enemy ballistic warhead in order to destroy them[5].

Fortunately, there was no need to detonate a nuclear bomb every time someone wants to perform an experiment with a short-wavelength laser as the Lawrence Livermore National Laboratory (LLNL) showcased the first lasing of soft x-rays at wavelengths around 20 nanometers in a Selenium plasma [6]. These x-ray lasing experiments were conducted at the Novette laser-target irradiation facility, primarily utilized for Inertial Confinement Fusion research. In order to produce soft x-rays through lasing, a peak power intensity of 5×10^{13} W cm^{-2} was required for 520 ps, on a 1.2-by-0.02 mm Selenium target, reaching the required terawatts pump power [7]. Later, experiments were performed showcasing conventional lasing in these wavelength regimes [8, 9].

3.2. LARGE-FACILITY LIGHT SOURCES

Before the experiments performed at LLNL with the facility laser Novette, in the 1940s the synchrotron principle was discovered [10]. The synchrotron was conceived by Ernest Lawrence at the Radiation Laboratory of the University of California, Berkeley, to overcome the physical size and energy limits of the cyclotron [11].

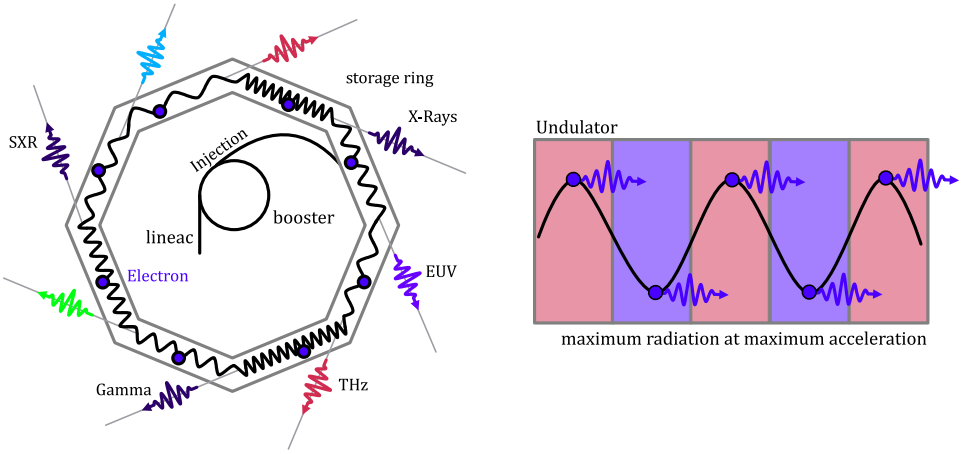

Figure 3.3: The fundamental origin of the generated light in a synchrotron (left) or a free electron laser (FEL) (right) are identical, i.e. moving electrons, the main technical difference are that electrons in a synchrotron are continuously bending and emitting light, whereas for an FEL this mainly occurs around the peaks of the trajectories of the electrons induced by the oscillating magnetic fields in an undulator/wiggler. However, newer generations of synchrotrons have undulators build into the storage ring to generate coherent light for specific wavelengths as shown in the left figure.

The working principle of a synchrotron involves several stages. First, particles, such as electrons or protons, are injected into a linear accelerator (lineac) and a booster ring where they are pre-accelerated to close to the speed of light. Then, these particles enter

the synchrotron ring (typically a circumference of several hundreds of meters) where they are further accelerated to a stable speed. As the particles travel around the ring, magnetic fields are used to keep them in a circular path. Meanwhile, electric fields are employed to accelerate the particles each time they make a full loop up to relativistic speeds. By keeping the particles in a circular path, they emit an incoherent broadband light cone along the trajectory of the relativistic particle resulting in emitted light around the entire ring. In order to get coherent light, both temporally and spatially, from these types of synchrotrons one would have to perform spatial filtering and spectral filtering via a pinhole system and gratings respectively resulting is a significant loss of brightness.

More modern iterations of synchrotrons added so called undulators and wigglers. These undulators and wigglers induce alternating magnetic fields which cause the particles to oscillate along their trajectory. The relativistic particles within the undulators emit a beam with a small divergence and narrow spectral bandwidth, whereas in wigglers the spectral bandwidth remains broad. To increase the coherence even further, it is still common practice to add spatial and spectral filters in these types of beamlines.

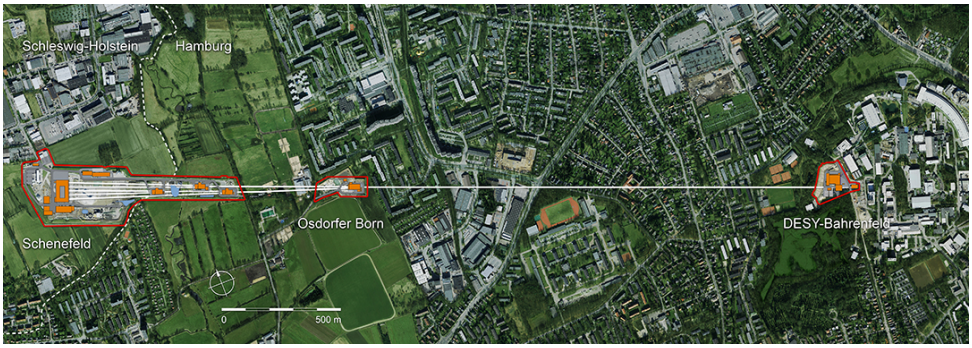

Figure 3.4: The utter scale and cost of large scale facility sources like synchrotrons and free electron lasers, make them impractical for industrial and (most) scientific applications. For example, the European XFEL, as shown in the figure, is build underground underneath Schenenfeld (Germany) near Hamburg and stretches over a 3.4 kilometers. Image source: [12]

After high-brilliance synchrotron light sources, the X-ray Free Electron Lasers (XFEL) was developed, which originated in the late 20th and early 21st centuries. The concept was theoretically proposed by John Madey in 1971 and the first operational XFEL was built at the SLAC National Accelerator Laboratory, United States, and became operational in 2009. The primary advantage of XFELs over other types of X-ray sources is their ability to produce extremely intense, short pulses of X-rays, with the brightness being billions of times greater than traditional synchrotron light sources. FELs also make use of undulators as shown in modern synchrotrons, but then hundreds of meters in size.

Both synchrotrons and XFELs are large-scale facilities and require significant resources, infrastructure and space. Synchrotrons can range from a few meters up to over a kilometer. For example, the COSAMI miniature synchotron (in the current conceptual design) at PSI is 12 meters [13] while the ESRF synchrotron has a ring circumference of approximately 850 meters [14]

XFELs, on the other hand, typically have a linear design. The length of an XFEL is primarily determined by the length of the linear accelerator used to accelerate the electrons, and the undulator section where the X-ray light is produced. XFELs can also be quite large, with lengths often measured in kilometers. For instance, the Linac Coherent Light Source (LCLS) at SLAC National Accelerator Laboratory in the United States is about 3 kilometers long [15] and the European XFEL is about 3.4 kilometers long. [16]

The large dimensions of these facilities, coupled with the high cost of construction and operation, make synchrotrons and XFELs major scientific investments, often funded by multiple countries, making them not very suitable for industrial applications. Although thousands of researchers make use of these facilities [17], they are not easily accessible for most research groups. Beam time has to be requested and accepted, allowing the researcher to perform an experiment within limited time. Thus, a tabletop short-wavelength light source would make an ideal complement to these existing large facility like light sources. Same reasoning can be applied for industrial applications.

3.3. HIGH HARMONIC GENERATION

High harmonic generation (HHG) [18–21] is one of the very few ways to generate coherent light in the EUV and SXR regime on a table-top platform, which is the reason why its application to lensless imaging is the main focus in thesis. HHG is a non-linear optical process where intense laser light is used to convert many low-energy photons into a smaller number of high-energy photons. Higher harmonics were first observed in the end of the 1970s [22] in a solid using a CO_2 laser, but since the development and maturity of high power, shortly pulsed Titanium Sapphire (Ti:Sa) lasers and doped fiber lasers, this field of research and its applications got accelerated significantly. Even though HHG can be generated in solids, liquids and gasses, we focus in this thesis on gas-based systems.

A semi-classical model can be used to get a basic physical understanding of the HHG process. This process is typically divided in three steps namely, **ionization**, **acceleration** and **recombination**, also known as the "three step model" [19] (TSM) and forms the foundation of the high harmonic generation process. These steps, as well as some intermediate steps, are shown in Fig. 3.5.

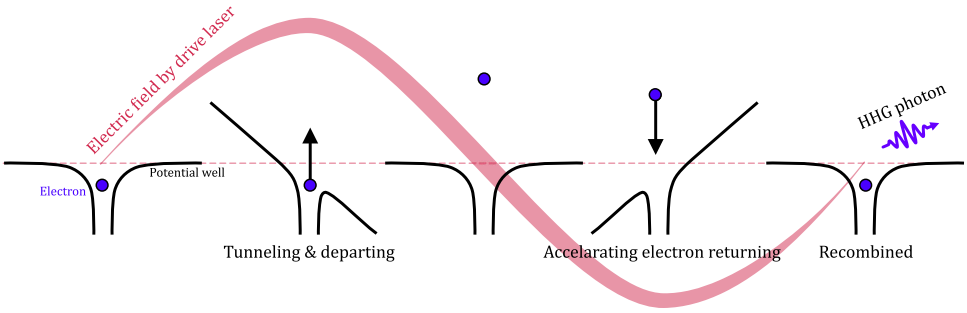

Figure 3.5: A strong electric field caused by a drive laser distorts the potential well enough where it allows for tunnel-ionization turning the bound electron into a free electron. The electric field accelerates the electron until the field changes sign, where the electron decelerates and eventually accelerates back to the atom. It may recombine with the atom, where it can release the built up kinetic energy through a high energy photon.

When an atom is exposed to a strong electric field, in this case originating from a drive laser, the potential well restraining an electron is distorted, allowing a bound electron to tunnel becoming a free electron. This free electron, still subjected to the electric field, gets accelerated and builds up kinetic energy. As mentioned before, as this electric field originates from a drive laser, we actually have an oscillating electric field. Thus once the electric field reverses sign, the electron is driven back towards the parent ion while building up kinetic energy. Once the electron approaches the parent ion, there is a chance it will collide and recombine with the parent ion where it may release the additional built up kinetic energy in the form of a photon.

The maximum photon energy U_{cutoff}, i.e. shortest wavelength, which can be generated through this method depends on the amplitude E_0 and the wavelength λ_0 of the drive

laser and the ionization potential of the parent atom:

$$U_{\text{cutoff}} = U_{\text{ip}} + 3.17U_{\text{p}} \quad \text{with} \quad U_{\text{p}} = \frac{e^2 E_0^2}{4 m_e \omega_0^2} \tag{3.3}$$

where U_{ip} is the ionization potential of the target atom [23]. U_{p}, also known as the ponderomotive energy, with E_0, ω_0, e, m_e being the strength and frequency of the driving field and the charge and mass of the electron, respectively. This relation indicates that the maximum energy of the generated photons increases for longer wavelengths of the drive laser. Initially, this feels a bit counter-intuitive from an energy conservation point of view (low energy in, high energy out), but as an electron resides for a longer time in the electric field of the drive laser it has more time to built up kinetic energy. Note that the efficiency of the HHG process of an individual atom drops off [24, 25] when scaling the wavelength of the drive laser too much as the probability of recombination reduces.

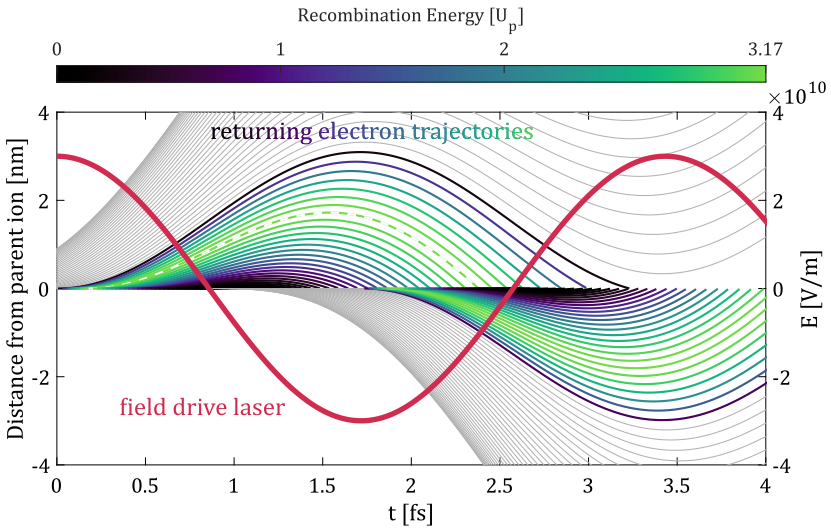

Figure 3.6: The electric field, shown in red, originates from the drive laser and displaces an electron from its parent ion. Depending on the phase at which the electron is ejected, it will either leave the parent ion and never return (grey trajectories), or return back to the parent ion (colored trajectories). The color of the trajectory depicts the buildup of kinetic energy in the electron once it recombines with the parent ion, with a maximum value of $3.17U_{\text{p}}$, highlighted by the dashed line. Everything below this line is considered a short trajectory, and everything above it is considered a long trajectory. The trajectories are simulated by using simple motion equations and the electric force on a charged particle. Image reproduced from [26].

Using the three step model as a basis, we can simulate the expected trajectories of free electrons in the oscillating electric field as depicted in Fig. 3.6 "born" at different times within a period of the drive laser. Electrons which are "born" when the amplitude of the electric field is increasing, will be ejected and never return to the parent ion and thus will not contribute to higher harmonics, as shown in Fig. 3.6 with the grey lines. In the other two quarters there is a possibility for the electron to return and recombine

with the parent ion. The maximum additional energy which can be build equals $3.17U_p$, indicated by the dashed trajectory in Fig. 3.6.

Two different possible paths can be distinguished for a given recombination energy, and these paths are referred to as "short" and "long" trajectories. In a long trajectory, the electron is ionized early in the process and is driven further away from its parent ion and spends more time in the laser field before it is driven back to recombine. In a short trajectory, the electron is released later but quickly driven back to the parent ion by the laser field after ionization. Only for the trajectories which have the maximum energy, where we have an additional kinetic energy of $3.17U_p$, are these paths identical (dashed trajectory in Fig. 3.6).

Long trajectories are less likely to result in recombination, as the electron can be deflected away from the parent ion by the laser field or collide with other particles. Thus, the harmonic signal from long trajectories is often weaker than that from short trajectories.

Looking at Fig. 3.6, we see that an electron can recombine with its parent ion two times during one complete cycle of the laser light. This creates a pulse train of extremely short bursts that repeat every half cycle of the laser, leading to the generation of high harmonic frequencies. Because these bursts happen twice in one complete cycle of the laser, the harmonic peaks are separated by twice the fundamental frequency of the driving laser and due to symmetry we only observe odd harmonics. Hence, we would expect an emitted spectrum $g(\omega)$ to look like

$$g(\omega) = 2\omega_0 \sum_{n=0}^{N_{\text{cutoff}}} f((2n+1)\omega_0) f_{\text{har}}(\omega - (2n+1)\omega_0), \tag{3.4}$$

with $f((2n+1)\omega_0)$ being the amplitude of each harmonic and $f_{\text{har}}(\omega - (2n+1)\omega_0)$ represents the shape of each harmonic in the frequency domain. This is visualized in a simplistic manner in Fig. 3.7.

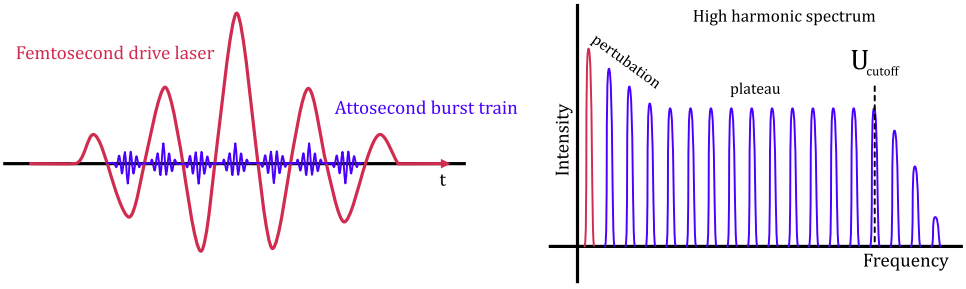

Figure 3.7: Left: A burst of light is emitted every half cycle of the drive laser, leading to a burst train. This behaviour results in the frequency domain to odd harmonics up to the cut-off energy as described in Eq. 3.3.

3.3.1. PHASE MATCHING

Phase matching is a crucial concept in nonlinear optics, including high harmonic generation (HHG), to maximize the efficiency of the process. It relates to the alignment of phases of waves at each generated frequency during a nonlinear interaction. In a nonlinear process like HHG, the incoming laser light (the fundamental wave) interacts with a medium (for example a gas jet) to generate a new wave at a different frequency (the higher harmonics). The fundamental wave and the higher harmonics then propagate together through the medium. However, due to dispersion, the phase velocities (the speed at which a point of constant phase travels) of these two waves in the medium are in general different.

If the fundamental wave and the harmonic wave are out of phase, they can destructively interfere, resulting in a low harmonic signal. On the other hand, if they are in phase (phase-matched), they can constructively interfere, resulting in a strong harmonic signal. Thus, for efficient generation of high harmonics, it is important to ensure phase matching.

Achieving phase matching can be challenging for several reasons. One of the main factors is the dispersion of the medium, in this case a soup of free electrons, neutral atoms and ionized atoms given by Δk_{na}, Δk_{fe} and Δk_{ia}, respectively. This can lead to a mismatch in phase velocities of the fundamental and harmonic waves, loosely defined as:

$$\Delta k = \Delta k_{\mathrm{fe}} + \Delta k_{\mathrm{na}} + \Delta k_{\mathrm{ia}} + \Delta k_{\mathrm{other}} \tag{3.5}$$

Other contributions to the phase mismatch $\Delta k_{\mathrm{other}}$ can range from an induced wavefront curvature by tightly focusing, different propagation geometries such as waveguides, gas jets or hollow-core fibers, or dipole phase which arises from the atomic or molecular response to the laser field.

For example, in the case of a free focusing geometry we mainly consider the wavefront curvature mismatch by focusing Δk_{Guoy}, dispersion from the ionized medium $\Delta k_{\mathrm{fe+na}}$, and due to the intensity dependent dipole phase $\Delta k_{\mathrm{dipole}}$;

$$\Delta k = \underbrace{m\frac{\partial}{\partial z}\left(-\arctan\frac{z}{z_0}\right)}_{\text{Guoy phase}} \underbrace{-\frac{2\pi m}{\lambda}\frac{p}{p_0}\Delta\delta\left(1-\frac{\eta}{\eta_c}\right)}_{\text{dispersion}} - \underbrace{\alpha_m\frac{\partial I}{\partial z}}_{\text{dipole phase}}, \tag{3.6}$$

with m being the harmonic order of interest, $\Delta\delta$ the difference in refractive index of the drive laser and the harmonics, p the pressure of the medium relative to the ambient pressure p_0, η refers to the ionization fraction and η_c is the critical ionization fraction [27].

Various techniques are used to achieve phase matching in HHG. These include tuning the properties of the medium, such as its density or pressure, medium geometries, focusing geometry or applying an external field, such as a static magnetic or electric field. The choice of technique depends on the specifics of the HHG setup and the desired properties of the high harmonic signal. The group of Kapteyn and Murnane in Boulder (USA)

focused mainly (not exclusively) on phase-matched high-order harmonic generation in hollow waveguides [28–30]. Meanwhile gas jet based systems were the main focus (not exclusively) by the group of Limpert in Jena (Germany) [31, 32]. The research activities at both groups has lead to a commercialization of their respective HHG systems via spin-offs KMLabs and Active Fiber Systems.

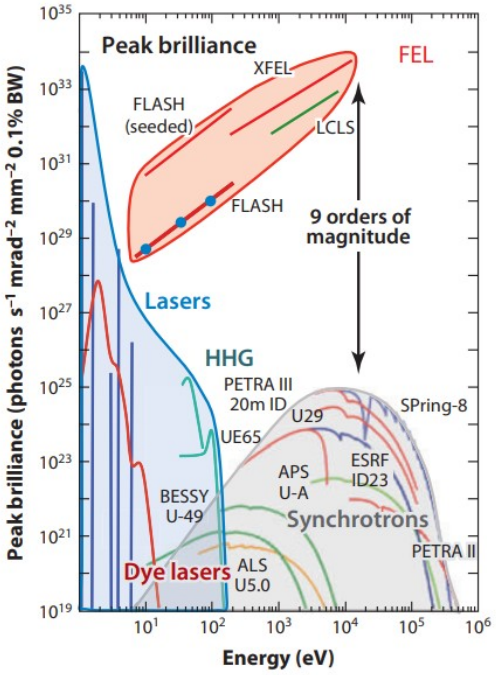

Figure 3.8: A comparison between synchrotrons, free electron lasers, high harmonic generation sources and common optical lasers in terms of peak brilliance. Figure source: [33].

The efficiency of this high harmonic generation process is typically rather low, typically in the order of $10^{-8} - 10^{-5}$ [34, 35]. HHG efficiency is influenced by several parameters, including the intensity and wavelength of the driving laser, the target gas or material, and the phase matching conditions. Generally, higher driving laser intensities and shorter wavelengths tend to increase the harmonic yield, but they also require precise control to avoid ionization of the medium, which can diminish the efficiency. Phase matching, where the generated harmonics constructively interfere over the interaction length, is crucial for maximizing HHG efficiency. Despite these complexities, advancements in high power laser technology and phase matching techniques have significantly improved HHG output and efficiency [36]. If we would just look at peak brilliance, HHG sources cannot compete with light sources at large scale facilities (especially free electron lasers), see Fig. 3.8. The main advantage of high harmonic generation sources lies in their compactness and relative affordability.

3.4. UPCOMING INVERSE COMPTON SCATTERING SOURCES

Although this thesis is related to HHG as a compact and coherent EUV source, a different approach based on Inverse Compton Scattering (ICS) is starting to ramp up as well [37–40]. The idea of ICS sources emerged in the late 20th century, based on the theoretical principle of Compton scattering formulated by Arthur H. Compton in 1923. This is a process where a photon scatters off a charged particle, typically an electron, and in the process transfers some of its energy to the particle. In an Inverse Compton Scattering source, the process is effectively reversed: a high-energy electron transfers part of its energy to a lower-energy photon, typically from a laser, boosting it into the X-ray or gamma-ray part of the spectrum. This allows for the production of high-energy photons without the need for the large, high-energy accelerators used in synchrotron or XFEL facilities.

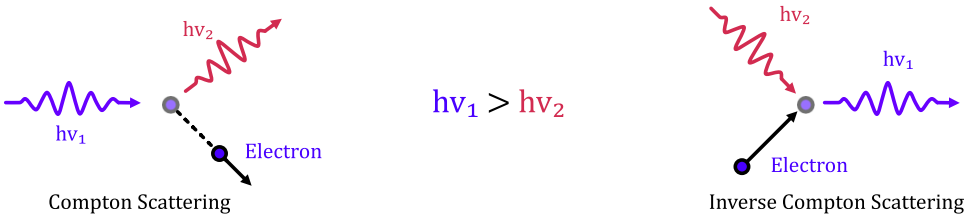

Figure 3.9: When a high-energetic photon collides with an electron it can scatter through Compton Scattering, transferring a part of the energy to the electron, resulting in a lower energetic photon. For Inverse Compton Scattering an energetic electron and a relatively low energetic photon collide resulting in a higher energetic photon, potentially in the X-Ray part of the spectrum.

While the current state-of-the-art Inverse Compton Scattering (ICS) sources have made considerable advancements [41], they do have some limitations. One of the key challenges is that, under standard operation, these sources emit incoherent radiation. This characteristic restricts their application in lensless imaging, where coherent light or at least partially coherent light is essential. However, using a laser-cooled ultra cold electron source (UCES) [42] or microbunched electron packets [43, 44] could potentially yield coherent soft x-rays and potentially reach higher brightness levels compared to HHG and is something to keep an eye on.

BIBLIOGRAPHY

1. Attwood, D. & Sakdinawat, A. *X-Rays and Extreme Ultraviolet Radiation: Principles and Applications* 2nd ed. (Cambridge University Press, 2017).
2. Grynberg, G., Aspect, A. & Fabre, C. *Introduction to quantum optics: from the semi-classical approach to quantized light* (Cambridge university press, 2010).
3. Svelto, O. *Principles of Lasers* ISBN: 9781441913029. https://books.google.nl/books?id=ioywRI5W2HEC (Springer US, 2010).
4. Carter, A. B. *Directed Energy Missile Defense in Space: Background Paper* in (1984).
5. Nilsen, J. *Legacy of the X-ray Laser Program* tech. rep. (Lawrence Livermore National Lab.(LLNL), Livermore, CA (United States), 1993).
6. Matthews, D. L. *et al.* Demonstration of a Soft X-Ray Amplifier. *Phys. Rev. Lett.* **54,** 110–113. https://link.aps.org/doi/10.1103/PhysRevLett.54.110 (2 Jan. 1985).
7. Rosen, M. *et al.* Exploding-foil technique for achieving a soft x-ray laser. *Physical review letters* **54,** 106 (1985).
8. Suckewer, S., Skinner, C. H., Milchberg, H., Keane, C. & Voorhees, D. Amplification of stimulated soft x-ray emission in a confined plasma column. *Phys. Rev. Lett.* **55,** 1753–1756. https://link.aps.org/doi/10.1103/PhysRevLett.55.1753 (17 Oct. 1985).
9. Rosen, M. D. *et al.* Exploding-Foil Technique for Achieving a Soft X-Ray Laser. *Phys. Rev. Lett.* **54,** 106–109. https://link.aps.org/doi/10.1103/PhysRevLett.54.106 (2 Jan. 1985).
10. Veksler, V. I. A new method of acceleration of relativistic particles. *J. Phys.* **9,** 153–158. https://cds.cern.ch/record/109364 (1945).
11. Wilson, E. J. *Fifty years of synchrotrons* in *Proceedings of the 1996 European Particle Accelerator Conference (EPAC'96)* (1996), 135–139.
12. *Operation of the XFEL Accelerator DESY* https://xfel.desy.de/. Accessed: 2023-09-08.
13. Rajendran, R. *et al. Towards a stand-alone high-throughput EUV actinic photomask inspection tool: RESCAN* in *Metrology, Inspection, and Process Control for Microlithography XXXI* **10145** (2017), 199–210.
14. *ESRF Accelerators data* https://www.esrf.fr/home/UsersAndScience/Accelerators/parameters.html. Accessed: 2023-09-08.
15. *SLAC at a glance* https://www6.slac.stanford.edu/about/lab-overview/at-a-glance. Accessed: 2023-09-08.

16. *European XFEL Facts and Figures* https://www.xfel.eu/facility/overview/facts_amp_figures/index_eng.html. Accessed: 2023-09-08.

17. *Two years of user operation in numbers - 1200 users, 60 experiments and 6 petabytes* https://www.xfel.eu/news_and_events/news/index_eng.html?openDirectAnchor=1713. Accessed: 2023-09-08.

18. L'Huillier, A., Schafer, K. J. & Kulander, K. C. Theoretical aspects of intense field harmonic generation. *Journal of Physics B: Atomic, Molecular and Optical Physics* **24,** 3315 (1991).

19. Corkum, P. B. Plasma perspective on strong field multiphoton ionization. *Physical review letters* **71,** 1994 (1993).

20. McPherson, A. *et al.* Studies of multiphoton production of vacuum-ultraviolet radiation in the rare gases. *J. Opt. Soc. Am. B* **4,** 595–601. https://opg.optica.org/josab/abstract.cfm?URI=josab-4-4-595 (Apr. 1987).

21. Ferray, M. *et al.* Multiple-harmonic conversion of 1064 nm radiation in rare gases. *Journal of Physics B: Atomic, Molecular and Optical Physics* **21,** L31 (1988).

22. Burnett, N., Baldis, H., Richardson, M. & Enright, G. Harmonic generation in CO2 laser target interaction. *Applied Physics Letters* **31,** 172–174 (1977).

23. Jl, K. *et al. High-order harmonic-generation from atoms and ions in the high-intensity regime. Phys. Rev. Lett. 68, 3535-3538* Apr. 2018. https://doi.org/10.1103/physrevlett.68.3535.

24. Frolov, M., Manakov, N. & Starace, A. F. Wavelength scaling of high-harmonic yield: threshold phenomena and bound state symmetry dependence. *Physical review letters* **100,** 173001 (2008).

25. Frolov, M. *et al.* Scaling laws for high-order-harmonic generation with midinfrared laser pulses. *Physical Review A* **92,** 023409 (2015).

26. Hofmann, C., Landsman, A. S. & Keller, U. Disentangling long trajectory contributions in two-colour High Harmonic Generation. *Applied Sciences* **8,** 341 (2018).

27. Tong, X.-M. Multiscale simulation of high-order harmonic generation: From microscopic to macroscopic. *Physical Review A* **108,** 023118 (2023).

28. Rundquist, A. *et al.* Phase-matched generation of coherent soft X-rays. *Science* **280,** 1412–1415 (1998).

29. Durfee, C. G., Backus, S., Kapteyn, H. C. & Murnane, M. M. Intense 8-fs pulse generation in the deep ultraviolet. *Optics Letters* **24,** 697–699 (1999).

30. Durfee, C. G., Backus, S., Murnane, M. M. & Kapteyn, H. C. Ultrabroadband phase-matched optical parametric generation in the ultraviolet by use of guided waves. *Optics Letters* **22,** 1565–1567 (1997).

31. Rothhardt, J. *et al.* Absorption-limited and phase-matched high harmonic generation in the tight focusing regime. *New Journal of Physics* **16,** 033022 (2014).

32. Hädrich, S. *et al.* High photon flux table-top coherent extreme-ultraviolet source. *Nature Photonics* **8,** 779–783 (2014).

33. Ullrich, J., Rudenko, A. & Moshammer, R. Free-electron lasers: New avenues in molecular physics and photochemistry. *Annual review of physical chemistry* **63,** 635–660 (2012).

34. Falcao-Filho, E. L., Gkortsas, V., Gordon, A. & Kärtner, F. X. Analytic scaling analysis of high harmonic generation conversion efficiency. *Optics express* **17,** 11217–11229 (2009).

35. Wang, H. *et al.* Bright high-repetition-rate source of narrowband extreme-ultraviolet harmonics beyond 22 eV. *Nature communications* **6,** 7459 (2015).

36. Loetgering, L., Witte, S. & Rothhardt, J. Advances in laboratory-scale ptychography using high harmonic sources. *Optics Express* **30,** 4133–4164 (2022).

37. Hornberger, B., Kasahara, J., Gifford, M., Ruth, R. & Loewen, R. *A compact light source providing high-flux, quasi-monochromatic, tunable X-rays in the laboratory* in *Advances in Laboratory-based X-Ray Sources, Optics, and Applications VII* **11110** (2019), 1111003.

38. Stragier, X., Mutsaers, P. & Luiten, O. Smart* Light: A Tabletop, High Brilliance, Monochromatic and Tunable Hard X-ray Source for Imaging and Analysis. *Microscopy and Microanalysis* **24,** 310–311 (2018).

39. Graves, W. S. *et al.* Compact x-ray source based on burst-mode inverse Compton scattering at 100 kHz. *Phys. Rev. ST Accel. Beams* **17,** 120701. https://link.aps.org/doi/10.1103/PhysRevSTAB.17.120701 (12 Dec. 2014).

40. Variola, A. *The THOMX project* in *2nd International Particle Accelerator Conference (IPAC'11)* (2011), 1903–1905.

41. Mușat, V., Latina, A. & D'Auria, G. *A high-energy and high-intensity inverse Compton scattering source based on CompactLight technology* in *Photonics* **9** (2022), 308.

42. Franssen, J. G. H. *et al.* From ultracold electrons to coherent soft X-rays. *arXiv: Accelerator Physics*. https://api.semanticscholar.org/CorpusID:150373895 (2019).

43. Nanni, E. A., Graves, W. S. & Moncton, D. E. *From incoherent to coherent x-rays with ICS sources* in *SPIE Optical Engineering + Applications* (2015).

44. Schaap, B. H., de Vos, T., Smorenburg, P. & Luiten, O. J. Photon yield of superradiant inverse Compton scattering from microbunched electrons. *New Journal of Physics* **24,** 033040 (2022).

4

SHORT-WAVELENGTH LENSLESS IMAGING BEAMLINE DESIGN

This chapter presents a detailed description of the design, assembly and performance of an EUV beamline with a high harmonic generation source designed for lensless imaging. The beamline consists of four subsystems: the drive laser, the high harmonic generation system, the beam analysis system, and the lensless microscope unit. A comprehensive overview of each subsystem, including its individual components and functions, is given. There are challenges associated with maintaining alignment in the non-linear compression unit, high harmonic generation unit, and microscope vacuum vessel. A detailed explanation of the experimental setup, including details such as the design of the vacuum system and optics, gives insights into the design choices to ensure the system operates within the specified requirements for lensless imaging.

4.1. INTRODUCTION

This thesis predominantly focuses on the experimental work performed on an extreme UV (EUV) and Soft X-Ray (SXR) lensless microscopy beamline that has been designed, developed and built from scratch at the Optics Research Group of the TU Delft, warranting an entire chapter. The system is subdivided into four subsystems which are constructed on a 4.2 by 1.5 meter optical table. These subsystems include the infrared (IR) drive laser, the high harmonic generation system, the beam analysis system, and the lensless microscope unit. Each sub-assembly will be discussed individually in this chapter.

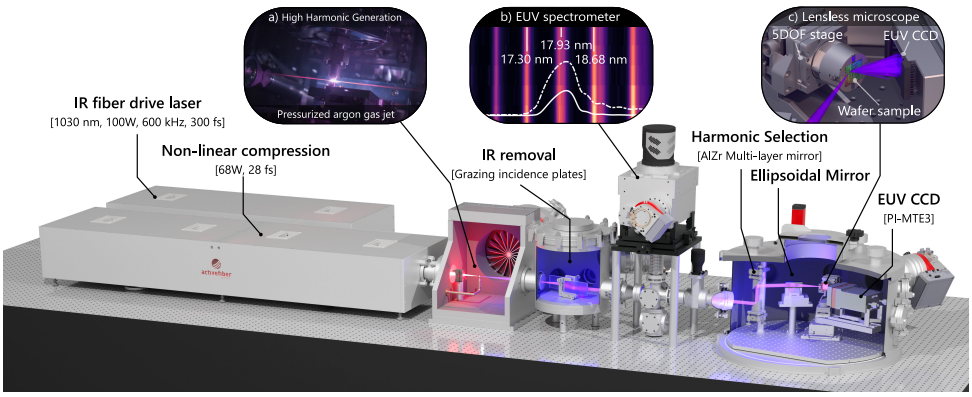

Figure 4.1: A 3D render of the entire EUV beamline, consisting of four sub-assemblies namely the IR drive laser, the high harmonic generation system, the beam analysis system and the lensless microscope vessel which are connected sequentially. Each subassembly will be covered in a dedicated subsection.

4.2. HIGH-INTENSITY FEMTOSECOND DRIVE LASER

The drive laser is crucial to generate (partially) coherent EUV/SXR light through high harmonic generation as explained in Chapter 3. Many beamlines in this field are driven by Titanium Sapphire (Ti:Sa) lasers [1–11] with a center wavelength at 800 nm at relatively high pulse energies on the order of a few milli-joules per pulse and a low repetition rate of about 1 kHz. In contrast to those systems, the EUV beamline described in this thesis is driven by a compact, high-power, commercially accessible, Ytterbium-doped fiber laser system (Active Fiber Systems Ytterbium-100 [12]), with a center wavelength at 1030 nm, characterized by relatively lower pulse energy on the order of several hundred microjoules but with the possibility to operate at much higher repetition rates on the order of a few MHz. Similar drive lasers have been used in recently reported high harmonic generation sources [13–16].

The repetition rate f_{rep} of the Ytterbium-doped fiber laser can be set up to the oscillator frequency f_{osc} of 19 MHz or set to integer divisions of f_{osc}. For example, an integer division of 31 leads to a repetition rate of about 600 kHz. From the oscillator, the pulses go through a pre-amplifier, pulse stretcher, pulse picking and phase shaping module, after which they are amplified by a main amplifier and compressed through chirped pulse

amplification (CPA). This commercial subsystem is treated as a black box.

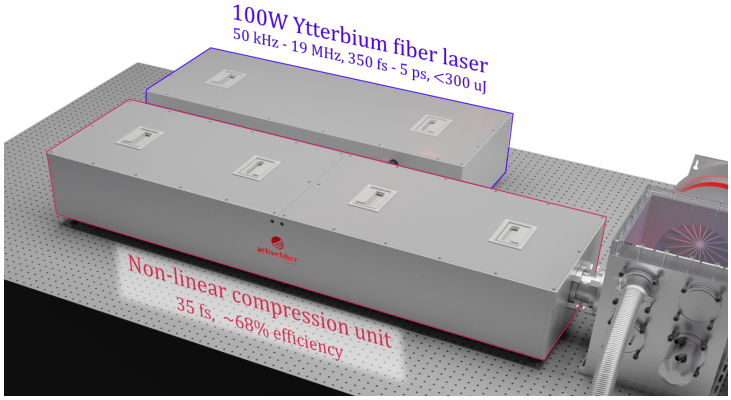

Figure 4.2: A 3D render of the drive laser system based on Ytterbium fiber laser technology. This 100 W drive laser emits pulses ranging from 350 fs to 5 ps at repetition frequencies from 50 kHz to 19 MHz, and it can deliver a top pulse energy of 300 µJ. Subsequently, a pulse compression mechanism employing non-linear compression via a hollow core fiber is coupled to the 100 W system to further shorten the pulses down to 35 fs.

The pulse length of the pulses from the CPA module can be dispersively tuned from 350 fs to 5 ps, with pulse energies reaching up to 300 µJ. This results in a maximum average power of 100 W and peak powers ranging between 1 and 5 GW. The average output power of the laser can be adjusted by varying the amplifier currents, which range from 0 to 36.5 A.

For efficient HHG generation in the EUV regime, short pulses in the order of a few femtoseconds are desired to improve phase matching conditions and reduce self-absorption in the generated plasma. The "native" pulse length of 300 fs from the primary drive laser, outlined in purple in Fig. 4.2, can be further compressed in the sequential unit outlined in red in the same figure. In this unit the pulses are first spectrally broadened, due to nonlinear effects as self phase modulation, in a hollow core fiber (HCF) which is located in a pressurized vessel filled with 7 bar of Krypton. This fiber, with a 200 µm diameter hollow core and a length of approximately 1.2 meters, results in significant power loss, with an average efficiency of about 68%. To ensure thermal stability, the entire HCF unit is water-cooled, as the fiber absorbs about 32 Watts of laser light when operated at full power. After passing through the hollow core fiber, the output beam is collimated using a plano-convex lens, resulting in a beam diameter of 4.2 mm. A set of dispersive chirped mirrors downstream compresses the pulse to approximately 30 femtoseconds. The pulse length has been measured once through an autocorrelation method assuming a sech^2 pulse shape (defined as $\cosh(t/\tau)^{-2}$ with τ being the pulse width), associated with a measured spectrum as shown in Fig. 4.4 to be used as a reference to ensure successful pulse compression.

The wavefront of the drive laser can be measured in the leak light through a mirror and is

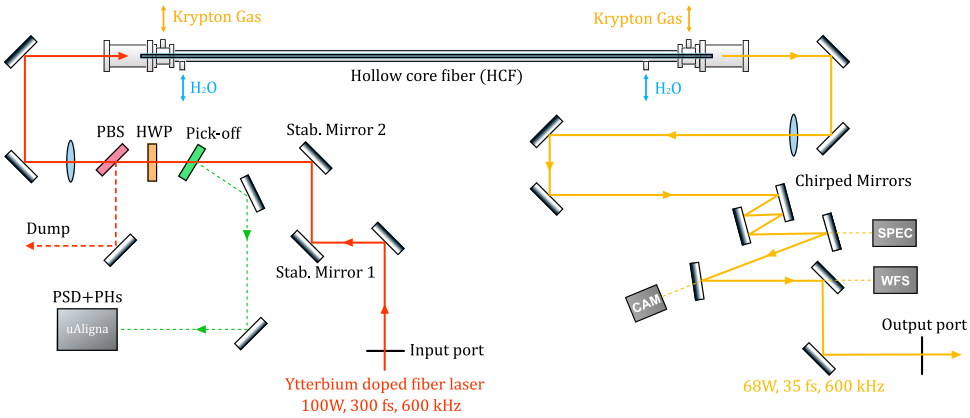

Figure 4.3: A schematic depiction of the non-linear compression unit. We start at the input (center bottom in the figure) originating from the main drive laser. After two actively controlled stabilized mirrors (TEM µAlgina), using the pick-off beam as a reference, the beam can be either directed into the dump port or into the hollow core fiber (HCF) by using a half wave plate and polarisation beam splitter combination. The beam is focused into the HCF situated in a pressurized Krypton gas broadening the pulses non-linearly, after which the pulses are linearly compressed down to 35 fs using a set of chirped mirrors. The leak light through the last few mirrors can be used to inspect the spectrum, beam profile and wavefront after which the beam is directed to the output port.

assessed using a Shack-Hartmann wavefront sensor[1]. This assessment reveals the presence of defocus and vertical astigmatism, see Fig. 4.4, with the latter having the potential to be amplified in the HHG beam. The beam quality factor, M^2, is commonly observed to be less than 1.2, close to diffraction limited.

The in-coupling process into the HCF can be intricate and requires a stable beam to avoid damaging the fiber. Therefore, the CPA beam is first stabilized using a set of piezo-driven mirrors controlled by a TEM µAligna beam stabilization unit before coupling into the fiber. A pick-off mirror extracts a small portion of the main beam (shown as a green line in Fig. 4.3) for a closed-loop stabilization system. This beam stabilization is only activated above a threshold power of 17 W. A combination of a waveplate in a motor-driven rotation mount and a polarisation beamsplitter allows for control how much power is going to a dump port (beam path labelled with a red dashed line in Fig. 4.3) or to the HCF.

4.3. HIGH HARMONIC GENERATION EUV LIGHT SOURCE

The IR beam is guided into the first set of vacuum chambers in the EUV beamline. The first chamber, as shown in Fig. 4.5 outlined in purple/blue, is where the higher harmonics are generated. The bottom plate of the vacuum chamber acts as an integrated optical breadboard and is water cooled to ensure the thermal stability. The top cover of the vacuum chamber is made of a 5 centimeter thick transparent plastic slab and allows for visual inspection of the generated plasma inside the HHG source during operation.

[1] Some additional wavefront aberrations can be introduced by the propagation through the mirror.

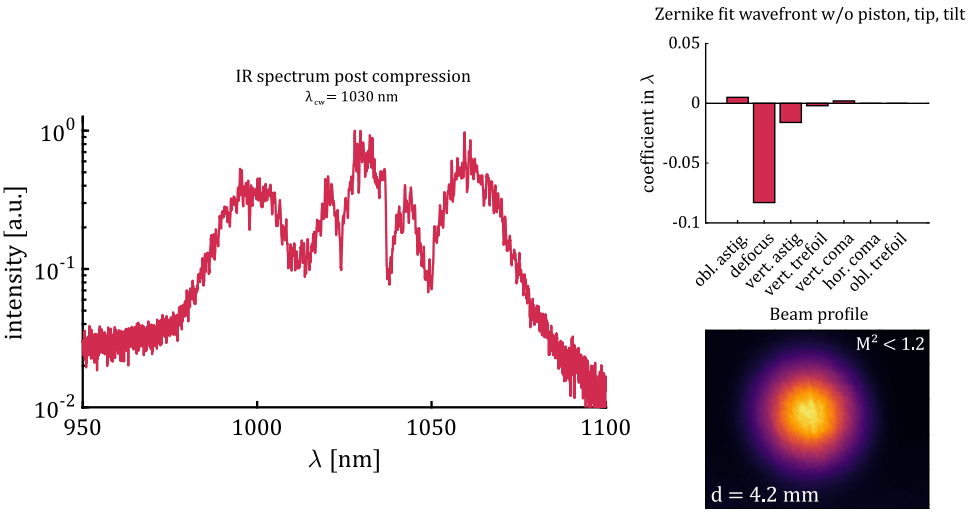

Figure 4.4: Left: Typical measured spectrum after compression via picked-off leak light through a mirror as shown in Fig. 4.3 and labelled with 'SPEC'. Top-right: A wavefront of the leak light through a mirror is measured with a Shack-Hartmann based wavefront sensor, which is mainly dominated by defocus, caused by the lens right after the hollow core fiber (HCF). The beam quality is heavily dependent on the in-coupling into the HCF. Bottom-right: A fairly Gaussian beam can be observed after the pulse compression, which is used to generate the higher harmonics.

The IR beam passes into the vessel through a IR transmission window where the beam is focused with a plano-convex lens with a focal length of 80 mm resulting in a spot-size of about 30 µm in diameter. With an average power of 68 W, 30 fs pulse length at 600 kHz in a 30 µm spot, a peak power density in the order of 10^{15} W/cm^2 can be achieved.

Near the focus a set of brass gas jet nozzles with diameter of 220 and 300 µm are placed. The nozzles are mounted on X, Y and Z linear piezo-driven SmarAct stages in order to align the nozzles with the IR beam. The Y-axis allows to switch between the two nozzles. The nozzle is fed via a pressure regulated gas line attached to a switch where different gas types can be selected, either argon or neon. The gas bottles are attached to an automatic switching station, when the pressure of the gas bottle drops allowing for long experiments without running out of drive gas.

Opposite to the gas jet nozzle, a gas catcher is placed (see Fig. 4.6), which is directly attached to an Edwards XDS35 scroll pump to maintain a vacuum when the gas is injected into the chamber. This setup is complemented by a magnetically levitated turbo-molecular pump (Pfeiffer ATH1600M) with a pumping speed of 1200 liters per second for argon, also combined with another XDS35 scroll pump. A base pressure of 10^{-7} mbar can be achieved when no gas is injected into the chamber, and 10^{-3} up to 10^{-2} mbar when the gas is injected. This vacuum pressure is sufficient for Extreme Ultraviolet (EUV) to propagate through without any noticeable losses, as can be estimated using the H_2O vapor transmission values from the CXRO database [17]. However, operating continuously on this vacuum pressure can put a strain on the turbo-molecular pumps.

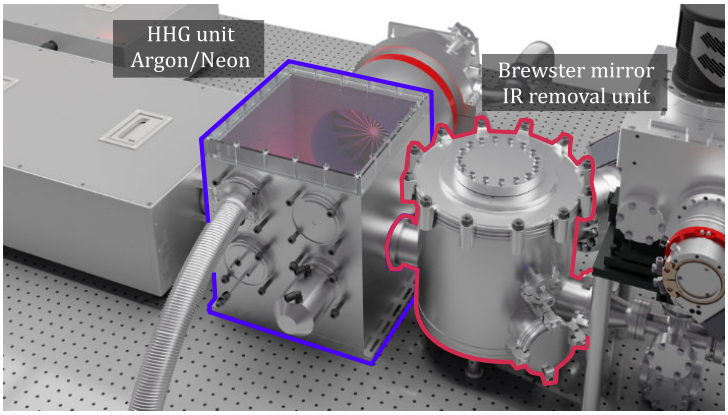

Figure 4.5: A 3D render of the High Harmonic Generation unit (highlighted in purple) and IR removal unit (highlighted in red). The top cover of the HHG chamber allows to visually inspect the plasma as shown in Fig. 4.6. Both vacuum chambers have a dedicated turbo molecular pump (Pfeiffer ATH1603M and Pfeiffer HiPace 300) backed by a scroll pump (Edwards XDS35). The chambers are connected through a 5 mm aperture to enable differential pumping, reducing the pumping load downstream.

Differential pumping is applied to reduce the downstream flow of residual drive gas to the remaining vacuum chambers. The HHG vessel is connected to the next chamber via a 5 mm by 50 mm tube, resulting in a base pressure in all other vacuum chambers of 10^{-7}-10^{-6} mbar. With this setup, photon fluxes of 10^9 and 10^{11} photons per second are achieved at photon energies of 92 eV (λ = 13.4 nm, 77th harmonic) and 68 eV (λ = 18 nm, 57th harmonic), respectively, as detailed in [18, 19] before filtering. These results were obtained with the IR drive laser operating at an average power of 68 W, with pulse durations of 30 fs at a repetition rate of 600 kHz. For generating these higher harmonics around 18 nanometers, argon with a backing pressure of 10 bar was used. For harmonics around 13.5 nanometer a neon gas jet with a backing pressure of 7 bar is used.

The resulting photon fluxes, ranging from a few hundred nanowatts to a few microwatts, are eight orders of magnitude lower than the average power of the drive laser. In order to actually make use of the generated EUV light, it is necessary to remove the high power IR drive laser from the relatively low power generated higher harmonics. The first step happens right after the plasma, where we take advantage of the discrepancy in beam divergence between the drive laser and the generated EUV beam of 55 mrad and 3.2 mrad respectively. An annular-shaped IR mirror with a center hole of 1.5 mm in diameter is placed at 45 degrees with respect to the optical axis. The difference in divergence ensures that the EUV beam passes lossless through the center aperture while the outer ring of the IR beam is rejected, dumping 64% of the light from the drive laser in a dump port.

A set of mirrors, coated with a 127 nm layer of Nb_2O_5 and a second 235 nm layer of SiO_2 on a glass substrate, are placed at the Brewster angle for the infrared drive laser. Therefore, about 99% of the linearly polarized IR light is transmitted while the produced EUV light is still partially reflected. In total, 52% of the EUV light remains, along with a few tens of mW of infrared light. The residual infrared light is absorbed using a set of metal-

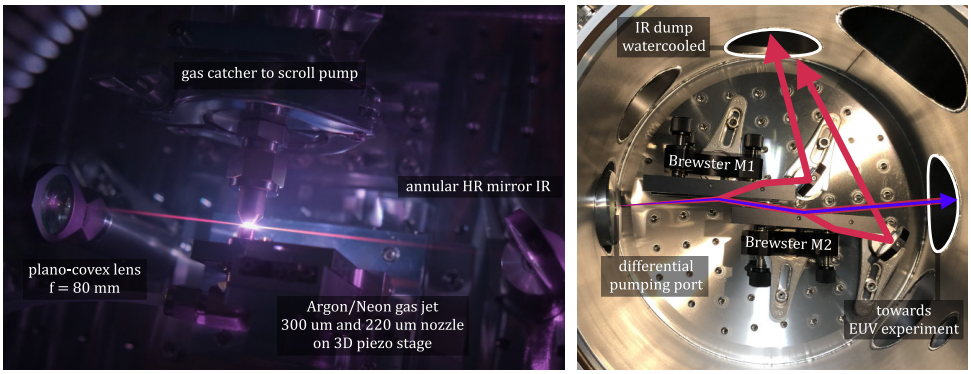

Figure 4.6: **Left:** The IR beam is focused between the gas jet nozzle and gas catcher where the plasma is generated. An annular mirror partially separates IR light from the EUV light without any losses in the EUV. After which it goes through a 5 mm tube of 5 cm to the next chamber. **Right:** The EUV and IR beam enters the next vacuum vessel from the left where two mirrors are placed set at the Brewster angle for IR. At this angle the IR is mostly transmitted while the EUV light is reflected. The IR light is dumped in a water cooled dump port while the EUV is passed towards the experimental port with a very small amount of residual IR light. This residual is removed by using two thin-film metallic filters of 200 nanometers thick. The metal of choice depends on the desired EUV wavelength, either aluminum or zirconium for 18 nanometer and 13.5 nanometer respectively.

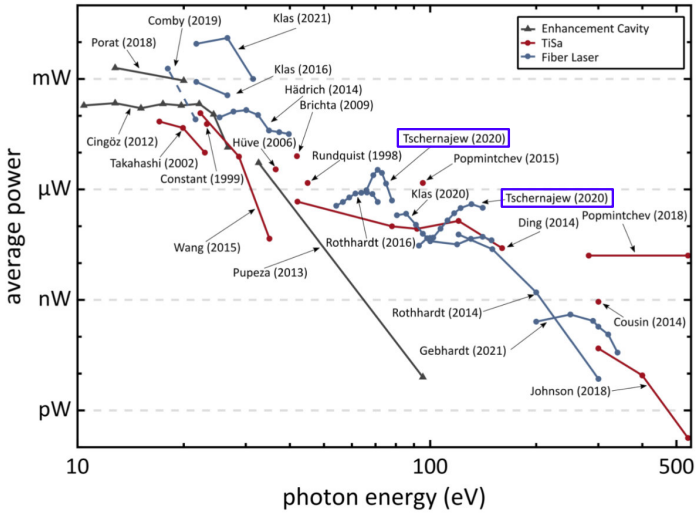

Figure 4.7: A performance overview of state-of-the-art HHG sources as reported in [18] with different drive lasers. HHG systems which are driven by fiber lasers tend to outperform Ti:Sa-based systems in terms of photon flux in the EUV regime. The HHG system as reported in this thesis and in [19], is highlighted by the two rectangles and labelled **Tschernajew (2020)**. These powers have been generated with an argon gas jet around 70 eV (approx. 18 nm) and neon gas jet for around 100 eV (approx. 13 nm). Figure reproduced from [18].

lic, free-standing foils. When the system is operated at 18 nanometer wavelength, a stack of two 200 nanometer thick aluminum foils is used, while for the 13.5 nanometer wavelength, a set of zirconium foils is utilized. These filter stacks have a total transmission of

54% and 24%, respectively [20]. With all of this combined, in the best case scenario, only a quarter of the light from the generated higher harmonics reaches the output port of the source ($1.7 \cdot 10^8$ and $2.8 \cdot 10^{10}$ photons for 13.4 nm and 18 nm respectively). In order to avoid accidental rupture of these delicate thin foils, a vacuum tube is placed as a by-pass to ensure pressure equilibrium before and after the foil stack.

Right after the output port of the source, a mirror with a bare gold coating is placed, oriented at 45 degrees to the optical axis. This setup is designed to precisely redirect the EUV beam into a compact, off-line transmission spectrometer. This particular spectrometer, developed by the University of Twente (Laser Physics & Nonlinear Optics group, LPNO) and Scientec [21], incorporates a 2D linear piezo-driven stage. Mounted atop this stage is a metal bracket, featuring a 5 mm aperture allowing to observe the EUV beam directly with all the harmonics (partially clipped by the aperture). On the same bracket a silicon wafer chip is mounted and serves as a holder for an array of 21 distinct transmission gratings. These gratings have been etched into a 200 nm silicon nitride (Si_3N_4) membrane, overlaid with a composite layer of 70 nm gold and 20 nm chromium to enhance contrast. The etched gratings vary in line densities, ranging from 500 to 10,000 lines per millimeter. A motorized translation stage allows for the positioning of a 200 µm slit in front of the gratings, resulting in a spectral resolution down to $\Delta\lambda = 0.13$ nm at a wavelength of 20 nanometer [21]. Frames of the spectrum or the beam are captured with a flange-mounted EUV camera (PI-PIXIS-2KB [22]), which is maintained at a temperature of −50°C and positioned 69.5 mm downstream from the grating assembly.

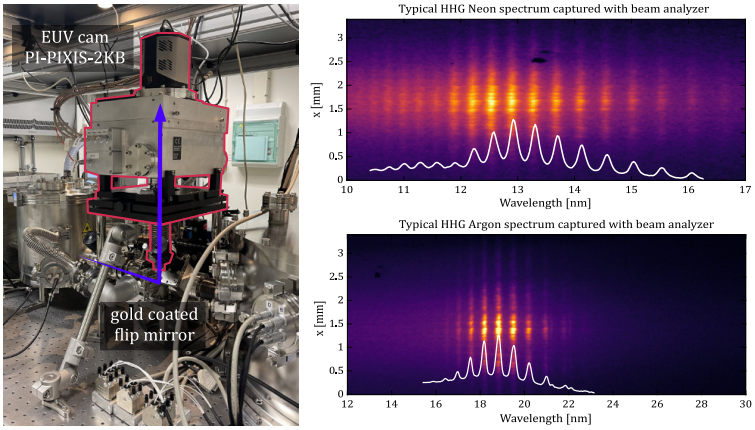

Figure 4.8: **Left:** An off-line beam analyzer [21] is mounted vertically on the beamline. A bare gold mirror can be inserted to flip the EUV beam into the beam analyzer. The beam analyzer has 21 different transmission gratings ranging from 500 lines per mm up to 10.000 lines per mm with a 200 µm slit on top. After 69.5 mm the spectrum can be observed with an EUV camera PI-PIXIS-2KB. **Top-right:** A spectrum captured around 13.5 nanometer using neon as drive gas. **Bottom-right:** argon is used to generate harmonic around 18 nanometer.

Beam pointing stability is a critical factor in the performance of any HHG light source, especially for applications such as lensless microscopy. The stability of the beam pointing is influenced by several factors for example, the fundamental pointing stability of the

drive laser, thermal settling of the system, vibrations within the system, and positioning stability of the gas jet. The generated EUV beam is directly aimed onto a full-vacuum EUV-sensitive camera, where a set of frames are acquired. A 2D Gaussian is fitted in each frame, defining its centroid position of which a beam pointing stability of ±30 µrad for a beam with a divergence of 3.2 mrad has been found, which is a significant dithering within 1% of the beam width.

The source performance figures given in this chapter are derived from a series of manual parameter sweeps where, eventually, trade-offs have been made and may not represent optimal conditions, as some source parameters are coupled. For instance, the gas jet location relative to the IR focus can greatly impact the virtual or physical source location of the harmonics, the beam divergence, photon flux and stability [23–25] due to changing phase matching conditions for different focusing conditions. Clipping the input NA of the IR drive laser slightly can improve focusing conditions, but this comes at a cost of input power. Ultimately, the HHG source must be tuned and optimized, to some degree, every day an experiment is initiated.

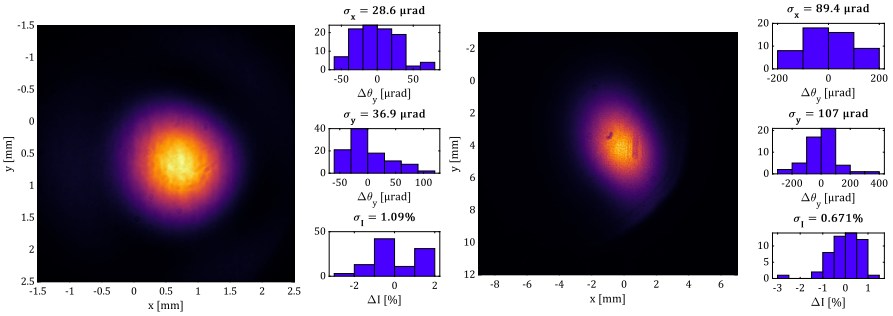

Figure 4.9: **Left:** A measured ideal case of the generated EUV beam at 18 nanometer, where the beam is close to Gaussian and uniform in all directions. The beam pointing stability in x and y direction is in the order of 30 µrad with an intensity stability of about 1%. **Right:** Unfortunately, it is not that trivial to keep the HHG source performing with the conditions as shown on the left due to thermal changes, pulse compression drift, mechanical drift of the gas jet and alignment inaccuracies. Usually an astigmatic distortion and a significantly higher angular beam pointing of 100 µrad is found.

4.4. DESIGN CONSIDERATIONS FOR EUV LENSLESS MICROSCOPE CHAMBER

In this subsection, we focus on design and engineering considerations for conducting lensless microscopy experiments on the EUV beamline. We will start from the vacuum chamber design, over to the EUV illumination optics and finally to the lensless microscope assembly. The conceptual design of the lensless microscope has been inspired by the work reported in [1, 4, 26].

4.4.1. VACUUM CHAMBER

Before getting into the experimental setup, we start with the vacuum chamber, which encloses the entire lensless imaging assembly. The vacuum vessel is the end-station of the beamline as shown in Fig. 4.1 and in Fig. 4.11. The vessel contains all the optics, electronics and mechatronics required for lensless imaging within a custom-made cylindrical chamber. The internal diameter of the chamber is 590 mm and 296 mm in height which is sandwiched in between a base plate and top plate. All the infrastructure, from data and power cabling to water cooling lines, must go through the welded ISO63-KF and CF100 flanges on the chamber. The system is pumped by a turbo molecular pump (Pfeiffer HiPace 300) and scroll pump (Pfeiffer HiScroll 6) combination, which should maintain a vacuum down to at least 10^{-6} mbar.

Conventional optical experiments are situated on a flat optical table, which is designed to be vibration-resistant/isolating and thermally stable, providing a stable platform for mounting optical components and other equipment needed for experimentation. A vacuum chamber however cycles through pump-down phases resulting in a pressure difference between inside and outside of the vacuum vessel. This causes the walls of the vacuum chamber, to some extent, to bend, inducing a misalignment of the components mounted in the chamber. In Fig. 4.10, a finite element model (FEM analysis in AutoDesk Inventor CAD) shows that the center of the base plate displaces by 0.29 mm in the positive z-direction due to the pressure difference. Maintaining any alignment after pumping-down remains a difficult, if not impossible, task without introducing many vacuum-compatible stages for re-alignment.

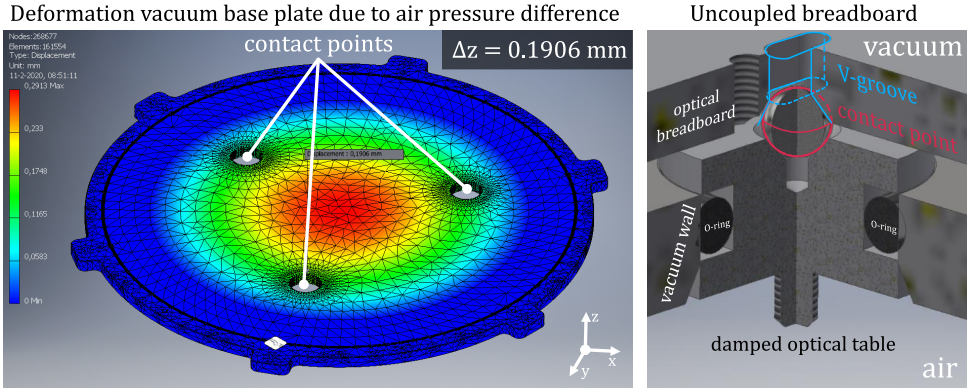

Figure 4.10: The base plate in the microscope vacuum vessel deforms due to the pressure difference between vacuum and ambient air pressure. If the optical breadboard would be mounted directly onto the base plate, it would be dynamically displaced by 0.19 mm in the z-direction causing a misalignment of the entire microscope. Right: Three support points are fed through the base plate, allowing them to be directly coupled to the stabilized, damped optical table and uncoupled from the vacuum vessel. V-grooves are milled in the optical breadboard to ensure kinematic mounting. A thick 8 mm O-ring around the supports is required for a leak tight seal.

An initial step to address this issue could be to reduce the surface area of the vacuum chamber or use thicker plates to a certain extent. However, this has already been maximised to some extent to keep the system manageable in terms of weight and size (∽50

kg, 590 mm x 0.2 mm) for the outsourced metalshop. The next step could be using a separate optical breadboard with v-grooves milled on the bottom. The latter can be mounted on top of three spherical contact points on the vacuum chamber's base plate to achieve kinematic mounting. This kinematic mounting ensures that the optical breadboard moves all together as an assembly in the z-direction with a reduced displacement of 0.19 mm.

The reduced 0.19 mm displacement remains a significant amount. An unconventional approach has been designed to completely isolate the optical breadboard from the vacuum chamber, as shown at the right of Fig. 4.10. Three holes of 30 mm are machined through the base plate. Three support posts surrounded with an 8 mm thick Viton O-ring is screwed into an interface plate which is directly mounted on the optical table. The base plate of the vacuum chamber is placed over these three supports through the aforementioned machined holes. As the supports are directly in contact with the damped optical table and semi-isolated (there is still some contact via the O-rings) from the vacuum walls, it completely eliminates any displacement during a pump down.

A possible risk of this approach is that the O-ring is not self-compressing during a pump down, potentially leading to reduced vacuum performance. On top of that, if contamination reaches the O-ring, resulting in a leak, the entire optical setup within the vacuum vessel must be taken out. However, it is expected that this issue could only occur if the base plate is moved around the O-ring, which would usually only happen during installation. Despite these potential risks, a baseline pressure of 10^{-7} mbar in an empty vacuum vessel has been achieved within 4 hours of pumping which is considered to be within specification.

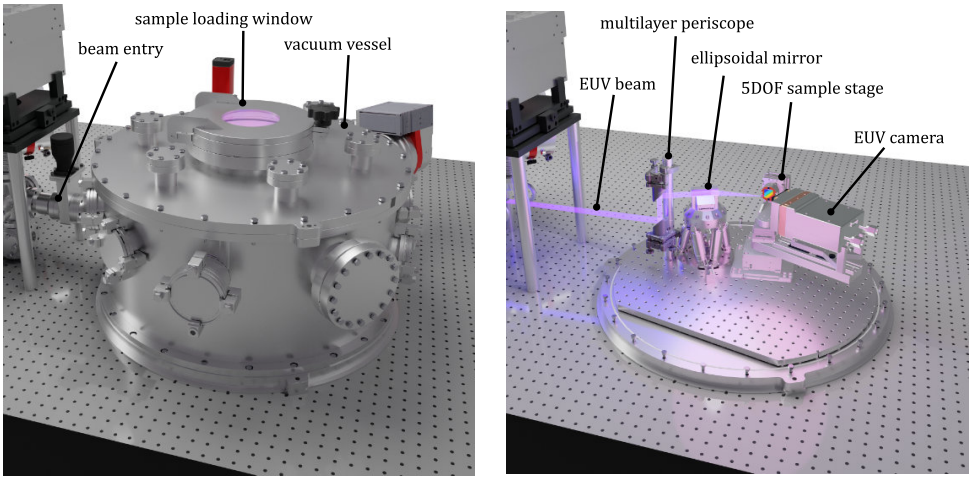

Figure 4.11: **Left:** A 3D render of the end-station attached to the HHG EUV source, enclosing the lensless imaging experimental setup. **Right:** When the exterior cylindrial construction of the vacuum vessel is removed from the 3D render, the lensless imaging setup is exposed, consisting of a periscope, the ellipsoidal mirror, the sample stage assembly and the EUV camera. It must be noted that all the infrastructure going into the chamber through the flanges and other parallel equipment such as a conventional visible microscope normal to the sample plane are not shown in this render.

4.4.2. HARMONIC FILTERING

Although it has been shown before that lensless imaging techniques such as ptychography can be operated with multiple wavelengths [26–28], having a narrow spectral bandwidth simplifies the ptychography reconstruction drastically. Therefore, some spectral filtering is desired. As has been described before, a rather broad bandpass filter has been applied to the HHG EUV beam prior to the main vacuum chamber by means of a thin metallic foil stack. However, further spectral filtering is desired.

A periscope is implemented in the vacuum chamber, see Fig. 4.11, where two multilayer mirrors (Bragg reflectors) are placed at respective angles of 45 degrees. For the 13.5 nanometer wavelength, a stack of Molybdenum and Silicon layers (MoSi) is used, demonstrating a peak reflectivity of 0.4, as depicted in Fig. 4.12. The reflectivity is notably less compared to mirrors for EUV lithography or in reflective EUV lithography masks. These higher-end mirrors operate at much smaller incidence angles with respect to the normal when compared to our 45 degrees, e.g. at a reflective mask in EUV lithography it is only 6 degrees, which are better conditions to design a Bragg reflector in the EUV regime. For the 18 nanometer wavelength, a ZrAl stack is applied instead with a peak reflectivity of 0.48. It is important to note that these reflectivity curves are calculated estimations provided by the mirror supplier NTT-AT. The mirrors have to be manually swapped and re-aligned when a switch of wavelength is desired, making it far less 'turn-key' than the EUV source's ability to switch wavelength.

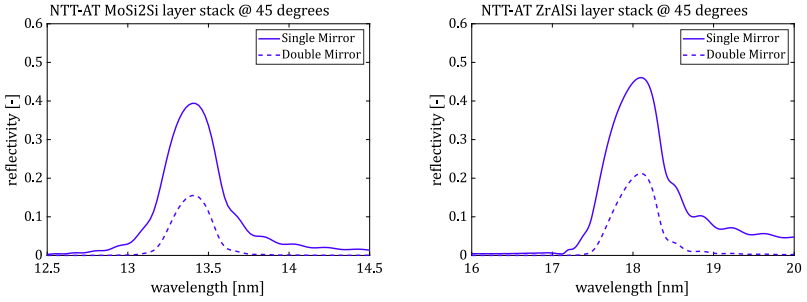

Figure 4.12: A set of multi-layer mirrors are used in the periscope to select a narrow bandwidth of the HHG spectrum. For 13.5 nanometer a stack of MoSi is used with a calculated peak reflectivity of 0.4 as shown in the figure on the left. The figure on the right shows the calculated reflectivity curve for 18 nanometer with a ZrAl stack. The reflectivity curves are calculated by the supplier of the mirrors, NTT-AT Corporation.

The spectral reflectivity can be slightly shifted with respect to wavelength by changing the angle of incidence on the mirror as shown in Fig. 4.13. This could be used to broaden the total spectral bandwidth of the mirrors. Changing the angle of incidence on the mirrors will also change the optical path of the EUV beam relative to ellipsoidal mirror resulting in misalignment.

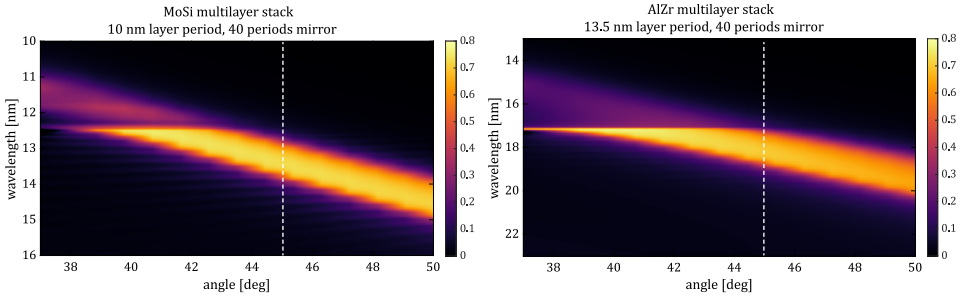

Figure 4.13: The spectral reflectivity of the multiylayer mirrors can be tuned to some extent by tuning the angle of incidence. Notice the sharp absorption edges at 12.3 nm and 17 nm related to silicon and aluminium. The data used in figure are retrieved from the CXRO database [17].

4.4.3. OPTICAL DESIGN OF ILLUMINATION SYSTEM FOR EXTREME UV AND SOFT X-RAY PTYCHOGRAPHY

Although we have been addressing the lensless aspect of ptychography in Chapter 2, some optical components are still required to efficiently collect EUV light from the HHG source and focus it on a target of interest. In Fig. 4.14, there are some examples of types of (illumination) optics in this wavelength regime. Among the diverse types of EUV optics, Fresnel zone plates are often used in research applications as they can be fabricated in a typical university nano-fabrication lab, and they have decent focusing capabilities [29–33]. However, the typical acceptance NA of a zone plate is limited as the radial line width of the concentric rings needs to be reduced towards the edge of the aperture. This limits the size of the zone plate to typically a few hundred micron, making their photon flux efficiency too low.

Toroidal mirrors, with their torus-like shape, offer advantages because they are relatively easy to manufacture [34] and are commonly employed in beamlines and monochromators in synchrotrons [35–38]. However, at conditions close to grazing incidence, these types of optics can contain significant amounts of coma and spherical aberrations.

Kirkpatrick-Baez (KB) mirrors [39], which consist of two orthogonal curved mirrors, focus the light horizontally and vertically (or vice versa) separately. These mirrors introduce limited aberrations and are relatively easy to manufacture, for which they are often used in synchrotron applications. Using two optics puts higher requirements on the optomechatronic control in a vacuum environment and will therefore yield additional complexity and costs.

Spherical mirrors are often chosen due to their relative ease of fabrication and because they have large tolerances in terms of alignment when compared to off-axis optics such as ellipsoidal mirrors. Initially, a dual spherical mirror system was designed for this beamline as shown in Fig. 4.15. The angle of incidence relative to the normal has be to minimized in order to limit spherical aberration. In our case a maximum angle of incidence of 2.5 degrees was possible, limited by the system dimensions and clipping of the beam paths without introducing too much spherical aberration. The curvatures of mir-

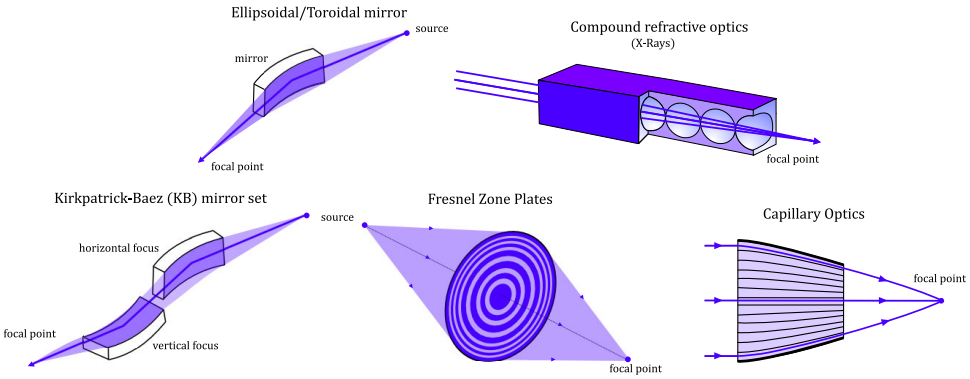

Figure 4.14: A selection of short-wavelength optics each tailored to collect and manipulate light. The ellipsoidal, toroidal and Kirkpatrick-Baez (KB) mirror set operate off-axis, in grazing incidence conditions. On-axis optics include diffraction based optics like Fresnel zone plates or refractive optics like compound optics. Except for the compound refractive optics (as they are more suited for hard x-rays), all are valid options to illuminate targets for lensless imaging in the EUV or SXR regime. Spherical mirrors, not depicted in this figure, with a multi-layer coating are also an option but have to be operated at near normal incidence to limit spherical aberration.

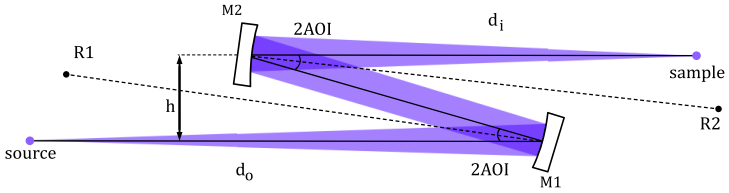

Figure 4.15: As mentioned before, spherical mirrors with a multi-layer coating could be used as well for illumination. A dual spherical mirror system was initially considered for the EUV beamline. The mirror set had a double function of imaging the source on the sample and to change the beam height h. This initial concept had a relatively small illumination NA of 0.0017, due to a small angle of incidence of 2.5 degrees in order to limit spherical aberration.

ror 1 (M1) and mirror 2 (M2) was optimized using raytracer software Code V[2] resulting in a radius of 2660 mm for M1 and 642 mm for M2. When the sample is illuminated at normal incidence, it would result in a probe size of roughly 10 µm, as shown in Fig. 4.16. In a tilted orientation of 20 degrees relative to the surface the probe significantly stretches in the horizontal direction up to 71 µm.

In order to reflect EUV at this angle of incidence, the substrate has to be coated with a multi-layer making it only functional for a small spectral bandwidth in the order of a few nanometers. This optical design was implemented for testing at 13.5 nm but was not used for actual ptychography experiments reported in this thesis, due to delays in the arrival times of crucial components required to perform experiments (e.g., the mechanical

[2] Ray-tracing simulations in Code V and paramater optimization, resulting in the design of the spherical and elliposidal mirrors, have been done by Dr. Ir. Yifeng Shao at the Optics Research group of Delft University of Technology.

stages to move a sample, section 4.4.4).

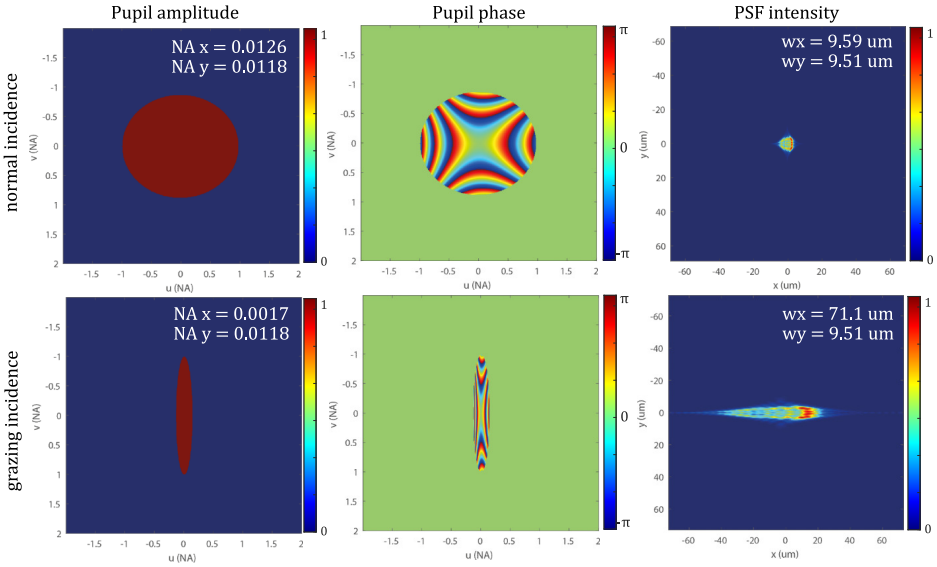

Figure 4.16: The optical performance of a set of spherical mirrors as shown in Fig. 4.15, with radii of R1 = 2660 mm and R2 = 642 mm for M1 and M2 respectively. When the sample is illuminated under normal incidence, the pupil function is close to symmetrical, resulting in a probe (PSF) with an extent of about 10 µm. When the sample is illuminated under an angle of 20 degrees with respect to the surface, the probe elongates in the tilt direction to 71 µm.

Beyond these conventional types, the field of EUV optics recently got extended with meta-lenses and other advanced diffractive elements [40]. Capillary optics [41–44], employing narrow, tube-like structures, are mainly used for focusing Soft to Hard X-Ray light through internal reflection, which is beneficial in compact and specialized instruments. For EUV and the lower-end of the soft X-Rays spectrum these capillary type of optics tend to be quite inefficient.

Instead, an ellipsoidal mirror has been designed and implemented into the EUV ptychography beamline. These off-axis optics allow for direct light collection and focusing with a single optical element. An ellipsoidal shape has two defined foci, as shown in Fig. 4.17, and is further characterized by three width parameters a, b and c. The full ellipsoid can be described accordingly,

$$\frac{x^2}{a^2} + \frac{y^2}{b^2} + \frac{z^2}{c^2} = 1, \tag{4.1}$$

with (x,y,z) being Cartesian spatial coordinates. Each ray originating from one focus will reach the other focus independently of its wavelength and without any aberrations, yielding perfect imaging when perfect alignment and a point source is assumed. In reality we will not have the full ellipsoidal surface but rather a subsection matching the input NA of the EUV beam as shown in the 3D representation of the ellipsoid in Fig. 4.17.

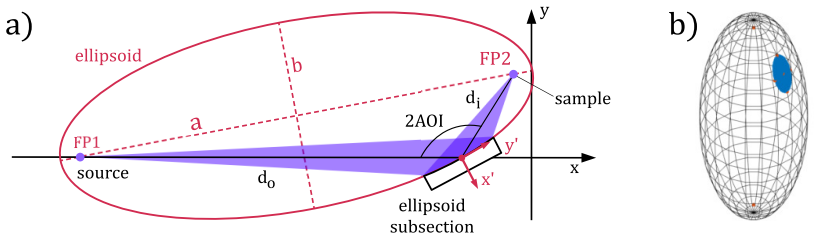

Figure 4.17: Schematic representation of an ellipsoidal mirror used in a focusing system for EUV (extreme ultraviolet). The diagram illustrates the path of EUV radiation from the source to the sample. A subsection (shown in black) of the total ellipsoid (shown in red) captures the light from the EUV source (in FP1) and focuses the light onto the sample (in FP2). The source is positioned at one focal point of the ellipsoid, while the sample is placed at the other. Twice the angle of incidence (AOI) is marked as 2AOI, with distances d_o and d_i indicating the respective positions of the source and the image from the mirror surface. A three-dimensional representation of an off-axis ellipsoidal reflector is shown on the right, with the highlighted area indicating the subsection used for focusing.

The ellipsoidal mirror is designed for an incoming angle of incidence (AOI) of 10 degrees relative to its the surface, allowing for high reflectivity without requiring multi-layer coatings. With a source distance of 1250 mm and an image distance of 160 mm, an ellipsoidal surface with a long axis of a = 705 mm and with the other axis given by b=c= 77.66 mm have been found as an ideal ellipsoid. Making b and c equal to each other results in a rotationally symmetric ellipsoid along the a-axis (long axis), simplifying the manufacturing to some degree. A ray-traced PSF of 2.44 by 0.42 µm has been found using CodeV[3].

The figure error of the manufactured ellipsoid (by NTT-AT) is measured by the supplier, where a figure of merit of 0.75 mm peak-to-valley and 0.17 RMS has been found. This yields a long axis of 704.84 mm and 77.68 mm for the short axis. The surface roughness of the mirror substrate has been measured in a small region of 300 by 300 µm with a Zygo white light interferometer of the manufacturer NTT-AT, yielding a surface roughness of 0.385 nm (RMS).

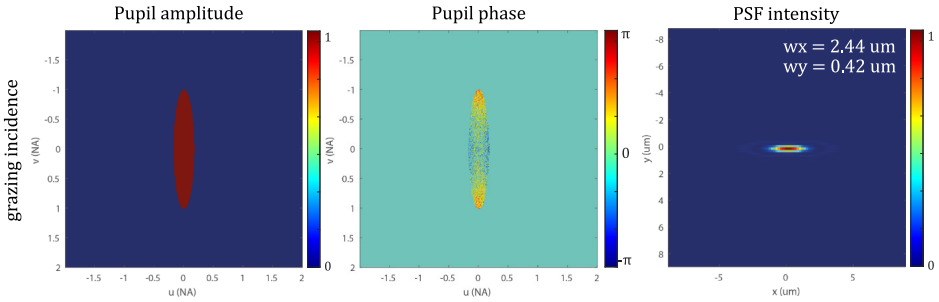

Figure 4.18: The designed ellipsoidal mirror with parameters a = 705 mm and b=c= 77.66 mm is illuminated at a grazing incidence angle of 10 degrees. A ray-traced probe of 0.42 by 2.44 µm is formed in the focus of the ellipsoid.

[3] See footnote 2 on page 60

The mirror substrate has been coated with a single 50.4 nm layer of ruthenium. At the shallow angle of incidence of 10 degrees relative to surface, the calculated peak reflectivity is 92% at 12.5 nm [17]. For the relevant wavelengths of 13.5 nm and 18 nm, a calculated reflectivity of 89% and 78% respectively has been found, making it suitable for a broader spectral range compared to multi-layer based optics.

Some optomechanical control is required to move the ellipsoidal mirror within the vacuum system. The original setup involved mounting the ellipsoidal mirror on an open-loop five degrees-of-freedom (DOF) piezo system (Newport 8081M-UHV XYZTxTy), as shown in Fig. 4.19. Because it is an open-loop configuration and two pairs of piezo motors in the five motor configuration are non-linearly coupled, this setup was later upgraded to a more advanced six DOF hexapod (a vacuum-compatible version of the PI H8.11, Physik Instrumente PI).

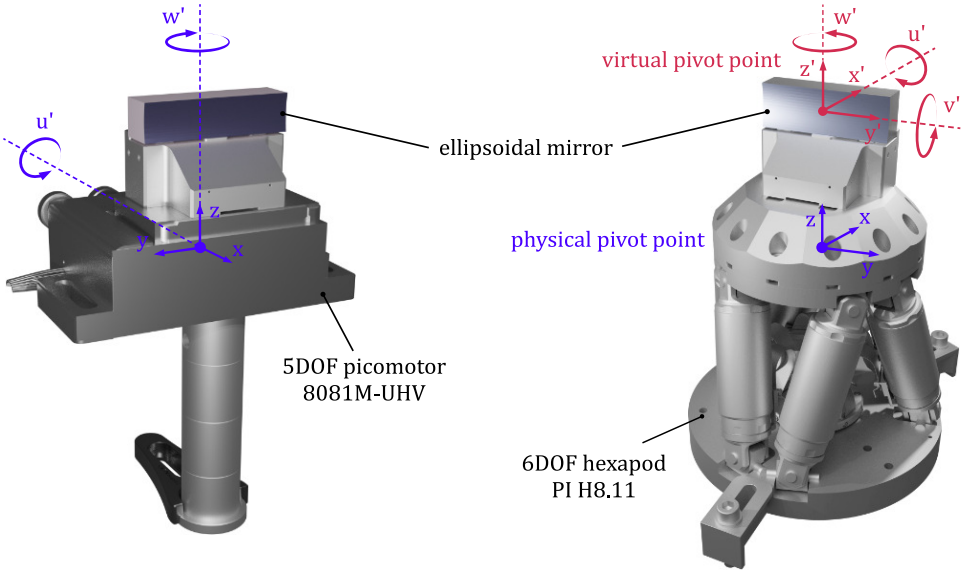

Figure 4.19: Left: Initially the ellipsoidal mirror was mounted on top of an open-loop five degree-of-freedom (DOF) piezo system (Newport 8081M-UHV XYZTxTy). Being open-loop and having 5DOFs and coupled piezo motors, it was eventually upgraded to a vacuum-compatible six DOF hexapod PI H8.11 (right figure). The physical coordinate system and thus the pivot point lies in the center just below the mounting plate. The mirror optical axis and the physical pivot point are not aligned, however through software, this point can be virtually moved in space. In our case the virtual pivot point is placed 69.75 mm higher in the center of the optic based on the technical drawings.

The actual experimental performance of the illumination optics will be considered in Section 4.5 and Chapter 5.

4.4.4. REFLECTION-MODE GONIOMETRIC EUV LENSLESS MICROSCOPE

We have reached the final assembly in the entire beamline, the actual reflection mode lensless microscope for EUV. The focused light from the previously described ellipsoidal

mirror illuminates a sample of interest. After the light interacts with the sample, it propagates towards an EUV-sensitive camera. In this subsection, we describe this assembly as shown in Fig. 4.20 in more detail.

A conical custom sample mount has been designed to hold patterned samples with dimensions up to 20 by 20 mm with a maximum thickness of 750 µm. The conical mount has a cylindrical magnet clamped in the bottom and three V-grooves, which facilitate kinematic coupling with the stage stack, as depicted in the Fig. 4.20. This allows for a relatively quick and easy sample swap process, where the pump-down process of the vacuum chamber is the bottleneck when performing a sample swap. The sample holder is placed on a stack of five slip-stick piezo-driven stages, enabling precise manipulation of the sample in various directions.

The movement of the sample in the X, Y, and Z axes is controlled by three linear stages, specifically the SmarAct CLS-5252 models. The slip-stick approach allows these stages to have a relatively large travel range of 30 mm with an accuracy of around one nanometer. Additionally, the setup includes two slip-stick rotation stages (SmarAct SR-5014) to control azimuth and angle of incidence (AOI) with an accuracy of 15 µrad and infinite travel range. The stacking order of the stages from the mounting point up to the sample is Z, AOI, X, Y and azimuth. The stacking orientation of the stages for Z and AOI ensures that the rotation axis relative to the sample plane remains fixed if the Z-axis is moved. The downside of this approach is that Z is only occasionally orthogonal with X and Y.

These slip-stick piezo stages have a large travel range while maintaining high accuracy and can handle a significant load (>20N) normal to the travel direction. Their holding force in the travel direction is limited, with only 3.5 N. The weight of the azimuth stage and the sample mount combined is close to this maximum value, decreasing the accuracy and stability of the stage. Therefore, a compensation leaf spring with a spring force of 1.9 N is added as a counterforce.

Ultimately, we want to measure diffraction patterns originating from the sample plane with an EUV-sensitive camera. The specular reflection from the sample hits the camera in the center of the detection area at normal incidence. To keep the specular reflection in the center and normal to the camera, we need to be able to rotate the camera around the sample goniometrically.

A full vacuum-compatible EUV-sensitive camera allows for flexible placement and will enable us to rotate around the azimuthal axis (ν_s) of the sample. The Princeton Instruments PI-MTE3 [45] is such a device. The EUV camera is mounted on a manual linear rail[4], allowing to change the distance between the camera and the sample plane. This assembly is mounted on a stepper motor driven rotation stage (Newport URS75BPPV6). This rotation stage and the piezo-driven stage, which controls the angle of incidence of the camera and sample, can each move over 360 degrees individually. Due to geometric limitations, however, the AOI can only be changed between 0 and 30 degrees relative to the surface of the sample, depending on the camera's location relative to sample (propa-

[4] As this is mounted on a manual linear rail it can only be moved in air conditions, i.e. not under vacuum conditions. This is one of the recommendations of potential future upgrades, see Section 4.6.

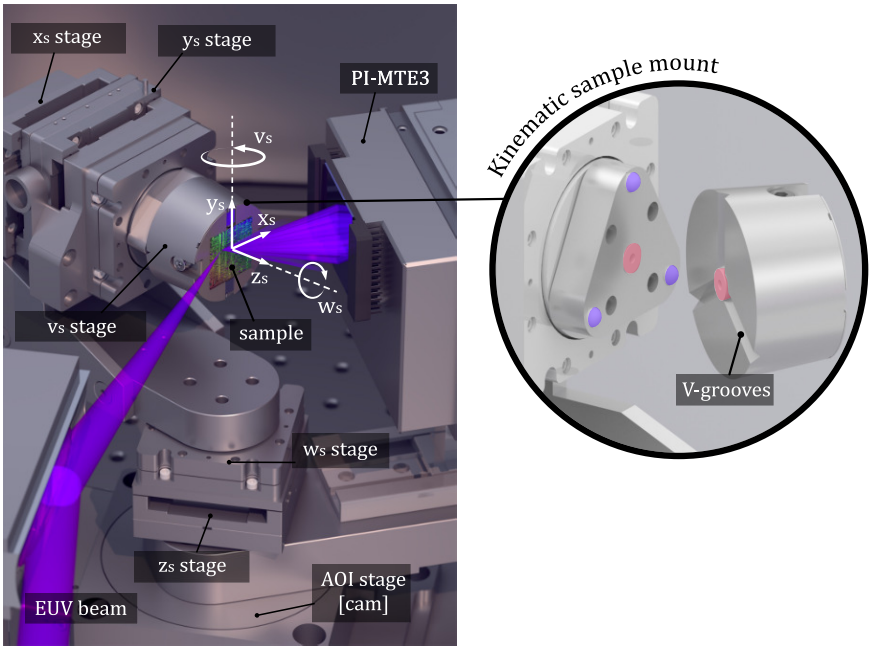

Figure 4.20: A sample, of up to 20 by 20 mm, can be clamped in a custom made conical sample mount. The sample holder is attached on a series of five slip-stick piezo-driven stages. Movement of the sample in the X, Y, and Z directions is enabled by three linear stages (SmarAct CLS-5252), while azimuth (labelled with w_s) and angle of incidence (AOI) (labelled with v_s) movement are driven by two rotation stages (SmarAct SR-5014). To maintain the normal camera alignment with respect to the specular reflection, the EUV-sensitive camera (PI-MTE3) is mounted on a rotation stage (URS75BPPV6) which rotation axis is aligned with the AOI rotation axis of the sample (v_s). The circular inset on the right shows the mounting mechanism of the sample mount onto the stages via two magnets (shown in red), three V-grooves and three spherical contact points (shown in blue). This method ensures kinematic coupling to the stage stack.

gation distance). This could be changed by making the coolant tubes of the EUV camera more compact, moving the ellipsoidal mirror further back or (of course) increasing the volume of the vacuum vessel.

The PI-MTE3 is equipped with a large back-illuminated CCD sensor (e2v CCD230-42) of 30.7 by 30.7 mm divided in 2048 x 2048 pixels with a pixel size of 15 µm. The CCD is cooled through a water-cooled Peltier element. The Peltier element can cool the CCD down to -55 °C, reducing the dark current to 0.0106 electrons per pixel per second. The low dark current, combined with 16-bit depth and a 177.000 electron well depth, enables a relatively large dynamic range.

The pixel array can be read with different readout rates (4 MHz, 1 MHz and 100 kHz) and gains (approx. 6, 2 and 1 electron per count). Given the 4 megapixels, the quickest readout time is 1 second, limiting the frame rate to lower than one frame per second. The camera has four readout ports to increase the readout speed by a factor of four. However, each port has slightly different gains and noise statistics, requiring more data processing

to correct for this effect. During the readout sequence, the camera still accumulates charge when exposed to light. A mechanical shutter is necessary to block any EUV light from hitting the camera during the readout sequence, with a minimum opening-closing time of 12 ms.

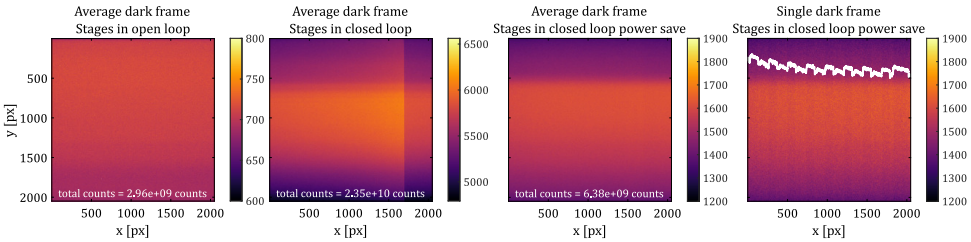

Figure 4.21: The SmarAct stages implemented in the microscope use IR interferometers in their encoders to determine the location of the stage. This light leaks out of the stages which can be observed in the background signal on the camera when comparing the open loop, closed loop and power save mode background frames. These examples are acquired at 200 ms exposure time and are averaged 10 times. The total power on the camera reduces significantly when in power save mode. However, when looking at an individual frame a banding pattern can be observed, emphasized with the white colored plot overlapping the right image. This is caused by the blinking of the optical encoders which are still emitting light during the read out phase of the camera.

Despite the low dark current and readout noise, some background light is present in the dark frames as shown in Fig. 4.21, limiting the dynamic range. This additional signal originates from the piezo-driven stages, which are controlled through optical encoders leaking IR light within the vacuum chamber. A sharp shadow is cast onto the camera, and a non-uniform distribution is observed. This background light can be removed by operating the stages in an open-loop configuration or reduced in a power-save mode where the camera is less often controlled.

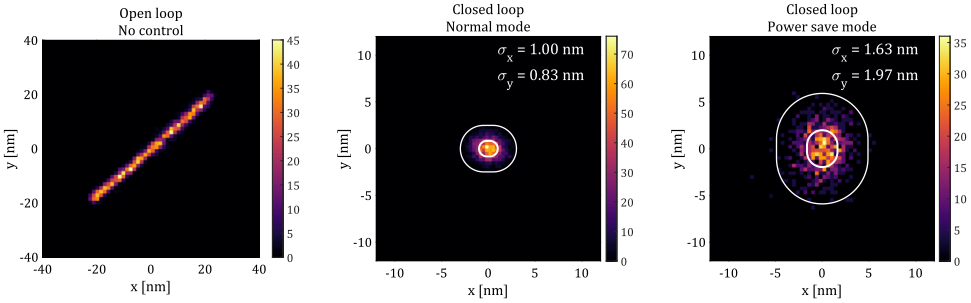

Figure 4.22: The sample stages can operate in three modes namely, open loop, closed loop and closed loop in a power save mode. The figure shows the statistics of recorded positions of the stages in X and Y over half an hour. When operated in open loop, there is no control of the stages and therefore the system drifts away from the starting point. In closed loop, normal mode, the stages are maintained within a nanometer. In a power save mode, the stages are updated at a lower refresh rate compared to the normal mode, at the cost of accuracy resulting in a stability of about 2 nm. The white ellipses represent the σ and 3σ in the x and y direction.

The power save mode and open-loop have an average of 3.6 and 7.9 times less total background counts, respectively. For optimum dynamic range, one would operate in the

open-loop configuration at the cost of completely losing the high precision and control of the piezo stages, as shown in Fig. 4.22. The X and Y stages linearly drift away from the set point in an uncontrolled manner and can therefore, not be used. In the power save mode however, the stages remain stable within an acceptable 2 nm compared to 1 nm in the normal closed-loop mode.

A side effect of the power save mode is a "banding effect" observed in a single dark frame. As the optical encoders operate at a reduced rate (i.e blinking at a lower rate), these frequencies are slow enough to be observed during the readout sequence in vertical bands as shown in Fig. 4.21. These bands move horizontally per shot but are averaged out in the final acquired dark frame which is used to correct the recorded images of the diffraction patterns in the ptychographic image series.

4.5. OPTIMIZING AN ELLIPSOIDAL MIRROR ALIGNMENT USING SENSITIVITY ANALYSIS FOR ILLUMINATION

The light from the EUV source is collected by an ellipsoidal mirror and focused onto the sample of interest. The alignment of the mirror is essential as it affects the maximum achievable resolution. It must be stressed that aberrations or structures in the final probe are not necessarily problematic for lensless imaging, unlike conventional imaging techniques, as the probe and object are computationally separated. However, the size of the probe is crucial as it determines the minimum distance between the sample and the camera (i.e., the collection NA).

An initial rough alignment is performed with infrared light, as it is easier to operate due to its higher photon flux and does not need to be performed in a vacuum. A conventional 8-bit CMOS camera (SVS-Vistek eco183MGE) is mounted on a SmarAct linear stage (SmarAct SLC-2445), which allows for translation along the propagation axis. The repetition rate of the laser is reduced to limit the amount of overexposure of the camera.

Finding the focal plane is a challenge, considering the relatively large pixel size, the size of the probe, and the overexposure of the camera. Placing a binary transmission Bahtinov mask, consisting of three sections with two diagonal gratings and one horizontal grating, as close as possible to the ellipsoidal mirror results in additional diffraction orders to the probe in the focal plane. These spokes align and cross in the 0^{th} when in the focal plane, see Fig. 4.23 and Fig. 4.24. Bahtinov masks originate from the astronomy and astrophotography community, where they are used to ensure proper focusing of point-like objects in the night sky such as stars [46, 47].

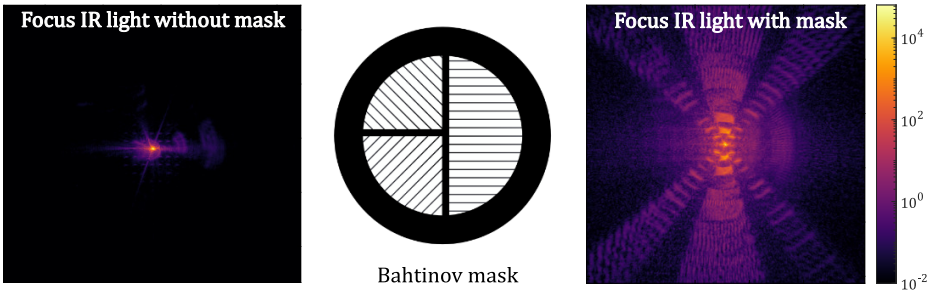

Figure 4.23: Without introducing any attenuation (or reduced repetition rate) of either the IR beam or EUV beam, capturing non-overexposed images of the beam near the focus becomes rather tricky. At a lower flux, non-overexposed images can be made without much detail due to the rather large pixels and a small probe when performing a through-focus scan. Placing a binary transmission Bahtinov mask, consisting of three sections with two diagonal gratings and one horizontal grating, as close as possible to the ellipsoidal mirror results in additional diffraction orders in the focal plane. The 0^{th} still closely represents the probe without a mask, but the energy is more dispersed across the camera, relieving the exposure problem. The main benefit of the mask is the ability to find the focal plane, as shown in Fig. 4.24. Note that the image on the right is on a log scale.

After this initial rough alignment, the CMOS camera is removed and replaced by an EUV camera (PI-MTE3) mounted on the linear stage. The combination of the EUV camera and the stages is mounted onto the rotation arm of the goniometric EUV lensless microscope unit. Note that the sample stages (X, Y, Z and two rotational stages) need to be removed for this procedure, and the camera is mounted in a non-ideal manner as the stages are relatively small. In the ideal case, one would use an additional dummy stage to support the camera and mill a layer off the rotation arm to compensate for the stage thickness. This would allow for permanent installation of the linear stage when performing ptychography experiments, as is suggested in the future outlook of Section 4.6.

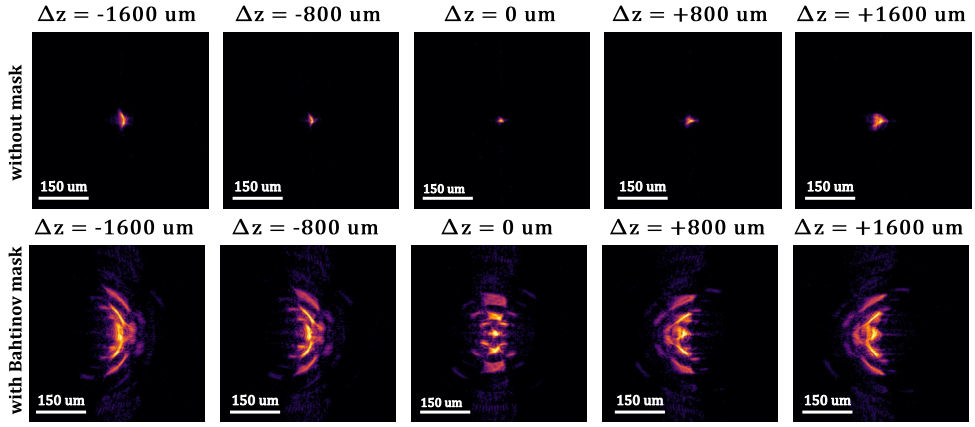

Figure 4.24: Top-row: Example of a through focus scan in normal operation. The images are cropped from 2050 by 2448 pixels down to 256 by 256 pixels, where still not much details of the probe can be retrieved. With the lack of detail, it becomes rather challenging to find the focal plane. Bottom-row: When introducing a Bahtinov mask just after the ellipsoidal mirror, we can observe diffraction orders, which distort and shift while scanning the camera through the focal plane. This visual feedback helps to find the focal plane and initial rough alignment of the ellipsoidal mirror.

4.5.1. JACOBIAN SENSITIVITY MATRIX

Following the initial rough alignment, as outlined in the previous section, further alignment is needed. Aligning an off-axis ellipsoidal mirror with six degrees of freedom manually is non-trivial especially with the limited resolution of the EUV camera restricting the amount of detail in the probe beyond the minimum beam waist at the focal plane. To further improve the alignment we implement an iterative gradient descent optimization routine to help in the process.

This optimization approach relies on a sensitivity matrix or the Jacobian matrix S, which includes the sensitivity (or gradient) of each observable y_m relative to each input x_n. In practical terms, these observables y_m are key performance indicators (KPIs) such as the minimum beam waist or aberrations (e.g., expressed in Zernike modes), while the inputs x_n represent the position of the mirror actuators. Adjusting the actuators by Δx prompts a corresponding change in the observables by Δy (which is observable-dependent) with a certain amount, where the degree of change indicates its sensitivity.

$$\Delta y = S\Delta x \quad \text{with} \quad S = \begin{bmatrix} \frac{\partial y_1}{\partial x_1} & \cdots & \frac{\partial y_1}{\partial x_N} \\ \vdots & \ddots & \vdots \\ \frac{\partial y_M}{\partial x_1} & \cdots & \frac{\partial y_M}{\partial x_N} \end{bmatrix}. \tag{4.2}$$

Subsequently, we define a loss function $\mathcal{L}_m$ for each observable, quantified by the difference between its current value y_m and the desired target value $\tilde{y}_m$. Weight values w_m are assigned to each loss term $\mathcal{L}_m$ within $\mathcal{L}$, in order to adjust the learn rate for each observable.

$$\mathcal{L} = \begin{bmatrix} w_1 & \dots & w_M \end{bmatrix} \begin{bmatrix} \mathcal{L}_1(y_1, \tilde{y}_1) \\ \vdots \\ \mathcal{L}_M(y_M, \tilde{y}_M) \end{bmatrix} \quad \text{with} \quad \mathcal{L}_m(y_m, \tilde{y}_m) = (y_m - \tilde{y}_m)^2. \tag{4.3}$$

We then construct a gradient matrix **G**, which contains the gradient of the loss function for each observable relative to each input. This matrix shows which adjustments are most effective in reducing the overall loss, i.e. reaching the set target values of the observables.

$$\mathbf{G} = \begin{bmatrix} w_1 & \dots & w_M \end{bmatrix} \begin{bmatrix} \frac{\partial \mathcal{L}_1}{\partial x_1} & \cdots & \frac{\partial \mathcal{L}_1}{\partial x_N} \\ \vdots & \ddots & \vdots \\ \frac{\partial \mathcal{L}_M}{\partial x_1} & \cdots & \frac{\partial \mathcal{L}_M}{\partial x_N} \end{bmatrix} \tag{4.4}$$

Using the chain rule, we can decompose each term $\frac{\partial \mathcal{L}_m}{\partial x_n}$, simplifying the problem to,

$$\frac{\partial \mathcal{L}_m}{\partial x_n} = \frac{\partial \mathcal{L}_m(y_m, \tilde{y}_m)}{\partial y_m} \frac{\partial y_m}{\partial x_n} = 2(y_m - \tilde{y}_m) \frac{\partial y_m}{\partial x_n}. \tag{4.5}$$

This enables us to iteratively optimize the system by updating the position of the actuators $\mathbf{x}^{k+1}$ based on the gradient matrix and a preset "overall" learning rate γ with k indicating the current iteration or epoch number,

$$\mathbf{x}^{k+1} = \mathbf{x}^k - \gamma \mathbf{G}(\mathbf{x}^k) \tag{4.6}$$

The system should gradually converge towards the desired configuration, minimizing the overall loss. Practically, in order to populate each term in **G**, we need to retrieve the current values of the observables y_m and their respective gradients $\frac{\partial y_m}{\partial x_n}$. In our case, we are interested in the minimum beam waist and astigmatism and would like to minimize both values. These observables can be retrieved by performing a through focus scan and

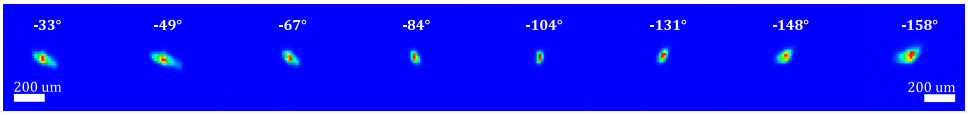

Figure 4.25: Several frames along the propagation axis are acquired for the EUV probe at 18 nanometer to form a through focus scan. Each frame is rather limited in resolution due to the large pixel size of the EUV sensitive camera (PI-MTE3) which are 15-by-15 micron in size. Despite the low resolution, a rather aberrated probe can be observed considering the tails and shape of the probe. The angle denoted in each frame refers to the rotation found in the 2D Gaussian fit.

fitting a Gaussian beam, yielding a minimum beam waist in x and y direction and their location relative to each other in the z-direction. This difference in the z direction we use to quantify the amount of astigmatism. In order to retrieve the gradients per observable we perturb each input slightly such that the observable change linearly. A linear function is fit to retrieve the gradient.

In our case we would like to minimize our target values $\tilde{y}_m$ of the observables (minimum waist and astigmatism) and set therefore $\tilde{y}_m$ equal to zero. The optimization process of the sensitivity matrix starts with a learning rate of 0.1. We assign weights of 10 and 1 for the beam width and astigmatism, respectively. After 40 epochs, the loss function reaches a plateau. Notably, astigmatism experiences a significant reduction, whereas the beam width appears unaffected. This observation holds true when examining the through-focus scan before and after optimization, as illustrated in Fig. 4.27. This method requires quite a lot of through focus scans. For a single gradient $\frac{\partial y_m}{\partial x_n}$ we need at least three through focus scans. Practically, we acquire six through focus scans for each input to fit a better linear function. With five or six degrees of freedom, this would lead to 30 to 36 through focus scans for a single iteration in the gradient descent process. As a result, for just 40 epochs it took about 14 hours of experimental time.

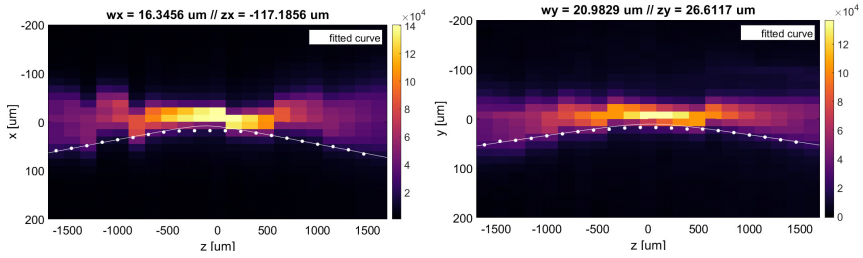

Figure 4.26: The frames acquired along the propagation axis are integrated along the horizontal and vertical direction and are shown in the background of the plot. On top of that are the values retrieved by fitting a 2D Gaussian function in each frame over which a Guassian beam is fitted. The fitted Gaussian beam yields our observables for the sensitivity matrix, being the minimal beam waist w_x and w_z as well as astigmatism Δz. The astigmatism is defined as the distance between the waist locations in the z-direction, which is 143 microns in this example.

This method could be further improved by using the hexapod instead of the five degrees of freedom system. Additionally, more observables can be used, for example Zernike

modes from a retrieved wavefront. The wavefront could potentially be retrieved through a phase retrieval method, such as a Gerchberg-Saxton type of approach by using the different frames acquired in the through focus scans. This could be a topic for future research.

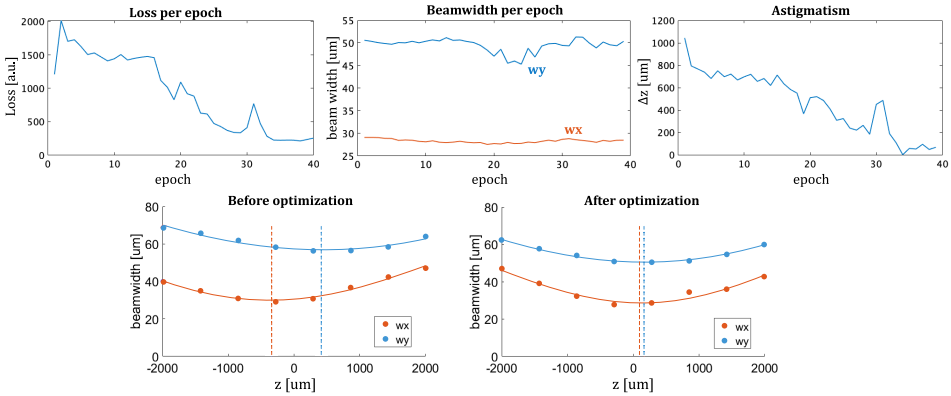

Figure 4.27: The sensitivity matrix optimization process is initiated with a learning rate of 0.1. For the observables a weight of 10 and 1 is set for the beam width and astigmatism respectively. After 40 epochs the loss function stagnates. The astigmatism is significantly reduced while the beam width does not seem to be affected. The same conclusion can be drawn when comparing the through-focus scan before and after optimization, as depicted in the figures in the bottom row.

4.6. POSSIBLE FUTURE IMPROVEMENTS OF THE EXTREME UV BEAMLINE

Although a functional setup has been designed, built and tested from scratch, some parts could be improved in hindsight. The purpose of this section is to summarize a few of them.

PULSE COMPRESSION AND BEAM STABILITY CONTROL

The 300 fs pulses from the drive laser must be compressed for efficient harmonic generation. This is achieved by coupling into a 200 µm hollow core fiber (HCF) and a chirped mirror set for further compression down to 30 fs. This approach works up to reasonable levels of satisfaction, but is pretty lossy as more than 32% of the IR power is dissipated in the fiber. On top of that, manually optimizing the coupling into the fiber with a uniform "single mode" at the output is not an easy task. This optimization can only be done at lower power to avoid fiber damage. When the system is operated at full power, the beam tends to drift to a different position due to the newly introduced thermal load, and self-focusing effects start to appear, reducing the in-coupling quality. Adding the two extra motorized mirrors before the HCF allows for a controlled way to couple into the fiber, making this process easier, quicker and more reliable.

Setups with a multi-pass gas cell compression approach [48, 49] have successfully compressed pulses to even single-cycle pulses for high repetition rates with very high

throughput (>90%). Tuning these multi-pass cells might be challenging, and the side effects of self-focusing, thermal drift and pointing stability have yet to be reported.

Other techniques like loose focusing in a low-pressure gas [50] might be suitable to avoid in-coupling challenges, strong self-focusing effects and beam stability effects. Further investigation is needed to determine if this approach is suitable for driving lasers with higher average power, lower pulse energies and higher repetition rates.

As reported in Section 4.2, the beam of the drive laser is stabilized through a μAligna beam stability unit just before the non-linear compression unit. After the compression, there is no control of beam stability and therefore as an effect, any changes made after the HCF result in a misalignment in the entire beamline downstream. On top of that, any thermal effects caused in the fiber or optics after the compression are not compensated and can result in higher beam-pointing errors of the generated EUV beam.

REPEATABILITY AND LONGEVITY

The repeatability and longevity of the system are a real bottleneck in the EUV beamline. The high harmonic generation source including the IR drive laser are the main source of causing down-time and low repeatability. As mentioned before, the current implementation of the hollow core fiber (HCF) requires a lot of (manual) re-alignment changing slightly the in-coupling conditions causing quite some down-time. Initially it was expected that the fiber, with its fixed input and output aperture of 200 μm, would reliably fix the beam path post compression. Therefore, it was expected, if the beam would be coupled into the fiber everything downstream would be pretty much aligned. However, this is not true and therefore some more alignment and optimization is required once this procedure has been done. Adding a beam stabilization unit at the output port leads to a "check-point" of the system, meaning that any changes made before this check-point will not cause any misalignment downstream. Replacing the HCF with the aforementioned multi-pass cell or loose focusing approach should improve repeatability and longevity as well.

The gas jet nozzle is currently mounted on an open-loop piezo drive stage with X, Y, and Z axes, which would ideally be upgraded to a closed-loop system for improved repeatability. Moreover, the gas catcher is fixed and unable to move under vacuum conditions. Consequently, adjusting the position of the gas jet during optimization affects the quality of the vacuum and increases the strain on the turbo molecular pumps. By mounting the gas catcher either on a coupled stage or on the same base as the gas jet nozzle would improve this significantly.

Ideally one would like to have an aperture close and far away from the EUV source as a reference point to ensure that the generated harmonics beam path is aligned (just like a common beam walk method). The current approach by using an aperture and the off-axis camera in the beam analzyer, on paper should be sufficient. A 45 degrees mirror is translated into the beamline using a 'linear' actuator to aim the beam towards the EUV camera. Unfortunately these 'linear' actuators are far from linear due to a wobble. On-top of that, due to the relative low reflectivity of the mirror the exposure time is not that high (order of 5 to 10 seconds) while being exposed to multiple wavelengths. Improv-

ing the reflectivity of the optic and use an actual linear actuator (or flip-mirror method) could improve the repeatability significantly.

CONTAMINATION AND HYDROCARBON DEPOSITION CONTROL

For any vacuum system, contamination control is crucial to remain at suitable low pressures and avoid contamination deposition on sensitive equipment. Two categories of contaminants can be identified, gaseous contaminants which can be pumped away. These are known as contaminants leading to increased partial pressure [51]. The second category is a contaminant that penetrates the chamber and remains there. For example, a greasy fingerprint caused by the operator within the vacuum chamber can take about a full day of pumping to eliminate the gaseous contaminants. After the gaseous contaminants are gone, it leaves a residue behind in the chamber. These can be avoided by working carefully and ultrasonically cleaning each item going into the chamber.

However, some level of contaminants will always be present in the chamber. The photon energies, in our case 68 eV (18 nm) or 92 eV (13.5 nm), are energetic enough to crack hydrocarbon and water molecules [52] that decompose, resulting in a film of carbon or oxide layer on the surfaces which are illuminated with EUV light. These films could degrade the reflectivity of the illumination optics and the detection efficiency of the EUV camera over time. This is especially a big issue in, for example, EUV lithography machines due to their high average power of EUV (compared to HHG) combined with many contaminant producers present in the chamber. Hydrocarbon-based resists, residues from high-speed stages or (although neither hydrocarbon nor water-based) tin contaminants from the laser-produced-plasma (LPP) EUV source leave contaminants within the chamber which damage the optics. The growth rate of these carbon layers can be on the order of 0.001 up to 0.01 nanometer per hour [53], which adds-up rather quickly for machines which operate 24/7.

Luckily, our HHG system does not run 24/7 and at those high powers where it has not been a noticeable effect so far in the EUV ptychography beamline. Nevertheless, over time, this could become problematic and significantly reduce the efficiency of the beamline, which is already an essential factor in HHG beamlines due to the relatively low photon flux.

Several approaches could be implemented to reduce contamination and therefore hydrocarbon cracking on critical surfaces. Adding a bake-out step, where the chamber is heated, to remove any water vapour can help with the downside of higher requirements on heat resistance of equipment.

Contaminants like to stick on cold surfaces due to lower kinetic energies of the particles compares to hot surfaces. In our case the camera is cooled down to -55 °C and is the coldest surface in the chamber and therefore it may suffer from a potential higher rate of deposition. Instead, adding a cryogenic cooled 'cold finger' in the chamber can help to collect contaminants, leading to an improved vacuum quality.

If hydrocarbon deposition does become problematic in the future, one could consider to implement plasma cleaners in each chamber to etch away the contaminants. Potential side effects of plasma cleaning on the equipment within the vacuum vessel is unknown.

ANNULAR BEAM FOR IMPROVED EFFICIENCY AND POLARISATION CONTROL

Significant amount of EUV light is lost by separating the generated EUV light from the IR light of the drive laser. This can be improved by replacing the last mirror before focusing the IR light in the HHG chamber by an annular mirror (i.e. a mirror with a hole drilled in the center), as shown in Fig. 4.28. This would make it possible to only separate the IR light from the generated EUV light without introducing any losses to the produced EUV, making the IR removal unit obsolete, as shown in [54]. As the center part of the IR beam is dumped, there is of course a loss in terms of IR power.

An additional benefit of this approach is that in contrast to grazing incidence plates, this method is not polarisation sensitive. Therefore, allowing for arbitrary polarisation input of the drive laser and the resulting EUV beam.

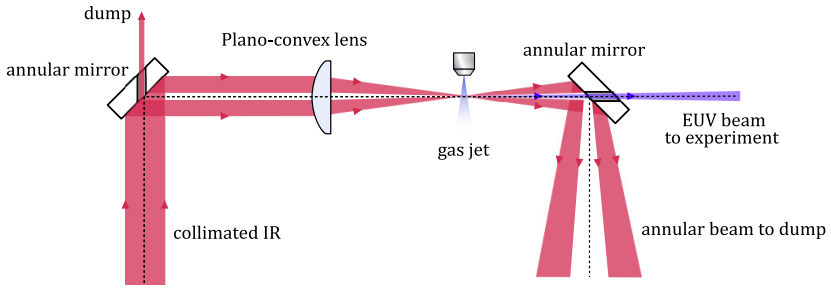

Figure 4.28: Swapping the last mirror in the IR source (right before the gas jet on the left) with an annular mirror could make the IR removal unit obsolete. The drive laser can be separated from the EUV without any losses and potentially increasing the efficiency of throughput.

MANUAL CONTROL OF IMAGING ASSEMBLY

The entire imaging assembly, i.e. the 5DOF piezo stages to control the sample, the EUV camera and its rotation stage, has to be placed near the focus of the EUV beam. In the initial alignment, this is done manually with the IR beam, as no vacuum conditions are required. When pumped down, this has to be repeated with EUV, but it can only be done by offsetting the z-axis stage of the 5DOF stage assembly. This slightly misaligns the rotation axis of the camera and the sample stage, which can be problematic for experiments which require rotational sweeps. Therefore, a stack of two additional manual stages which carry the entire assembly would be ideal to compensate for this, similar to the system in JILA [4].

HIGH-SPEED DATA ACQUISITION WITH CMOS TECHNOLOGY

The vacuum compatible EUV CCD camera has a limited readout rate of 4 MHz (which equates to 0.5 seconds of read out per full frame) and a limited minimum exposure time of 12 milliseconds. This can make High Dynamic Range (HDR) imaging a pretty slow method with the readout rate as the main bottleneck. Recently, CMOS technology has become available for the EUV range, which have significantly higher readout rates where a mechanical shutter is not needed anymore. Recent work has already shown the advantages of lensless imaging with CMOS technology implemented [55].

EUV CAMERA ON A MOTORIZED STAGE FOR PROPAGATION DISTANCE CONTROL

The EUV sensitive camera is mounted on top of a rail which allows the user to slide the camera over a certain distance relative to the sample. By replacing the rail with a motorized stage allows the user to change the propagation distance while under vacuum conditions. This could also help with the automatic alignment of the ellipsoidal mirror via the sensitivity matrix approach as this requires such a motorized stage. In the example given in Section 4.5, we temporarily mounted the camera on a motorized stage. However, this stage does not fit permanently while doing ptychography measurements due to the additional thickness of the motorized stage. By simply milling away some thickness of the arm which the camera is mounted on solves this issue.

BIBLIOGRAPHY

1. Porter, C. L. *et al.* General-purpose, wide field-of-view reflection imaging with a tabletop 13 nm light source. *Optica* **4,** 1552–1557 (2017).
2. Cousin, S. *et al.* High-flux table-top soft x-ray source driven by sub-2-cycle, CEP stable, 1.85-μm 1-kHz pulses for carbon K-edge spectroscopy. *Optics letters* **39,** 5383–5386 (2014).
3. Johnson, A. S. *et al.* High-flux soft x-ray harmonic generation from ionization-shaped few-cycle laser pulses. *Science advances* **4,** eaar3761 (2018).
4. Porter, C. L. *Complex Extreme Ultraviolet Imaging Reflectometry: Quantitative Lensless Imaging with Short-Wavelength Light in Reflection Geometries* (University of Colorado at Boulder, 2019).
5. Takahashi, E. J., Kanai, T., Ishikawa, K. L., Nabekawa, Y. & Midorikawa, K. Dramatic enhancement of high-order harmonic generation. *Physical review letters* **99,** 053904 (2007).
6. Takahashi, E. J., Nabekawa, Y. & Midorikawa, K. Low-divergence coherent soft x-ray source at 13 nm by high-order harmonics. *Applied Physics Letters* **84,** 4–6. ISSN: 0003-6951. eprint: https://pubs.aip.org/aip/apl/article-pdf/84/1/4/12249670/4_1_online.pdf. https://doi.org/10.1063/1.1637949 (Dec. 2003).
7. Takahashi, E. J. *et al.* Generation of strong optical field in soft X-ray region by using high-order harmonics. *IEEE journal of selected topics in quantum electronics* **10,** 1315–1328 (2004).
8. Ding, C. *et al.* High flux coherent super-continuum soft X-ray source driven by a single-stage, 10mJ, Ti:sapphire amplifier-pumped OPA. *Opt. Express* **22,** 6194–6202. https://opg.optica.org/oe/abstract.cfm?URI=oe-22-5-6194 (Mar. 2014).
9. Popmintchev, D. *et al.* Near-and extended-edge x-ray-absorption fine-structure spectroscopy using ultrafast coherent high-order harmonic supercontinua. *Physical review letters* **120,** 093002 (2018).
10. Dorney, K. M. *et al.* Bright, single helicity, high harmonics driven by mid-infrared bicircular laser fields. *Optics Express* **29,** 38119–38128 (2021).
11. Popmintchev, T. *et al.* Phase matching of high harmonic generation in the soft and hard X-ray regions of the spectrum. *Proceedings of the National Academy of Sciences* **106,** 10516–10521 (2009).
12. Systems, A. F. *Compact ultrafast Ytterbium (1μm) - Active Fiber Systems* https://www.afs-jena.de/products/compact-ultrafast-ytterbium/ [Accessed: (03-12-2023)].

13. Klas, R. *et al. Ultrafast HHG source delivering 13 mW of average power* in *Compact EUV & X-ray Light Sources* (2022), EThe3A–1.

14. Malekmohamadi, S. *et al. 70W, 1MHz, sub-50fs Yb-doped fiber laser system for high harmonic generation* in *The European Conference on Lasers and Electro-Optics* (2023), cj_p_19.

15. Rothhardt, J. *et al. Nanoscale imaging with high photon flux table-top XUV sources* in *2016 IEEE Photonics Conference (IPC)* (2016), 448–449.

16. Dorner-Kirchner, M. *et al.* HHG at the Carbon K-Edge Directly Driven by SRS Red-Shifted Pulses from an Ytterbium Amplifier. *ACS photonics* **10,** 84–91 (2022).

17. Henke, B. L., Gullikson, E. M. & Davis, J. C. X-ray interactions: photoabsorption, scattering, transmission, and reflection at E= 50-30,000 eV, Z= 1-92. *Atomic data and nuclear data tables* **54,** 181–342 (1993).

18. Loetgering, L., Witte, S. & Rothhardt, J. Advances in laboratory-scale ptychography using high harmonic sources. *Optics Express* **30,** 4133–4164 (2022).

19. Tschernajew, M. *et al. High repetition rate high harmonic generation with ultra-high photon flux* in *Laser Applications Conference* (2020), JTh2A–21.

20. Gullikson, E. CXRO x-ray interactions with matter. *Center for X-ray Optics, Berkeley, CA, USA, http://henke. lbl. gov/optical_constants/(accessed May 2, 2019). There is no corresponding record for this reference* (2011).

21. Bayraktar, M., Bastiaens, B., Bruineman, C., Vratzov, B. & Bijkerk, F. Broadband transmission grating spectrometer for measuring the emission spectrum of EUV sources.

22. Instruments, T. P. *Princeton Instruments PIXIS-XO:2KB datasheet* https://www.princetoninstruments.com/wp-content/uploads/2020/04/PIXIS-XO_2KB_datasheet.pdf [Accessed: (03-12-2023)].

23. Roscam Abbing, S. *Control over Extreme-Ultraviolet High-Harmonic Generation from Gases and Solids* English. PhD-Thesis - Research and graduation internal (Vrije Universiteit Amsterdam, Mar. 2023). ISBN: 9789083303277.

24. Wikmark, H. *et al.* Spatiotemporal coupling of attosecond pulses. *Proceedings of the National Academy of Sciences* **116,** 4779–4787 (2019).

25. Quintard, L. *et al.* Optics-less focusing of XUV high-order harmonics. *Science advances* **5** (2019).

26. Tanksalvala, M. *et al.* Nondestructive, high-resolution, chemically specific 3D nanostructure characterization using phase-sensitive EUV imaging reflectometry. *Science Advances* **7,** eabd9667 (2021).

27. Loetgering, L. *et al.* Tailoring spatial entropy in extreme ultraviolet focused beams for multispectral ptychography. *Optica* **8,** 130–138 (2021).

28. Du, M. *et al.* High-resolution wavefront sensing and aberration analysis of multi-spectral extreme ultraviolet beams. *Optica* **10,** 255–263 (2023).

29. Kirz, J. Phase zone plates for x rays and the extreme uv. *JOSA* **64,** 301–309 (1974).

30. XRnanotech. *Fresnel zone plates* https://www.xrnanotech.com/fresnel-zone-plates [Accessed: (03-12-2023)].

31. Gorelick, S., Guzenko, V. A., Vila-Comamala, J. & David, C. Direct e-beam writing of dense and high aspect ratio nanostructures in thick layers of PMMA for electroplating. *Nanotechnology* **21,** 295303 (2010).

32. Michette, A. G. in *Optical Systems for Soft X Rays* 165–215 (Springer, 1986).

33. Baez, A. V. A study in diffraction microscopy with special reference to x-rays. *JOSA* **42,** 756–762 (1952).

34. Sweeney, D. W., Hudyma, R. M., Chapman, H. N. & Shafer, D. *EUV optical design for a 100-nm CD imaging system* in *Emerging Lithographic Technologies II* **3331** (1998), 2–10.

35. Hurwitz, M. & Bowyer, S. *A high resolution spectrometer for EUV/FUV wavelengths* in *Instrumentation in astronomy VI* **627** (1986), 375–378.

36. Scholze, F. *et al. High-accuracy EUV metrology of PTB using synchrotron radiation* in *Metrology, inspection, and process control for microlithography XV* **4344** (2001), 402–413.

37. Miyake, A. *et al. LPP-based reflectometer for characterization of EUV lithography systems* in *Emerging Lithographic Technologies VII* **5037** (2003), 647–655.

38. Huber, M. C. & Tondello, G. Stigmatic performance of an EUV spectrograph with a single toroidal grating. *Applied Optics* **18,** 3948–3953 (1979).

39. Kirkpatrick, P. & Baez, A. V. Formation of Optical Images by X-Rays. *J. Opt. Soc. Am.* **38,** 766–774. https://opg.optica.org/abstract.cfm?URI=josa-38-9-766 (Sept. 1948).

40. Ossiander, M. *et al.* Extreme ultraviolet metalens by vacuum guiding. *Science* **380,** 59–63 (2023).

41. Bilderback, D. H. Review of capillary x-ray optics from the 2nd International Capillary Optics Meeting. *X-Ray Spectrometry: An International Journal* **32,** 195–207 (2003).

42. Erko, A. & Zizak, I. Hard X-ray micro-spectroscopy at Berliner Elektronenspeicherring für Synchrotronstrahlung II. *Spectrochimica Acta Part B: Atomic Spectroscopy* **64,** 833–848 (2009).

43. Attwood, D. & Sakdinawat, A. *X-Rays and Extreme Ultraviolet Radiation: Principles and Applications* 2nd ed. (Cambridge University Press, 2017).

44. Spiller, E. *Soft-x-ray optics* in *OSA Annual Meeting* (1990), TuB1.

45. Instruments, T. P. *Princeton Instruments PI-MTE3 datasheet* https://www.princetoninstruments.com/wp-content/uploads/2020/04/PI-MTE3-Rev-A1-07212021.pdf [Accessed: (03-12-2023)].

46. Van den Born, J. *et al. The MICADO atmospheric dispersion corrector: optomechanical design, expected performance and calibration techniques* in *Ground-based and Airborne Instrumentation for Astronomy IX* **12184** (2022), 927–942.

47. Clark, J. in *Viewing and Imaging the Solar System: A Guide for Amateur Astronomers* 57–80 (Springer New York, New York, NY, 2015). ISBN: 978-1-4614-5179-2. https://doi.org/10.1007/978-1-4614-5179-2_4.

48. Lavenu, L. *et al.* High-power two-cycle ultrafast source based on hybrid nonlinear compression. *Optics express* **27,** 1958–1967 (2019).

49. Vicentini, E. *et al.* Nonlinear pulse compression to 22 fs at 15.6 µJ by an all-solid-state multipass approach. *Opt. Express* **28,** 4541–4549. https://opg.optica.org/oe/abstract.cfm?URI=oe-28-4-4541 (Feb. 2020).

50. Zhang, F., Pelekanidis, A., Du, M., Eikema, K. & Witte, S. *Nonlinear compression of mJ-level pulses via double-pass loose focusing in air* in *The European Conference on Lasers and Electro-Optics* (2023), cf_p_15.

51. Danielson, P. Contamination in vacuum systems, sources and remedies. *R&D Magazine* (2001).

52. Hollenshead, J. & Klebanoff, L. Modeling radiation-induced carbon contamination of extreme ultraviolet optics. *Journal of Vacuum Science Technology B: Microelectronics and Nanometer Structures Processing, Measurement, and Phenomena* **24,** 64–82. ISSN: 1071-1023. eprint: https://pubs.aip.org/avs/jvb/article-pdf/24/1/64/15863905/64_1_online.pdf. https://doi.org/10.1116/1.2140005 (Jan. 2006).

53. Dolgov, A. Plasma assisted cleaning of Extreme UV optics.

54. Klas, R., Kirsche, A., Tschernajew, M., Rothhardt, J. & Limpert, J. Annular beam driven high harmonic generation for high flux coherent XUV and soft X-ray radiation. *Optics Express* **26,** 19318–19327 (2018).

55. Eschen, W. *et al.* High-speed and wide-field nanoscale table-top ptychographic EUV imaging and beam characterization with a sCMOS detector. *Optics Express* **31,** 14212–14224 (2023).

5

REFLECTION-MODE EUV PTYCHOGRAPHY WITH AN AUTOMATIC DIFFERENTIATION BASED FRAMEWORK

Ptychographic extreme ultraviolet (EUV) diffractive imaging has emerged as a promising metrology solution in the semiconductor industry, as it can image wafer samples in reflection geometry at the nanoscale. In this chapter we demonstrate multi-wavelength ptychographic reconstruction with a novel ptychography algorithm based on automatic differentiation. A wafer sample with 20-nm height patterned gold structures on a silicon substrate was illuminated in a reflection geometry with an EUV source implemented in a high harmonic generation beamline. To tackle instabilities of the HHG source, a series of mutually incoherent and independent spatial modes were implemented in the ptychography model. By optimising over 200 million parameters, we demonstrate the algorithm's capacity to accommodate experimental uncertainties and achieve a resolution approaching the diffraction limit in a reflection geometry.

This chapter is a collaborative effort together with Yifeng Shao and Jacob Seifert. I focused on the methodology, experimental measurements, investigation, visualization and writing. Yifeng Shao and Jacob Seifert worked on methodology, algorithm, investigation, visualization, writing and conceptualization. The work presented in this chapter has been published in Light: Science and Applications, "Wavelength-multiplexed Multi-mode EUV Reflection Ptychography based on Automatic-Differentiation"

5.1. INTRODUCTION

In Chapter 2 we covered some fundamentals of lensless imaging and ptychography including some algorithms like PIE and ePIE. The basic goal of these iterative optimisation engines is to find convergence in a solution space by minimizing a loss function utilizing the information redundancy in a data set. However, exploiting the information redundancy and expanding the parameters to be retrieved leads to a drastic growth in model complexity, making it harder to derive the loss function and its various derivatives analytically by hand.

We can use automatic differentiation (AD) to help dealing with these complex physical processes described by our models. AD is a great tool for creating a general framework for ptychography models [1–5] and other computational imaging methods [6, 7] as thanks to AD the gradients in iterative optimization problems do not have to be computed by hand.

In this chapter, we show results from the EUV beamline mentioned before, detailed in Chapter 4, using an HHG source for ptychographic diffractive imaging with a reflection geometry. We show that by using AD and a layered ptychography model, we can retrieve both the sample and the probe in different modes and wavelengths, while handling various uncertainties that come up during the experiment.

5.1.1. UNIVERSAL PTYCHOGRAPHY ALGORITHM BASED ON AUTOMATIC DIFFERENTIATION

Consider the universal case of the ptychography model when the illumination consists of multiple spectral harmonics. Both the field illuminating the sample and the sample itself exhibit moderate spatial partially coherent behaviours, which can be described by multiple spatial modes [8–14]. The probe modes represent a decoherence effect as a consequence of the accumulated instabilities. Sample modes typically describe a stochastic process of sample dynamics [8, 10, 12] which is usually needed when performing ptychography at an atomic scale as for 4D scanning transmission electron microscopy (4DSTEM) where sub-Ångström resolution is possible.

Our generalized ptychography model uses the following expression to estimate the diffraction patterns recorded during the scan:

$$I_k(\boldsymbol{\rho}) = \mathcal{M}(\boldsymbol{\rho}) \left[\sum_{l=1}^{L} \sum_{m=1}^{M} \sum_{n=1}^{N} |\mathcal{D}_{\lambda_l,z} \left[\sigma_k P_{l,m}(\mathbf{r}) O_{l,n}(\mathbf{r}-\mathbf{s}_k) \right] (\boldsymbol{\rho})|^2 + \mathcal{N}(\boldsymbol{\rho}) \right], \tag{5.1}$$

where k denotes the scan index, l is the index of L wavelengths, m and n are the indices of M illumination modes and N sample modes, respectively. $\mathcal{M}(\rho)$ represents the measurement-related effects at the detector, such as masking or clipping values of pixels in the presence of saturation and variation of responsivities of pixels (e.g "dead" pixels which are abnormally high or low in value and are often referred to as "hot" or "cold" pixels). $\mathbf{r}$ and $\boldsymbol{\rho}$ are 2-dimensional vectors representing the sample plane and the camera plane coordinates, respectively. $\mathcal{N}(\boldsymbol{\rho})$ denotes the intensity of a common background signal due to, for example, stray light. $\mathcal{D}_{\lambda,z}$ represents the propagator that depends on

the wavelength λ and propagation distance z. At wavelength λ_l, we denote the mth illumination mode of the probe by $P_{l,m}(\mathbf{r})$ and the nth sample mode of the object by $O_{l,n}(\mathbf{r})$. We further denote the object's scanning position by $\mathbf{s}_k$ and use σ_k as a coefficient to scale the probe power for the kth acquisition. Using the power coefficient to deal with the energy fluctuation of the HHG source, see more in Chapter 6, assuming that the probe shape remains unchanged through the scanning process. The ptychography process and the related experimental setup are shown in Fig. 5.1

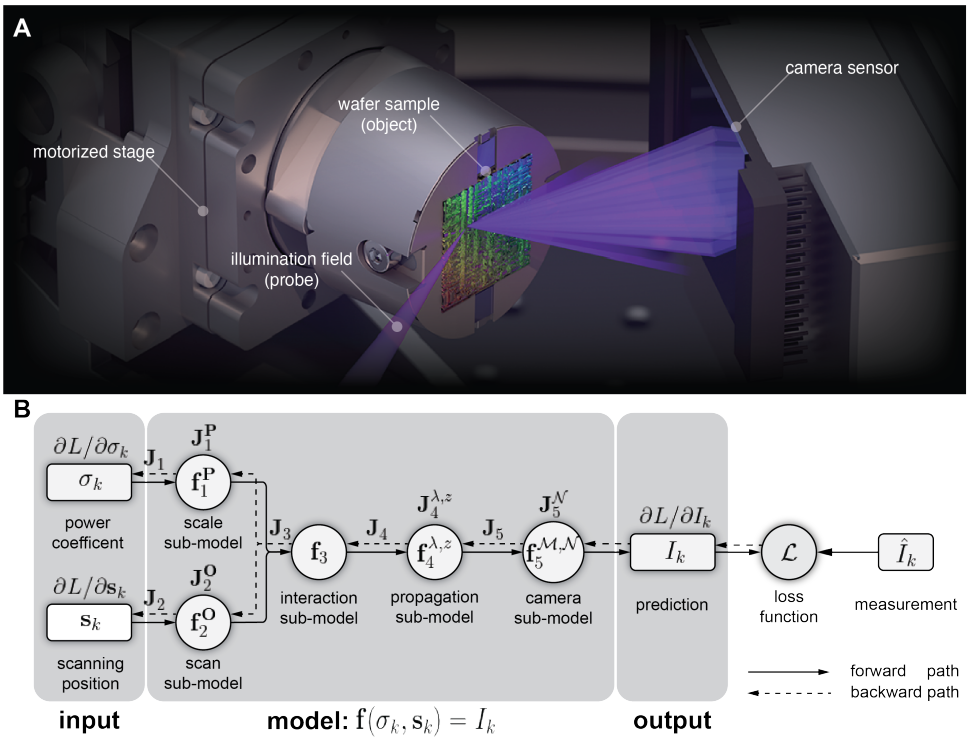

Figure 5.1: The ptychography process and the computational graph for the reconstruction. (**A**): Illustration of the ptychography process and the experimental setup in the reflection geometry. (**B**): The computational graph for ptychography reconstruction. The forward path (solid arrows) predicts the diffraction pattern measured by the camera during the scan and evaluates the loss function. The backward path (dashed arrows) computes the gradients of the loss function with respect to the variables of the sub-models and both inputs of the model in an accumulative manner.

The optimisation requires a loss function to quantify the difference between the predicted and measured diffraction patterns, denoted by I_k and $\hat{I}_k$, respectively. One can define such a loss function $\mathcal{L}(I_k, \hat{I}_k)$ either using the standard mean-squared-error (MSE) as the metric on the modulus of the diffracted field or, if the noise statistics is known, using the maximum-likelihood estimation [15–17].

Computing the gradient of the loss function with respect to each variable requires an analytical expression derived from Eq. 5.1 which is typically done through manual differ-

entiation or symbolic differentiation. This approach can be prone to mistakes in either the derivation process or converting the analytical model into a manually programmed function. On top of that, it can be rather time consuming as this process has to be repeated for any changes or extension to one of the sub-models in the overall model as described by Eq. 5.1.

Using automatic differentiation (AD) as an alternative to gradient computation can circumvent these issues. The crucial step is to represent the complicated model by a series of concatenated simpler functions, each representing a sub-model. With this concept in mind, we can restate Eq. 5.1 to be a function $\mathbf{f}$ with two inputs: σ_k and $\mathbf{s}_k$, and one output: the diffraction pattern I_k, both specified for a particular scan index k. We write this function $\mathbf{f}$ as:

$$I_k = \mathbf{f}(\sigma_k, \mathbf{s}_k) = \mathbf{f}_5^{\mathcal{M},\mathcal{N}}\left(\mathbf{f}_4^{\lambda,z}\left(\mathbf{f}_3\left(\mathbf{f}_1^{\mathbf{P}}(\sigma_k), \mathbf{f}_2^{\mathbf{O}}(\mathbf{s}_k)\right)\right)\right), \tag{5.2}$$

where the superscripts represent the variables that the respective functions depend on. $\mathbf{P}$ and $\mathbf{O}$ are both 4D data arrays, representing the 2D distributions of all spatial modes at all wavelengths. We define that $\mathbf{f}_1^{\mathbf{P}}$ scales the power of probe $\mathbf{P}$ by σ_k and $\mathbf{f}_2^{\mathbf{O}}$ shifts the location of sample $\mathbf{O}$ by $\mathbf{s}_k$. $\mathbf{f}_3$ computes the interaction between the probe and the object, and subsequently, $\mathbf{f}_4^{\lambda,z}$ propagates the resulting field to the detector plane. Finally, $\mathbf{f}_5^{\mathcal{M},\mathcal{N}}$ applies the measurement-related effects to the integrated power of the resulting field on the camera, predicting the diffraction pattern to be measured.

Each function, as shown in Fig. 5.1b, performs certain operations on its variables, taking inputs and yielding outputs. Ptychography is capable of optimising all these variables and inputs of the model by utilising the redundant information resulting from the overlap between the probes at neighbouring scanning positions.

To compute the gradients of the variables in the update scheme for optimisation, AD applies the chain rule to the composite function $\mathbf{f}$ and accumulates the Jacobians (matrices of partial derivatives) of each function in reverse order of evaluating $\mathbf{f}$, following the dashed arrows. Note that the mask function $\mathcal{M}$ is considered to be fixed. The explicit formulas for computing the gradients of the variables are listed below, according to the computational graph in Fig.5.1b:

$$\begin{aligned}
\frac{\partial \mathcal{L}}{\partial \mathcal{N}} &= \mathbf{J}_{\mathcal{L}}\mathbf{J}_5^{\mathcal{N}}, & \frac{\partial \mathcal{L}}{\partial \mathbf{O}} &= \mathbf{J}_{\mathcal{L}}\mathbf{J}_5\mathbf{J}_4\mathbf{J}_3\mathbf{J}_2^{\mathbf{O}}, \\
\frac{\partial \mathcal{L}}{\partial \lambda} &= \mathbf{J}_{\mathcal{L}}\mathbf{J}_5\mathbf{J}_4^{\lambda}, & \frac{\partial \mathcal{L}}{\partial \mathbf{s}_k} &= \mathbf{J}_{\mathcal{L}}\mathbf{J}_5\mathbf{J}_4\mathbf{J}_3\mathbf{J}_2, \\
\frac{\partial \mathcal{L}}{\partial z} &= \mathbf{J}_{\mathcal{L}}\mathbf{J}_5\mathbf{J}_4^{z}, & \frac{\partial \mathcal{L}}{\partial \mathbf{P}} &= \mathbf{J}_{\mathcal{L}}\mathbf{J}_5\mathbf{J}_4\mathbf{J}_3\mathbf{J}_1^{\mathbf{P}}, \\
& & \frac{\partial \mathcal{L}}{\partial \sigma_k} &= \mathbf{J}_{\mathcal{L}}\mathbf{J}_5\mathbf{J}_4\mathbf{J}_3\mathbf{J}_1,
\end{aligned} \tag{5.3}$$

where $\mathbf{J}_{\mathcal{L}}$ is the Jacobian of the loss function with respect to the kth diffraction pattern, $\mathbf{J}_i$ is the Jacobian of $\mathbf{f}_i$, where $i = 1,2,3,4,5$, consisting of the partial derivatives of its output with respect to its input, and $\mathbf{J}_i^{\boldsymbol{\theta}_i}$ denotes the Jacobian for the specific variable

$\boldsymbol{\theta}_i$ in $\mathbf{f}_i$. It is worth noting that AD is capable of avoiding the repetitive evaluations of common Jacobians shared by the explicit formulas in Eq. 5.3. In contrast, conventional approaches based on Eq. 5.1 can only accomplish this through human efforts, achieving in the best scenario an efficiency equivalent, not superior, to that of AD [18, 19].

The modularity of AD offers us maximum freedom in designing the model described by Eq. 5.2, allowing us to switch between different functions in each sub-model while maintaining the same input-output. This feature enables the implementation of various propagators in the propagation sub-model to handle diffraction in various ranges and provides options to customise further the numerical approach for computing each propagation. As a result, we can compute the propagator using either the chirp z-transform (CZT) algorithm [20–22], or using the conventional fast Fourier transform (FFT) algorithm.

AD allows for the decomposition of advanced functions in a model in more elementary functions, with the chain rule applied recursively from advanced to elementary functions when computing the gradient. The only requirement is that every function in this chain must be at least piecewise differentiable, ensuring that the final composite function remains differentiable.

With the gradient computed by AD, the optimisation routine of our algorithm updates the variables with a constant step size iteratively until the loss function reaches a minimum. To prevent oscillations of the loss function in the vicinity of the minimum, we decay the step size exponentially at a constant rate. Due to the differences in physical interpretations and value scales between the variables (often of different dimensions or even dimensionless), each variable may require a different step size.

In addition, we also introduce various regularisations to the loss function to incorporate prior knowledge of the variables, such as the probe and the object, into the optimisation process. For example, the probe support constraint can help centre the probe at the origin, thus avoiding translation ambiguity. The L1 norm and total variation (TV) regularisation can enhance contrast and suppress noise, respectively. To guarantee the orthogonality of the spatial modes, our algorithm uses the mixed mode procedure proposed in [23]. Integrating various regularisations into the optimisation using AD is convenient and straightforward, which only implies extra additive terms, differentiable with respect to the relevant variables, in the loss function.

The algorithm to achieve the results in this work is implemented in a modular package, called *PtychoFlow*. The package is developed in a Python environment with its core functionalities, including the ptychography model and the optimisation loop implemented in Tensorflow, a mainstream open-source machine learning platform. Tensorflow provides the AD functionality and various advance optimisers like the Adam optimiser [24] and GPU acceleration, which guarantees that the optimisation can be completed in a reasonable time so that tuning the optimisation hyperparameters (learning rates, support functions etc.), becomes possible. A utility library of the necessary mathematical functions had to be developed using the Tensorflow AD compatible functions, with which we further build the sub-models. Finally, by concatenating these sub-models together we end up with the final generalized ptychography model.

5.1.2. EXPERIMENTAL SETUP

A ptychography dataset, consisting of 225 diffraction patterns, has been acquired by utilizing the previously described EUV beamline (see Chapter 4). For completeness we go through the setup again. The compact HHG source is pumped by a Ytterbium-doped fiber laser (Active Fiber System UFFL 100) with a centre wavelength at 1030 nm. The pump laser emitted 167 µJ pulses with a pulse length of 300 fs, achieving an average power of 100 W at a repetition rate of 600 kHz. These pulses are further compressed to a pulse length of 28 fs by a Krypton-filled hollow core fiber (HCF) and a set of chirped mirrors. Following compression, the pulsed infrared (IR) beam remains with 114 µJ pulse energy and 68 W average power.

The IR pump laser is focused into a 10-bar pressurised Argon gas jet with a focal spot size of 25.6 µm, placed between a 300 µm sized gas nozzle and a gas catcher as illustrated by Fig. 5.2a. This enables the generation of higher harmonics up to the soft X-ray regime, with the strongest harmonic in the EUV range obtained at 68 eV photon energy, or 18 nm wavelength, with a photon flux of $2 \cdot 10^{11}$ photons per second at the gas jet within 1% of the bandwidth as reported in previous work [25]. By switching to Neon gas, our HHG source is capable of generating EUV radiation centred at 13.5 nm.

Due to the significant power disparity between the generated weak higher harmonics and the much stronger IR pump laser, several measures were implemented to separate the two. Firstly, an annular dichroic mirror with an aperture of 2 mm in the center rejects approximately half of the IR power by utilising the larger divergence of the IR beam relative to that of the higher harmonics. Secondly, a pair of grazing incidence plates (GIP), positioned at the Brewster angle for the IR beam, further attenuate the IR beam while still reflecting the higher harmonics with a total efficiency of 54%. Finally, a pair of 200 nm thick aluminium freestanding foils, which acts as a long-pass filter (in the EUV regime) with a transmission cut-off of 73 eV (equivalent to 17 nm) for the higher harmonics, blocks the remaining IR beam.

In order to calibrate the spectrum of the broadband EUV beam, a flip mirror is inserted into the beamline to redirect the beam towards a spectrometer before selecting a single harmonic for illumination. The spectrometer's working principle is explained in detail in [26]. A portion of the calibrated spectrum, ranging from approximately 17 nm to 19.5 nm, is presented in Fig. 5.2b.

The selection of a single harmonic is achieved using spectral filtering via a pair of consecutive multi-layer mirrors (MLMs) arranged in a periscope-like configuration. These mirrors are positioned parallel at a 45-degree angle with respect to the optical axis and coated with alternating layers of zirconium (Zr) and aluminium (Al). The spectral filter exhibits a reflectivity peak at the center wavelength of 18 nm with a combined peak reflectivity of 21% and a full width at half maximum (FWHM) of 0.6 nm. The white solid curve in Fig. 5.2b illustrates the reflection spectrum of the Zr-Al mirror pair.

The selected single harmonic incident at 10 degrees grazing angle relative to the surface on a Ruthenium-coated ellipsoidal mirror was focused onto the sample, forming a probe of 33 µm by 34 µm in the focal region. The size of the probe is confirmed through a knife-edge measurement in the plane perpendicular to the probe. However, due to the tilt of

the sample for 20 degrees grazing incidence, the probe is elongated in the tilt direction by a factor of three.

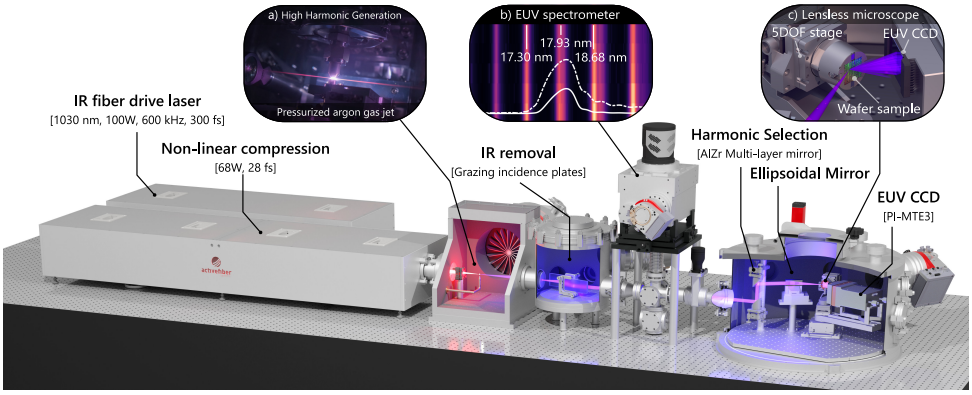

Figure 5.2: The same setup as shown before in Chapter 4 has been used to illuminate the sample. To re-iterate, a single harmonic is selected with spectral filtering using a pair of Al-Zr mirrors, whose spectrum is depicted by the white dashed (one mirror) and solid (two mirrors) curves in inset b). The illumination beam is focused onto a patterned sample by an ellipsoidal mirror, and the resulting diffraction pattern is captured by a CCD camera sensitive to EUV photons for analysis.

In the experiment, the sample is illuminated with an EUV beam focused at an angle of incidence of 70 degrees relative to the sample's surface normal. We scan the illumination beam over a patterned sample consisting of 20-nm high gold-titanium structures deposited onto a silicon substrate. We acquire intensity measurements of the diffraction patterns at 225 scanning positions on a randomly perturbed regular grid. As we illuminate at grazing incidence angle, the probe is severely elongated along the direction of incidence with a size of approximately 30-by-100 µm, resulting in an average scanning interval of 10 µm along the elongated direction of the probe and 3 µm along the other direction.

In reflection geometry, we must correct the distortion of the diffraction pattern due to sample tilt with respect to the optical axis, see Section 2.6. The tilt correction assumes that the camera is placed perpendicular to the direction of the specular reflection and requires information about both the propagation distance (88 mm measured from the sample to the camera) and the tilt angle (equal to the angle of incidence). Prior to the tilt correction, we subtract the noisy camera background, measured in the absence of EUV illumination, and align the specularly reflected zeroth order with the origin of the camera coordinate at the centre of the FOV.

The EUV camera has 2048-by-2048 pixels with 15-by-15 µm pixel size. Through the tilt correction, each diffraction pattern is interpolated non-uniformly onto a sampling grid that has 2048-by-3038 pixels with 15-by-5 µm pixel size. This results in a reduced FOV on the camera and, accordingly, a degraded resolution in the sample, both along the sample tilt direction. The sampling along the other direction remains unchanged. For EUV illumination at 18 nm wavelength, we achieve a sample resolution of 50-by-100 nm with a detection numerical aperture (NA) of 0.170-by-0.086.

The tilt correction also generates a binary mask to separate the pixels inside and outside the reduced FOV. We set the higher and lower threshold of the pixel values to be 2^{16} – 1 and 4, respectively, to discard the saturated and noise-corrupted pixels. The default initial value for the common background in all diffraction patterns to be reconstructed is a uniform value of one. We use a constant value of one as the initial value of the power coefficient at each scanning position.

In the proof-of-principle experiment, we incorporate two harmonics of the HHG beam in forming the diffraction pattern. A slight tilt between the pair of wavelength-selective periscope mirrors induces a slight shift of the filtering window in the spectral domain. As none of these two harmonics is aligned with the peak of the narrow-band filtering window, the beam intensity decreases, increasing the acquisition time from a few hundred milliseconds to tens of seconds per diffraction pattern. The full scan of 225 positions was completed in 45 minutes, including 1 additional second per position to stabilise the motion stage and another 1 second to read out the image at a rate of 4 MHz using a single read-out port from the EUV camera.

5.2. RESULTS

5.2.1. BENCHMARKING AGAINST STATE-OF-THE-ART OPEN-SOURCE PTYCHOGRAPHY ALGORITHM

We validate the benefit of the AD framework by conducting an objective performance comparison between the algorithm, named PtychoFlow, and other ptychography frameworks. Although several open-source code repositories like PtyPy [27], PtychoShelves [28], and PtyLab [29] have been published, none offer the joint optimisation of an equivalent set of parameters discussed in this work. Among these algorithms, PtyLab is the most recent and, to the best of our knowledge, has implemented the most extensive list of features. It resembles important features such as the reconstruction of both multiple spectral harmonics and spatial modes, GPU acceleration, and momentum optimisers. However, it does not support switching on optimising correction features simultaneously. Instead, it alternates between updating different parameters in different iterations. We choose to compare our dataset's reconstruction in both PtychoFlow and PtyLab. We focus on objective goals such as execution time and memory usage. In contrast, identifying the suitable initialisations and hyperparameters for optimisation is subjective and will therefore not be pursued.

In Fig. 5.3a, we compare the execution time per iteration across various scenarios using identical computational hardware. In the default setting of updating only the pixel values in the object and probe, PtyLab uses the mPIE engine [30] and outperforms PtychoFlow. It is worthwhile noting that the speed difference may be attributed to the different GPU acceleration packages used: CuPy [31] by PtyLab and TensorFlow by our algorithm, although both operate on the same Nvidia's CUDA platform. Additionally, PtyLab employs a two-step propagator for wavelength-multiplexed reconstructions [32], while our propagator is based on the chirp z-transform (CZT) or the conventional fast Fourier transform (FFT) algorithm.

In subsequent comparisons on scanning position and propagation distance correction,

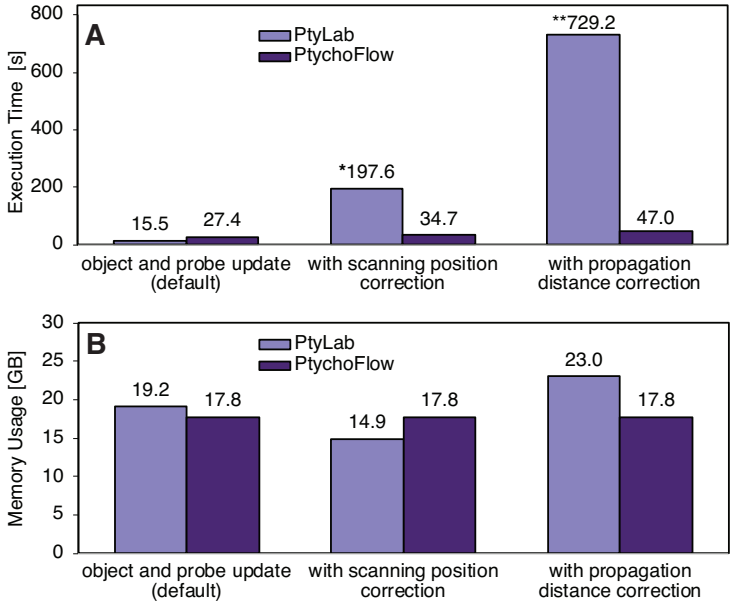

Figure 5.3: Performance comparison in execution time (**A**) and memory usage (**B**). The comparison is conducted by reconstructing the experiment dataset with two wavelengths, and three illumination modes and one sample mode per wavelength. The numbers in the figures are averaged over five runs on a Nvidia RTX A6000 GPU. * The number is obtained for the case of a single wavelength since PtyLab does not support scanning position correction in multiple wavelength reconstruction. ** The number is adjusted since PtyLab only corrects the propagation distance per epoch instead of per batch (usually set to 1, meaning one batch equals one frame). The adjustment calculates the execution time for one correction and scales it by the number of batches to match that in PtychoFlow.

we use the pcPIE [33] and zPIE [34] engines in PtyLab. Here, the benefit of AD becomes apparent, as indicated by the drastic speed advantage. Like other conventional ptychography algorithms [35–37], PtyLab updates the additional variables via a secondary optimisation loop alongside the primary iterative routine to reconstruct the probe and the object while updating all parameters in the AD framework is a unified process.

When comparing the usage of GPU's Video Random-Access Memory (VRAM), a critical resource for ptychographic reconstructions, we found in Fig. 5.3b that, thanks to AD, incorporating additional parameters does not impact the memory usage in PtychoFlow, while PtyLab tends to use extra VRAM for the correction. The overall performance comparison confirms that the computational complexity scales much more consistently and favourably for PtychoFlow than for conventional algorithms as used in PtyLab.

5.2.2. WAVELENGTH-MULTIPLEXED DIFFRACTIVE IMAGING

The reconstruction always starts with elliptical apertures as the initial guesses of the probe. The elliptical aperture's centre, size (long and short axes), and rotation angle can be configured individually for each wavelength. The initial object is a uniform value of

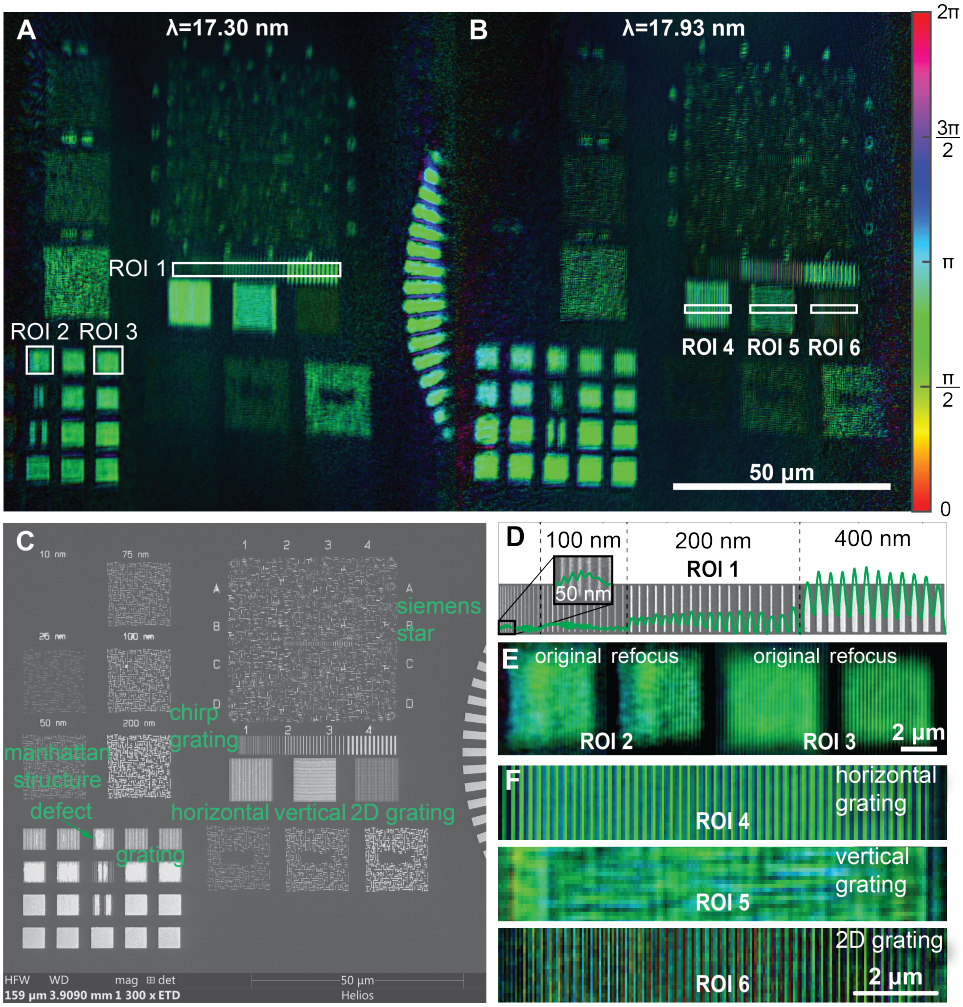

Figure 5.4: Ptychographic reconstructions of nanostructures on the wafer sample at wavelength 17.30 nm and 17.93 nm in the top row. The reconstructed objects show shifted field-of-views as the probes at different wavelengths illuminate different areas on the sample. The amplitude and the phase of the complex-valued object are presented by the colour and the brightness of the image, respectively. (**C**): SEM image of the wafer sample with various types of structures and manufacturing defects for comparison. (**D**): Profile of the chirped grating (green curve) in ROI 1 consisting of 200 nm, 100 nm, and 50 nm lines with varying spacing on top a SEM image of the chirped grating. Inset: the finest part of the chirped grating with 150 nm pitch and 50 nm linewidth. (**E**): Gratings in squared areas ROI 2 (with a manufacturing defect) and ROI 3, before (left) and after (right) refocusing for enhancing contrast. (**F**): Zoom-in of the reconstructed structures in ROI 4-6. Due to the non-uniform sample resolution in the reflection geometry, only the horizontal grating and the horizontal part of the 2D grating can be resolved.

one, representing a flat, unpatterned wafer sample.

The wavelength-dependent behaviour of the sample in response to the illumination field

necessitates the assumption of a dispersive sample in the reconstruction, resulting in a sample function for each wavelength. Eventually, we reconstruct six illumination modes and one sample mode per wavelength to tackle the limited source spatial coherence and inherent instabilities. As each illumination mode and sample mode contains 12 million and 27 million parameters, we optimise over 200 million parameters with our universal ptychography algorithm based on the AD framework, referred to as *PtychoFlow*. The optimization starts with updating the probe and object alongside propagation distance correction for 100 iterations, in which the support constraint and the L1 regularization were applied to the probe, and a mixture of L1 and TV regularizations was applied to the object. In the subsequent 150 iterations, we started to float the scanning positions in the optimization and fine-tuned the probe and object with modest regularizations.

The reconstructed objects presented in Fig. 5.4a and Fig. 5.4b, corresponding to sample modes at wavelengths 17.30 nm and 17.93 nm, respectively, exhibit shifted field-of-views on the wafer sample. The cross-correlation analysis of these objects indicates a shift of about 30 µm, mainly in the horizontal direction, perpendicular to the direction of sample tilt in the reflection geometry and the elongation direction of the probes. This shift suggests that the probes at the different wavelengths illuminate different areas of the sample. A similar spatial dispersion effect of the HHG beam has been reported in [38]. For a distance of 160 mm between the focusing optics and the sample, we found that the propagation directions of the two harmonics deviate from each other only by a negligible angle of 0.03 mrad at the pupil. Additionally, noticeable non-uniform deformation in each reconstructed object can be observed, which can most likely be attributed to the remaining uncertainties in the tilt plane correction procedure. However, the cause of the difference in the deformations at different wavelengths is a subject of future investigation.

In Fig. 5.4d, the chirped grating profile in region-of-interest (ROI) 1 is displayed. The profile is obtained by summing the intensity (absolute squared of the amplitude) of the reconstructed object along the direction parallel to the grating lines. From left to right, the grating consists of equally spaced 400 nm lines (800 nm pitch), 200 nm lines with decreasing pitches from 800 nm to 600 nm, 100 nm lines with decreasing pitches from 600 nm to 350 nm, and 50 nm lines with decreasing pitches 350 nm to 150 nm. The inset plot on the leftmost side shows the finest part of the grating, in which the peaks align well with the locations of the 50 nm lines in the background SEM image. The obtained resolution of 50 nm is the diffraction limit with an NA of 0.17 at 18 nm wavelength.

To improve the contrast of the reconstructed object, we employ a refocusing approach by propagating the entire object to a series of planes between -25 µm and +25 µm with an interval of 200 nm using the angular spectrum method. Specifically, we focus on refining the gratings in ROI 2 and ROI 3, both with 200 nm pitch and 50% filling ratio. By extracting the strength of the spatial frequency component at 5 μm^{-1} from the Fourier transform of the grating profile in each plane, we can obtain a curve as a function of the z location with fast oscillations due to the Talbot effect and a slowly varying envelope due to defocusing of non-periodic features in the periodic grating. By locating the maximum of this curve, we can determine a defocus distance of -3.51 µm and -3.31 µm for ROI 2 and ROI 3, respectively.

For ptychography in the reflection geometry, the resolution of the reconstructed object is reduced in the direction of the sample tilt and the elongation direction of the probe. This is illustrated in Fig. 5.4f by the reconstructed object with a non-symmetric resolution of 50 nm in the horizontal direction and 100 nm in the vertical direction. As a result, the horizontal grating (ROI 4) exhibits distinct periodic structures with a pitch of 200 nm and a linewidth of 100 nm, while the vertical grating (ROI 5) with identical pitch and linewidth appears almost uniform but does not resolve the lines. In the 2-dimensional grating (ROI 6), the horizontal components are resolved as a 1-dimensional grating, while the vertical components are effectively unresolved.

5.2.3. 3D STRUCTURE INFORMATION CHARACTERISATION

In Fig. 5.5a, the contours indicate the regions where specific percentages of the total number of photons illuminate the sample during the scanning process. Consider the part of the Siemens star reconstructed in the full field-of-view located in between the 75% and 95% contours. This ring area is illuminated by only 20% of the total amount of photons, and only a small fraction of this amount of photons is scattered by the structures, contributing to the formation of the diffraction pattern, while almost no photon is scattered by the substrate.

The reconstruction of the complex-valued object enables the segmentation of the sample into the gold structures and the silicon substrate based on the pixels' complex values and spatial locations. In Fig. 5.5b, we present the amplitude-phase histogram of the pixels in the reconstructed Siemens star, where two clusters of pixels can be identified: one with higher amplitudes representing the structures and the other with lower amplitudes representing the substrate. For illumination at 17.30 nm wavelength with a 70-degree incidence angle, the reflectivities of the gold and the silicon are 0.37 and 0.0077, respectively [39]. The structures reveal small phase variations, represented by an almost uniform green colour in the reconstructed Siemens star. The substrate, however, exhibits a large phase variation due to the low amplitude. This emphasises the need for caution when applying L1 and TV regularisations to the amplitude as both tend to drive the low amplitude further to zero and thus can introduce extra uncertainties when determining the structure information.

The phase difference between the structures and the substrate can be computed by averaging the phase over all pixels in each cluster. This phase difference arises from two sources: (1) the phase difference induced by the reflection at different interfaces through the Fresnel relations, and (2) the phase difference accumulated through propagation over different distances as caused by the surface topology..

With prior knowledge of the respective compositions of gold and silicon in the structures and substrate, the first part can be obtained by computing the phase difference between the Fresnel coefficients at the surfaces. We emphasise that this approach is only valid when no standing wave is formed in the structures due to sufficient absorption and the scattering in the lateral plane is negligible (e.g. when the feature size of interest is much larger than the wavelength). Otherwise, a Maxwell solver is required to compute the light-structure interaction.

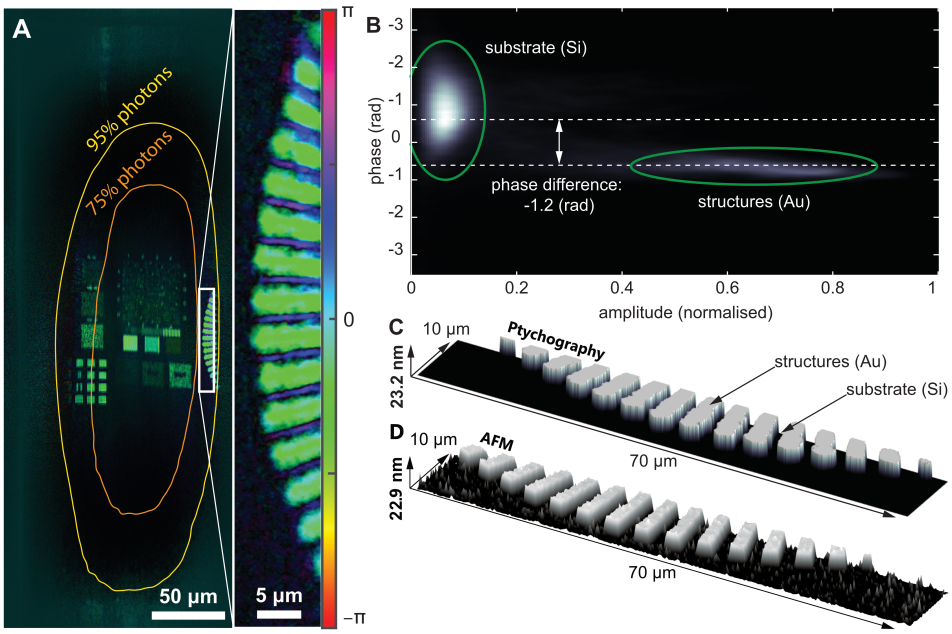

Figure 5.5: 3D structure information characterisation. (**A**): The entire field-of-view of the reconstructed complex-valued object. The contours in orange and yellow mark the areas illuminated with 75% and 95% of the total photons during the scanning process, respectively. Inset: the reconstructed Siemens star with 90 spokes and a radius of 60 µm. (**B**): Distribution of pixel values in amplitude (normalised) and phase coordinates. The green circles indicate the clusters of pixels for the Si substrate and the Au structures, respectively. (**C**): 3D representation of the reconstructed Siemens star. The height is computed using the average phase difference determined in (B), the incident angle, the wavelength, with prior knowledge of the materials and their n and k values, resulting in an average height of 23.2 nm. (**D**): A representative height of 22.9 nm has been retrieved with an Atomic Force Microscope (AFM) in the same ROI.

The second part, which is directly proportional to the height of the structures with respect to the substrate, can be obtained by subtracting the first part from the reconstructed phase difference. In this work, the thus estimated height of 23.6 ± 0.6 nm agrees well with both the 20 nm nominal design value and the height retrieved from the AFM measurement of 22.8 ± 1.4 nm. Fig. 5.5c shows a 3D representation of the segmented Siemens star with the values of the pixels belonging to the two clusters, the substrate and the structures, set to zero and actual height, respectively.

5.2.4. EUV FOCUSING OPTICS CHARACTERISATION

Fig. 5.6a and Fig. 5.6b show the sum of all diffraction patterns and the common background, respectively. Under the first Born approximation with the regular multiplicative assumption made in ptychography, the far-field wavefront that generates the diffraction pattern as its modulus squared, can be interpreted as the Fourier transform of the object convolved with the field distribution in the pupil when using a focused beam to illuminate the sample. Because of this convolution relation, both the zeroth diffraction

order, which is in the shape of the ellipsoidal focusing mirror, and higher diffraction orders are visible in Fig. 5.6a. In the presence of specular reflection by the sample, the Fourier transform of this uniform signal is a delta function in the far-field. As a result of convolving with the delta function, the common background on the camera is almost identical to the pupil plane field distribution despite the minor contributions by other effects like stray light due to spurious reflections in the beamline. Therefore, the common background can be used to characterise the focusing optics. Fig. 5.6 (B) clearly reveals grooves of grinding tool marks and defects on the surface of the ellipsoidal focusing mirror indicating a rather poor quality of the optical surface.

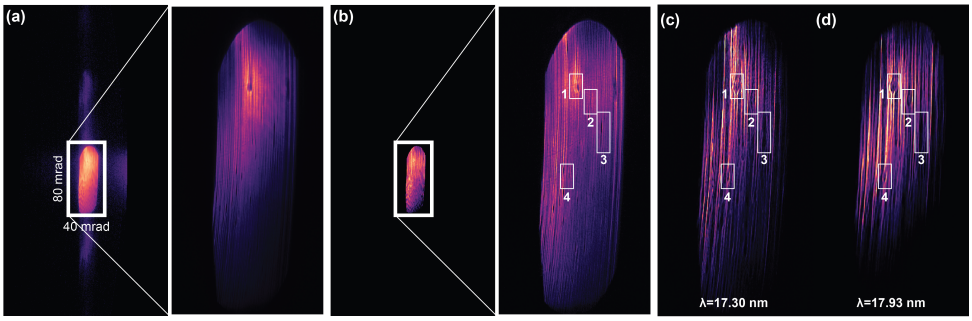

Figure 5.6: EUV focusing optics characterisation. (**A**): Summed intensity distributions of the diffraction patterns in logarithmic scale with zeroth order in the shape of the ellipsoidal focusing mirror and higher orders cropped in the horizontal direction due to the sample tilt in reflection geometry. Inset: zoom-in of the zeroth order in linear scale. (**B**): Reconstructed common background intensity in logarithmic with a clearly distinct ellipsoidal shape representing the pupil of the illumination system. Inset: zoom-in of pupil in linear scale. (**C** and **D**): Reconstructed pupil function of the illumination probe at wavelengths 17.30 nm (C) and 17.93 nm (D). The rectangular ROI 1-4 show the locations of the defects on the EUV focusing mirror.

The pupil function can also be obtained by applying the inverse Fourier transform to the reconstructed probe. By comparing the common background with the two pupil functions at two wavelengths shown in Fig. 5.6c and Fig. 5.6d, we can confirm the presence of the grinding tool marks and the defects on the focusing optics. ROI 1-4 reveal that the locations of the defects are well aligned in both the pupil functions and the common background, yet with distinguishable visual effects. For instance, those defects in ROI 2 & 4 are more discernible in the pupil functions than in the common background.

5.3. DISCUSSIONS AND CONCLUSIONS

The introduced universal ptychography algorithm based on the automatic-differentiation (AD) framework has been demonstrated to be a powerful tool for EUV diffractive imaging that is crucial for future semiconductor metrology applications. It covers both transmission and reflection (through tilt correction) configurations and can deal with source instabilities and numerous sources of experimental uncertainties.

The AD framework allows us to optimise the high-dimensional arrays of the probe and the object, along with other variables involved in relevant physical processes. As long as a physical process can be mathematically described using differentiable operations,

it can be incorporated into the universal ptychography model, and its variables can be retrieved using AD and gradient-descent type optimisation. We demonstrate through a comparison with a state-of-art ptychography algorithm that the AD approach is superior in both execution time and memory usage. It is worth noting that manual approaches can also achieve equivalent performance if and only if the derivation through all physical processes is handled properly and the implementation avoids repetitive computations. Combined with the modular design, our versatile and expandable ptychography algorithm is capable of handling diverse challenges and is future-proof to meet the requirements of next-generation metrology applications.

Implementing the algorithm on mainstream machine learning platforms like TensorFlow provides GPU acceleration as an additional benefit. However, the limited memory of the GPU also imposes a constraint on the model's size. In ptychography, computing the Fourier transform for field propagation is the most time-consuming operation. Because ptychography computes one field propagation per spatial mode per spectral harmonic, computation time increases rapidly as the number of spectral harmonics and spatial modes increases. This issue can be mitigated by distributed optimisation on GPU clusters.

To achieve the results shown in this paper, we optimise a ptychography model containing variables with a total number of 201 million parameters to retrieve information from a dataset containing frames with a total number of 1.1 billion pixels. The 1:5 ratio between the numbers of the parameters and the pixels suggests there is still a sufficient abundance of information available in the data.

Among these parameters, the illumination modes, required to deal with the lack of sufficient spatial coherence of the HHG EUV probe, can be decreased by increasing the source stability. This reduces both the computation time per iteration and the number of iterations. Besides, by pre-calibrating the probe and other experimental parameters, leaving the object as the only variable, one can significantly reduce the number of parameters and hence further achieve fast reconstructions.

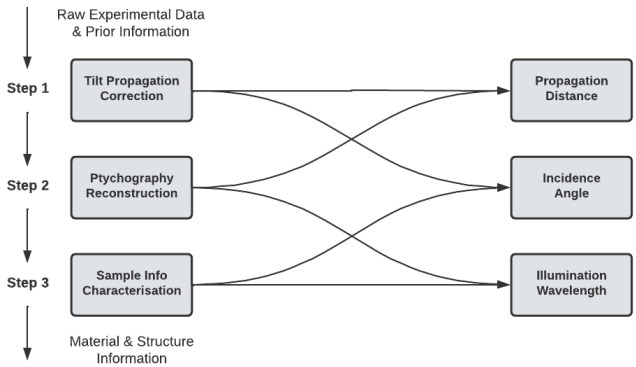

Figure 5.7: Intertwined relations between the main steps for quantitative imaging and the relevant variables.

Finally, achieving unique and unambiguous results is crucial for quantitative imaging approaches with metrology applications at the industrial level. Fig. 5.7 depicts the intertwined relations between the three main steps for quantitative imaging and the three relevant variables (propagation distance, incidence angle and illumination wavelength). This necessitates incorporating the tilted propagation into the model alongside the ptychography process. For future research, calibrating these three variables through optimisation, along with the reconstruction of the probe and the object, is critical to secure the unique and unambiguous characterisation of the sample information.

In conclusion, our AD-based ptychography algorithm successfully reconstructs images of samples using data acquired with multiple harmonic frequencies and limited spatial coherence by considering multiple illumination and sample modes per wavelength. AD is essential for managing complex, large-scale ptychography models and allows the algorithm to account for various uncertainties arising during the experiments. The wavelength multiplexed reconstruction using HHG EUV illumination in reflection geometry demonstrates the possibility of determining both material and structure information for wafer samples. These findings reveal the capabilities of our ptychography algorithm to release the full potential of advanced HHG sources in view of EUV diffractive imaging and establish ptychography as an imaging metrology approach with the potential for high-resolution and high-throughput applications.

BIBLIOGRAPHY

1. Jurling, A. S. & Fienup, J. R. Applications of algorithmic differentiation to phase retrieval algorithms. *JOSA A* **31,** 1348–1359 (2014).
2. Kandel, S. *et al.* Using automatic differentiation as a general framework for ptychographic reconstruction. *Optics express* **27,** 18653–18672 (2019).
3. Seifert, J., Bouchet, D., Loetgering, L. & Mosk, A. P. Efficient and flexible approach to ptychography using an optimization framework based on automatic differentiation. *OSA Continuum* **4,** 121–128 (2021).
4. Kharitonov, K. *et al.* Flexible ptychography platform to expand the potential of imaging at free electron lasers. *Optics express* **29,** 22345–22365 (2021).
5. Maathuis, K., Seifert, J. & Mosk, A. P. Sensor fusion in ptychography. *Optics Continuum* **1,** 1909–1917 (2022).
6. Du, M., Nashed, Y. S., Kandel, S., Gürsoy, D. & Jacobsen, C. Three dimensions, two microscopes, one code: Automatic differentiation for x-ray nanotomography beyond the depth of focus limit. *Science advances* **6,** eaay3700 (2020).
7. Du, M. *et al.* Adorym: A multi-platform generic X-ray image reconstruction framework based on automatic differentiation. *Optics express* **29,** 10000–10035 (2021).
8. Wolf, E. New theory of partial coherence in the space–frequency domain. Part I: spectra and cross spectra of steady-state sources. *JOSA* **72,** 343–351 (1982).
9. Goodman, J. W. *Statistical Optics. 2nd edn.* (New York: Wiley, 2015).
10. Lahiri, A. in *Basic Optics* (ed Lahiri, A.) 605–696 (Elsevier, Amsterdam). ISBN: 978-0-12-805357-7.
11. Whitehead, L. *et al.* Diffractive imaging using partially coherent x rays. *Physical review letters* **103,** 243902 (2009).
12. Thibault, P. & Menzel, A. Reconstructing state mixtures from diffraction measurements. *Nature* **494,** 68–71 (2013).
13. Clark, J. N., Huang, X., Harder, R. J. & Robinson, I. K. Dynamic imaging using ptychography. *Physical review letters* **112,** 113901 (2014).
14. Chen, Z. *et al.* Mixed-state electron ptychography enables sub-angstrom resolution imaging with picometer precision at low dose. *Nature communications* **11,** 2994 (2020).
15. Thibault, P. & Guizar-Sicairos, M. Maximum-likelihood refinement for coherent diffractive imaging. *New Journal of Physics* **14,** 063004 (2012).
16. Godard, P., Allain, M., Chamard, V. & Rodenburg, J. Noise models for low counting rate coherent diffraction imaging. *Optics express* **20,** 25914–25934 (2012).

17. Odstrčil, M., Menzel, A. & Guizar-Sicairos, M. Iterative least-squares solver for generalized maximum-likelihood ptychography. *Optics express* **26,** 3108–3123 (2018).

18. Griewank, A. & Walther, A. *Evaluating derivatives: principles and techniques of algorithmic differentiation* (SIAM, 2008).

19. Kakade, S. M. & Lee, J. D. Provably correct automatic sub-differentiation for qualified programs. *Advances in neural information processing systems* **31** (2018).

20. Rabiner, L., Schafer, R. W. & Rader, C. The chirp z-transform algorithm. *IEEE transactions on audio and electroacoustics* **17,** 86–92 (1969).

21. Hu, Y. *et al.* Efficient full-path optical calculation of scalar and vector diffraction using the Bluestein method. *Light: Science & Applications* **9,** 1–11 (2020).

22. Shao, Y. & Urbach, H. P. Comment on "Efficient full-path optical calculation of scalar and vector diffraction using the Bluestein method". *Light: Science & Applications* **10,** 1–1 (2021).

23. Li, P., Edo, T., Batey, D., Rodenburg, J. & Maiden, A. Breaking ambiguities in mixed state ptychography. *Optics express* **24,** 9038–9052 (2016).

24. Kingma, D. P. & Ba, J. Adam: A method for stochastic optimization. *arXiv preprint arXiv:1412.6980* (2014).

25. Tschernajew, M. *et al. High repetition rate high harmonic generation with ultrahigh photon flux* in *Laser Applications Conference* (2020), JTh2A–21.

26. Goh, S. *et al.* Fabrication and characterization of free-standing, high-line-density transmission gratings for the vacuum UV to soft X-ray range. *Optics express* **23,** 4421–4434 (2015).

27. Enders, B. & Thibault, P. A computational framework for ptychographic reconstructions. *Proceedings of the Royal Society A: Mathematical, Physical and Engineering Sciences* **472,** 20160640 (2016).

28. Wakonig, K. *et al.* PtychoShelves, a versatile high-level framework for high-performance analysis of ptychographic data. *Journal of Applied Crystallography* **53,** 574–586 (2020).

29. Loetgering, L. *et al.* PtyLab. m/py/jl: a cross-platform, open-source inverse modeling toolbox for conventional and Fourier ptychography. *Optics Express* **31,** 13763–13797 (2023).

30. Maiden, A., Johnson, D. & Li, P. Further improvements to the ptychographical iterative engine. *Optica* **4,** 736–745 (2017).

31. Okuta, R., Unno, Y., Nishino, D., Hido, S. & Loomis, C. *CuPy: A NumPy-Compatible Library for NVIDIA GPU Calculations* in (), Proceedings of Workshop on Machine Learning Systems (LearningSys) in The Thirty–first Annual Conference on Neural Information Processing Systems. Long Beach, CA, USA, 2017.

32. Loetgering, L. *et al.* Tailoring spatial entropy in extreme ultraviolet focused beams for multispectral ptychography. *Optica* **8,** 130–138 (2021).

33. Maiden, A., Humphry, M., Sarahan, M., Kraus, B. & Rodenburg, J. An annealing algorithm to correct positioning errors in ptychography. *Ultramicroscopy* **120,** 64–72 (2012).

34. Loetgering, L., Du, M., Eikema, K. S. & Witte, S. zPIE: an autofocusing algorithm for ptychography. *Optics letters* **45,** 2030–2033 (2020).

35. Zhang, F. *et al.* Translation position determination in ptychographic coherent diffraction imaging. *Optics express* **21,** 13592–13606 (2013).

36. Dwivedi, P., Konijnenberg, A., Pereira, S. & Urbach, H. Lateral position correction in ptychography using the gradient of intensity patterns. *Ultramicroscopy* **192,** 29–36 (2018).

37. Ruan, T. *et al.* Adaptive total variation based autofocusing strategy in ptychography. *Optics and Lasers in Engineering* **158,** 107136 (2022).

38. Zhang, B. *et al.* Ptychographic hyperspectral spectromicroscopy with an extreme ultraviolet high harmonic comb. *Optics express* **24,** 18745–18754 (2016).

39. Henke, B. L., Gullikson, E. M. & Davis, J. C. X-ray interactions: photoabsorption, scattering, transmission, and reflection at E= 50-30,000 eV, Z= 1-92. *Atomic data and nuclear data tables* **54,** 181–342 (1993).

6

SOURCE INTENSITY FLUCTUATION CORRECTION WITH PTYCHOGRAPHY

High harmonic generation (HHG) sources have seen great improvement over the years in terms of output power, however their intensity instability and drift compared to synchrotrons can be problematic. Lengthy ptychography scans, where a constant probe during the scan is assumed, might not converge to a solution with too large variation in the beam power. This chapter tries to mitigate the effects of large power variations by introducing a gain factor in order to allow the ptychography model to dynamically adjust for beam intensity fluctuations during scans, with the aim to improve image reconstruction without significant computational overhead. This method is validated experimentally using a visible light setup to emulate the conditions of EUV microscopy, demonstrating improved image reconstructions under controlled intensity fluctuations.

6.1. INTRODUCTION

Coherent Diffractive Imaging (CDI), in particular ptychography [1], is applied more often in high-resolution extreme UV (EUV) and soft X-Ray (SXR) microscopy applications. CDI exploits phase retrieval techniques to reconstruct images from diffraction patterns generated by illuminating an object with coherent light. Ptychography, an extension of CDI, improves upon this by scanning a coherent illumination probe across the sample at overlapping positions, thereby collecting a series of diffraction patterns to reconstruct the object complex-valued field, i.e. both amplitude and phase information. High Harmonic Generation (HHG) sources, known for producing coherent, high-energy photons in the EUV and SXR regimes, have become increasingly important for these techniques. However, the practical application of CDI and ptychography, particularly with HHG sources, can be challenging.

In a ptychography scan, it is assumed that the illumination intensity and probes $P_{l,m}(\mathbf{r})$ across the series of diffraction patterns remains consistent. As explained in Chapter 5, the forward model from object field $O_{l,n}$ towards intensity of the diffraction patterns $I_k(\boldsymbol{\rho})$ can be described by the following expression,

$$I_k(\boldsymbol{\rho}) = \mathcal{M}\left[\sum_{l=1}^{L}\sum_{m=1}^{M}\sum_{n=1}^{N}\left|\mathcal{D}_{\lambda_l,z}\left[P_{l,m}(\mathbf{r})O_{l,n}(\mathbf{r}-\mathbf{s}_k)\right](\boldsymbol{\rho})\right|^2 + \mathcal{N}(\boldsymbol{\rho})\right], \tag{6.1}$$

6

where k denotes the scan index, l is the index of L wavelengths, m and n are the indices of M illumination modes and N sample modes respectively. $\mathcal{M}$ represents the measurement-related effects at the detector such as masking or clipping values of pixels in the presence of saturation, variation of responsivities of pixels (the "hot" and "cold" pixels), $\mathcal{N}(\boldsymbol{\rho})$ denotes the background noise due to the dark current of the detector or the intensity of a common background signal on the camera due to stray light reaching the detector, $\mathcal{D}_{\lambda,z}$ represents the propagator that depends on the wavelength λ and propagation distance z. $P_{l,m}(\mathbf{r})$ and $O_{l,n}(\mathbf{r})$ are the mth illumination mode of the probe and the nth sample mode of the object, respectively, at wavelength λ_l. $\mathbf{s}_k$ indicates the object's scanning position at the kth scan position. The 2-dimensional vectors $\mathbf{r}$ and $\boldsymbol{\rho}$ represent the spatial coordinates in the sample plane and the camera plane, respectively.

The success of a ptychographic reconstruction partially relies on the stability and coherence of the illumination source [2, 3]. The intensity instabilities associated with HHG sources, i.e. fluctuations in the output harmonic beam intensity, can significantly impact the quality of ptychographic reconstructions. These instabilities can lead to artefacts in the reconstructed images, reduced resolution, reduced image contrast or no convergence to the solution at all.

Although a lot of progress has been made in recent years to improve the performance of EUV and SXR high harmonic generation sources in terms of maximum emitted photon energies and output power [4–8], these sources can suffer from intensity and beam pointing instabilities, especially when compared to the high-end synchrotrons. Addressing the challenges posed by HHG source instabilities in ptychography involves a combination of experimental and computational strategies. Experimentally, techniques such as active stabilization and optimization of the drive laser parameters combined with

interaction medium optimization can reduce intensity fluctuations to a certain extent. However, the typical intensity stability of HHG sources remains between 5% up to 30% relative to the root-mean-square (RMS) value [9–15] during a ptychography scan. Furthermore, long-term drift (in the order of several tens of minutes to hours) in the HHG output power is common due to thermal changes in the system induced by the high-power lasers required to drive the HHG process. The impact of the long-term drift can be reduced by returning to a reference scanning position after a certain appropriate number of scanning positions. The total energy in the diffraction pattern can be used to interpolate the change in intensity over the scan linearly. Changes between these 'checkpoints' remain unknown. Ideally, one could measure the beam power parallel to the ptychography experiment by picking off a small part of the main beam. This is rather straightforward for a visible setup (by using a beam splitter and a photodiode). For EUV, this can be rather tricky without losing too much light. A method has been explored as demonstrated in Appendix B.1.3, which enables online monitoring of the photon flux without introducing any losses but it requires sensing of tiny currents in the 10^{-12} Ampère regime.

Computationally, advanced reconstruction algorithms that incorporate models of the source fluctuations or adaptive correction methods can improve the robustness of ptychographic reconstructions against source intensity instabilities and other imperfections associated with high harmonic generation sources in ptychography. Several advanced computational techniques have been developed to enhance robustness and accuracy. One approach to deal with source pointing instabilities is to include multiple spatial modes (m) of the illumination probe into the reconstruction algorithm [16–20], as shown in Eq. 6.1 denoted by $P_{l,m}(\mathbf{r})$, as it effectively leads to a reduced spatial coherence. Instead of forcing a single-mode assumption, a sum of several coherent modes is used instead (often referred to as a "sum of coherent systems" or shortly, SOCS). A downside of adding more modes is the additional computational load and the additional parameters which needs to be reconstructed.

The Relaxed Orthogonal Probe Relaxation (ROPR) method [2] is another approach to mitigate this problem. By allowing for a more flexible adaptation of the probe model, ROPR can effectively compensate for changes in the illumination that might occur due to source instabilities per scanning position using a given basis of probe modes. This method improves the fidelity of the reconstructed image by ensuring that the probe used in the reconstruction accurately reflects the actual illumination conditions at the cost of computational load. Each of these computational techniques addresses specific aspects of the challenges posed by HHG source instabilities in ptychography. By integrating these methods into the reconstruction process can significantly improve the quality and reliability of ptychographic imaging [2, 16–20].

In this work, we introduce a simplified approach to address the challenge of beam intensity fluctuations in ptychographic imaging by introducing a gain factor σ_k for each measured diffraction pattern. This factor represents a dynamic adjustment mechanism, directly compensating for variations in the beam's power as a function of the scanning position index, k. Unlike the more complex methods previously mentioned, this approach can be integrated into existing ptychographic reconstruction frameworks with-

out imposing a large computational load.

Introducing σ_k into the ptychography model is rather straightforward. By multiplying the probe $P_{l,m}(\mathbf{r})$ at each scanning position by σ_k, the algorithm gains the freedom to adjusts for fluctuations in beam intensity during the scan,

$$I_k(\boldsymbol{\rho}) = \mathcal{M}\left[\sum_{l=1}^{L}\sum_{m=1}^{M}\sum_{n=1}^{N}|\mathcal{D}_{\lambda_l,z}\left[\sigma_k P_{l,m}(\mathbf{r})O_{l,n}(\mathbf{r}-\mathbf{s}_k)\right](\boldsymbol{\rho})|^2 + \mathcal{N}(\boldsymbol{\rho})\right]. \tag{6.2}$$

The gain factor σ_k only allows for retrieval of relatively low frequency modulation of the source intensity. Fluctuations during the exposure at a single scanning position cannot be retrieved as these are averaged out within the diffraction pattern during the acquisition. Only a local gain factor per scanning position relative to the average intensity per frame of the entire scan is retrieved.

It must be stressed that this approach cannot distinguish if a part of the total energy in a captured diffraction pattern moved outside the detection numerical aperture (NA), due to strong diffraction, as this could be perceived as a reduced total photon flux. Additionally, changes in the absorption and reflection function of the sample could be perceived as a source intensity fluctuation. The overlap constraint takes care of these problems to some degree, nevertheless the scanning position dependent gain factor σ_k should be learned at a rather slow rate to avoid over-compensation.

In order to validate this approach, we demonstrate the method in a more controlled environment by scaling down the complexity from HHG-based EUV microscopy to a visible light setup. Light sources in this wavelength regime are typically more stable, where controlled source intensity fluctuations can be introduced which sequentially have to be retrieved through ptychography.

6.2. UP-SCALED VISIBLE LIGHT PTYCHOGRAPHY SETUP

A ptychography setup typically consists of only four subsystems, namely the light source, illumination optics, motorized sample stage, and a camera to detect the diffraction patterns. In the up-scaled experimental setup, with wavelengths and structural dimensions about 30 times larger than in the EUV regime, we start with a three-channel coherent white light fiber laser (FISBA READYBeam-Ind1), which emits light at three distinct wavelengths: 450 nm, 520 nm, and 660 nm. The output power for each channel of the light source can be controlled through software. For the purpose of this study, we exclusively utilize the red channel, corresponding to a wavelength of 660 nm with a natural intensity stability of < 1% (RMS). By adjusting the intensity of the light source in a controlled manner, we can introduce a known intensity fluctuation during the ptychographic scan.

The collimated output beam is made divergent using a negative lens, which illuminates an aperture of about 1 mm in diameter. The aperture is imaged onto the sample plane by a plano-convex lens with a focal length of 100 mm. Imaging the aperture rather than directly illuminating the sample with a focused probe ensures that the probe on the sam-

ple is localized and enclosed (by the edges of the aperture), which is beneficial for ptychography as described in Chapter 2. On top of that, by illuminating the aperture with a divergent beam with the negative lens, we introduce a curved wavefront when imaging the aperture, adding some phase diversity to the probe while still maintaining a localized probe. The illumination field size (i.e. the probe size) can be easily controlled by changing the size of the aperture. In this experiment we keep the probe size approx. 500 by 800 µm.

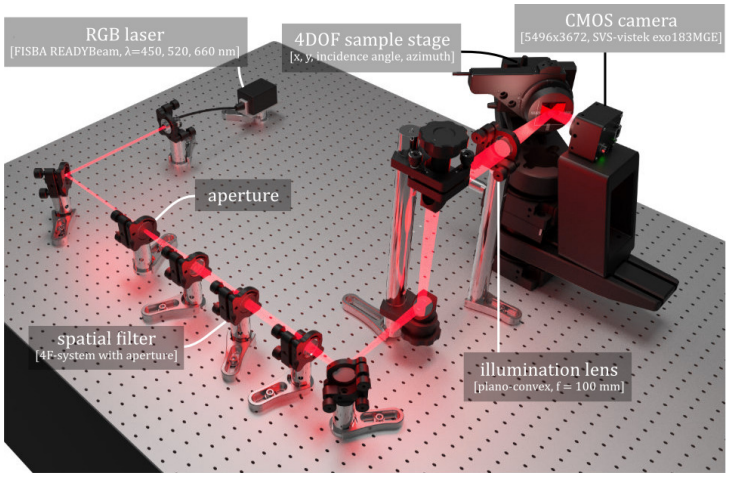

Figure 6.1: The up-scaled experimental ptychography setup in the visible light regime includes a three-channel white light source (FISBA READYBeam-Ind1) at 450 nm, 520 nm, and 660 nm. The light source's output power per channel can be controlled programmatically through a MATLAB routine. The output beam, which is divergent, illuminates an aperture, after which it passes through a 4F system that includes a Fourier spatial filter. After the spatial filter, the image of the aperture is re-imaged again onto the sample plane with the indicated plano-convex lens (f = 100mm), ensuring a localized, enclosed probe on the sample. The sample is movable in four dimensions, which include the x and y directions driven by linear stages and two rotational stages for adjusting the incidence angle and the azimuth rotation. The diffracted light from the sample is captured by a CMOS camera. In the demonstrated experiments, the sample and camera are set under an angle of 45 degrees with the normal of the sample.

A sample is positioned on a motorized platform, which allows for movement in four dimensions. This includes linear movements in the x and y directions driven by linear stages and rotational motors for the incidence angle and azimuth rotation. As the sample is scanned in the x,y plane, the resulting diffracted light propagates from the sample to an 8-bit CMOS camera (SVS-Vistek eco183MGE). The 20-megapixel camera has 5496 by 3672 pixels with a pixel size of 2.4 microns. This camera is able to move goniometrically around the sample, enabling the option to capture light at various angles in a reflection orientation.

6.2.1. RESULTS

A Siemens star target has been nano-fabricated, similar to the one described in Chapter 5 but with a different layer thickness of 50 nanometer[1] (compared to 20 nanometer in the EUV case) and up-scaled features by a factor 30 in the lateral direction. The relatively large target has a radius of 1500 microns and consists of 90 spokes, i.e. 2 degrees per spoke. The spoke width at the edge is about 50 microns down to 200 nanometers in the center. As shown in the brightfield microscope image in Fig. 6.2, two spokes in the star are damaged. Additionally, a black streak can be observed in the top-right of the Siemens star. This is a piece of residue from the lift-off process during manufacturing.

This sample is placed in the 4DOF sample holder and is oriented in such a way that the beam illuminates the target with an angle of incidence of 45 degrees. Only the red channel, i.e., at 660 nm, is utilized for this work. This setup starts with a reference measurement on the Siemens target. The target is scanned at 285 scanning positions, distributed in a relatively large region of 2.2 mm by 2.2 mm using Poisson Disc Radius distribution, as shown in Fig. 6.2.

A set of 285 diffraction patterns are captured by the CMOS camera at a distance of 35.62 mm from the sample, i.e. in the Fresnel regime given the propagation distance, wavelength and an estimated probe size of approximately 300 micron (Fresnel number is approximately equal to 1). As the setup is oriented in a reflection orientation, we have to perform tilted plane correction (TPC) in order to correct for conical diffraction. This is repeated for a dark frame where the beam is turned off, after which this is subtracted from the measured diffraction patterns.

Due to the small pixel size of the camera (2.4 microns), we apply 6-by-6 pixel binning, reducing the number of pixels in the diffraction patterns from roughly 20 million down to only 0.6 million. By doing so, we reduce the field of view that contributed to each diffraction pattern from 9.8 mm by x 13.5 mm down to 1.6 mm by 2.2 mm so that the total size of the dataset is significantly reduced. Given the propagation distance, tilt angle and the camera's size, we have a maximum obtainable (diffraction-limited) resolution of 2.7 microns in the tilt direction and 2.2 microns in the non-tilt direction.

The ptychography dataset is reconstructed using the automatic differentiation-based PtychoFlow platform, as described in Chapter 5. As an initial guess for the sample, we use a flat field of ones in the entire field of view, while for the probe, we use an oval aperture function of 150 by 300 microns in diameter. No regularization is applied in the reconstruction besides a probe support constraint, see Chapter 5, (with a support weight of 0.1) to ensure that the probe is reconstructed in the center of the field of view. A learn rate for both the probe and sample is set to 0.05, for which an object is reconstructed after 50 epochs.

The reconstruction of the Siemens star corresponds to the reference bright field microscope image where the aforementioned defects (the missing spokes and the black streak) are visible. The spokes are well reconstructed down to a spoke width of 3 microns, close

[1] The thickness has not been scaled by a factor of 30 but just by a factor of 2.5. This thickness has been chosen from a nanofabrication point of view as it is a more reliable recipe compared to thicker layers.

to the diffraction limit, as shown in Fig. 6.5 and Fig. 6.6. Although a complex-valued object is retrieved for all ptychography experiments, we only show the magnitude of upcoming reconstructions from now on because of the relatively low phase contrast of the target due to the small height of the structures relative to the wavelength, as shown in Fig. 6.2.

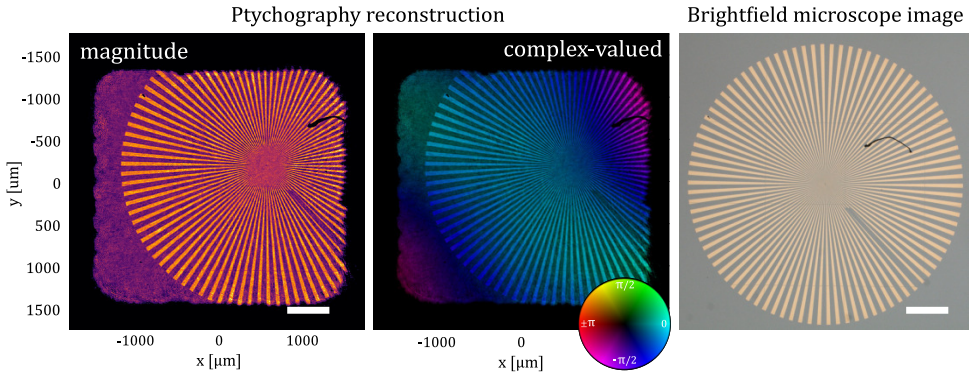

Figure 6.2: A Siemens star target made of 50 nanometer gold on top of a silicon substrate has been reconstructed by scanning the illumination probe (λ = 660 nm) across the target without introducing any fluctuations in the beam power. The left figure shows the magnitude reflection function of the target. The center figure represents the actual complex-valued reconstruction, where the hue represents the phase and the brightness represents the amplitude. Not much phase contrast can be observed due to the rather small height of the structure relative to the wavelength but more apparently a global phase profile across the region is observed. The right figure is a reference image taken by a bright field microscope. The black streak in the top-right of the Siemens star is a residue from the lift-off process while manufacturing the sample.

Two probe modes are simultaneously reconstructed with the object. These two modes are assumed to be sufficient as when more modes are added they do not reconstruct to any realistic probes besides noise with less than a few percent in each mode except for the two first modes. The reconstructed probes, see Fig. 6.3, show indeed a sharp edge from the aperture and a curved wavefront due to the introduced defocus as expected. This reconstruction, without any introduced fluctuation of the source power, acts as a reference reconstruction.

The same scanning grid has been used for five more experiments where instead, uniformly random fluctuations of the output power of the beam have been added. We allow the output power to vary uniformly randomly between the maximum and a given fraction (i.e. 90%, 80% down to 50%) in order to avoid saturation of the camera, and we only reduce the dynamic range.

The datasets undergo the same pre-processing procedure as the reference measurement and identical hyperparameters are used for the reconstruction. The controlled experiments with introduced random variations in power output demonstrated a correlation between power stability and image fidelity. As the power variations increased, the quality of the reconstructions degraded. Spots with increased intensity appeared in the sample plane, which coincided with the scanning positions. Eventually, the power variations reach a threshold where the object can not be resolved anymore, as shown in the top

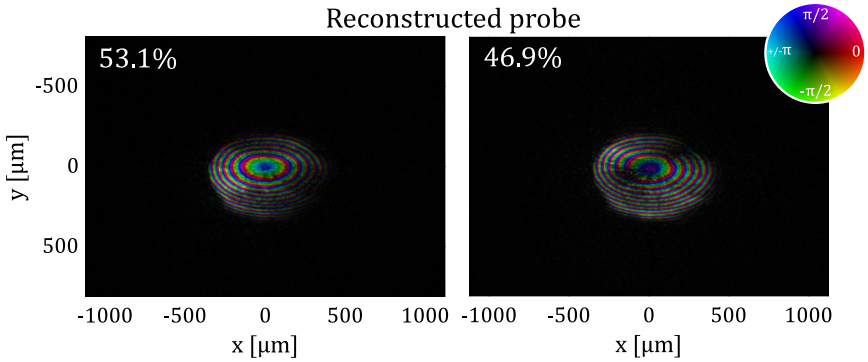

Figure 6.3: Two probe modes have been reconstructed, which somewhat equal power in each mode, approximately 53 and 47 percent of the total beam power, respectively, with a probe size of 806 by 523 microns. The hue in the figure represents the phase and the brightness represents the amplitude of the probe. Two probe modes are considered to be sufficient, as only noise is reconstructed (overfitting) with a total power of less than a few percent when more modes are added. As the aperture is illuminated with a divergent beam, which is imaged onto the sample, we have a probe with relatively sharp edges and a non-flat wavefront, as shown by the reconstructed phase.

6

row of Fig. 6.4.

The introduction of the power factor (σ_k) inference improved the reconstruction quality significantly and removed the high-intensity spots in the reconstruction for the datasets that are corrupted by power fluctuations. The cases where the conventional method was not able to converge to a solution (40 and 50 percent intensity fluctuation) were able to be reconstructed when enabling the training of the power factor σ_k.

When we take a closer look at the two reference reconstructions of the Siemens star where no power fluctuations are introduced, it can be observed that the reconstruction quality (in terms of resolution) did not reduce when power factor training was enabled. For the 50%-case, the final resolution is marginally reduced. This comparison is made by unwrapping the Siemens star in polar coordinates. First, the center of the Siemens star is selected. From that point, the data is interpolated to radial and angular coordinates, resulting in the image in Fig. 6.5. The radial dimension can be converted to a spoke width by using the prior knowledge of the radius of the Siemens star and the angle of a spoke. This process linearizes the spokes, which allows for a 1D Fourier transform in the horizontal direction, resulting in a spectrogram as shown in Fig. 6.6. The spectrogram shows peaks at the expected angular frequency of 0.25 spokes per degree (and its harmonics), corresponding to the spoke angle of 2 degrees. The power in this frequency band drops off when approaching the center of the Siemens star, where it eventually drops to the noise level. The center of the Siemens star has to be set to a few pixels accurately (i.e., about 3 microns) in order to minimize distortions in the polar coordinate representation. Ideally, the center of the Siemens star has to be selected within a few pixels accurate. If the center is too far off from the true center, it will result into distorted lines and thus spectral broading in the spectrogram (Fig. 6.5), especially near the center.

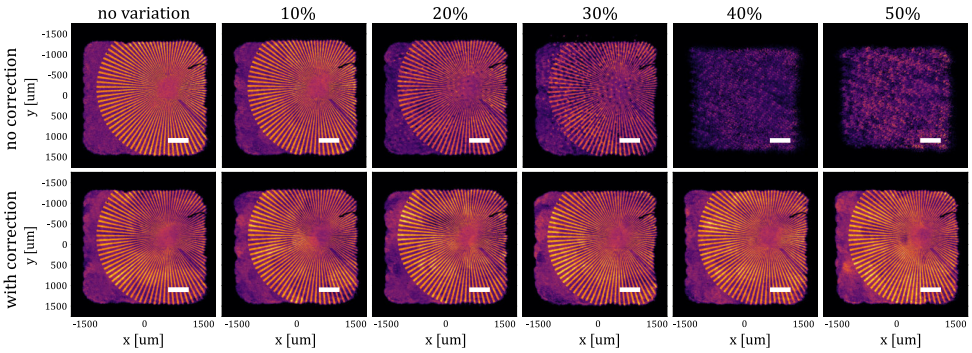

Figure 6.4: **Top-row:** The power output of the light source can be controlled when the output power is perturbed by adding random variations, ranging from no variation up to 50 percent relative to the maximum power. Identical scans are performed for each dataset and reconstructed with equal hyperparameters for the reconstruction. The reconstruction degrades when the random variations per scanning position are increased, and eventually, it does not converge anymore. **Bottom-row:** By enabling scanning position dependent gain factor σ_k inference during the reconstruction, the entire object can be reconstructed for all shown cases. Each reconstruction is carried out with 50 epochs and equal learning rates for the probe, sample and gain factor which are 0.05, 0.05 and 0.001 respectively. All reconstructions are without any regularization besides probe support to ensure that the probe is reconstructed in the center of the field of view.

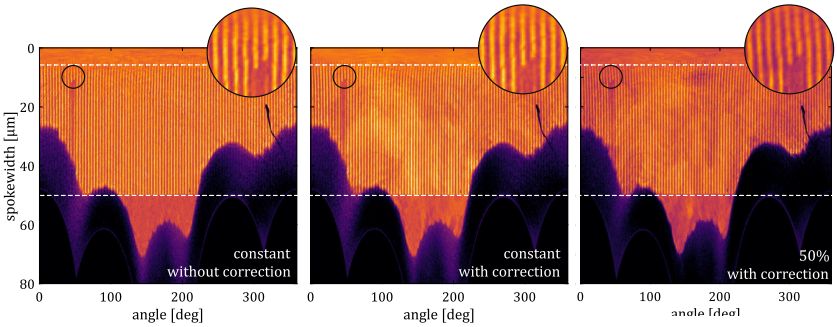

Figure 6.5: The Siemens star can be unfolded by interpolating and plotting the Siemens star in polar coordinates. In this representation, the vertical axis is the radial dimension of the Siemens star, which corresponds to the spoke width, while the horizontal coordinates represent the angular dimension. This procedure is repeated for the reference measurement, both with and without intensity training during the reconstruction, and for the case where a 50% fluctuation is introduced with intensity training enabled. The lower white dashed line represents the edge of the Siemens star, while the top dashed line represents the point up until the spokes are still resolved.

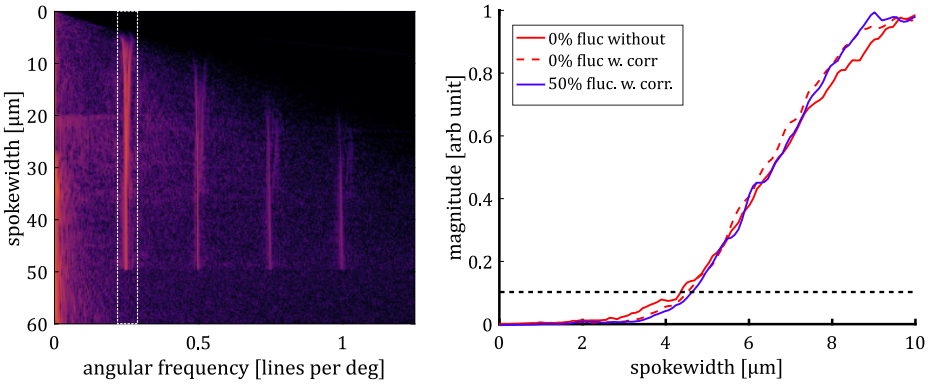

Figure 6.6: A Fourier transform can be performed in the horizontal direction, line-by-line, as a function of the angle to build a spectrogram. Peaks are observed in the power spectrum at an angular frequency of 0.25 and its harmonics, corresponding to the spoke angle of 2 degrees. The power in these peaks decreases when approaching the center of the Siemens star. This is shown in the figure on the right where the columns between the dashed lines are summed horizontally and plotted as a function of the spoke width. This is repeated for the reference reconstruction (i.e. zero fluctuation without correction), with correction and when 50% fluctuation is introduced. Comparable resolution can be achieved when intensity training is enabled when compared to the reference reconstruction, even when 50% intensity fluctuation is introduced.

6

All the power factors were set at one as an initial guess. After the iterative reconstruction converged to a solution it is expected that the retrieved power factors can be related to the input power factors of the source laser. By representing these values as a heatmap in relation to their scanning positions, we can indeed observe a strong correlation between the physical power values and the reconstructed values. When plotted against each other, these values show a linear relationship with offset and gain factors of 0.474 and 0.823, respectively. Additionally, it significantly enhances the quality of the reconstruction, particularly for the cases with a high power fluctuation above 30%.

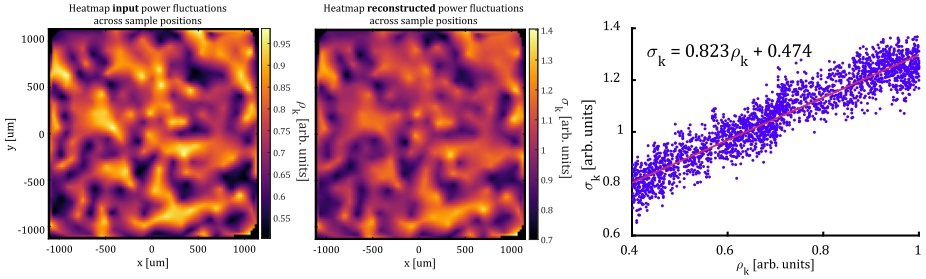

Figure 6.7: The output power from the light source is linearly decreased per scanning step from 100% down to 40%, which only seems to converge to a solution when allowed for intensity fluctuation inference. The scanning power coefficient σ_k per position k (relative to the average probe power during the entire scan) can be retrieved and compared to the input power factor ρ_k for the power-controlled light source.

6.2.2. CONCLUSION

High harmonic generation sources typically suffer from relatively lower intensity stability performance than higher-end synchrotrons, which can be problematic for imaging methods like ptychography. Solving this issue through hardware can be rather difficult, so computational approaches can help mitigate these problems. This work has demonstrated that a simple addition to the general ptychography framework makes the reconstruction more robust to large intensity fluctuations during a ptychography scan. Adding a scanning position-dependent multiplication factor σ_k allows for training corrective values of the input power without adding much complexity or computational load (single variable per diffraction pattern) to the algorithm.

This method is validated experimentally on a up-scaled visible light ptychography setup at 660 nanometer. In this setup, a 50 nanometer thick golden Siemens star target on a silicon substrate is used as a test object and oriented in a reflection mode at 45 degrees angle of incidence. The test target is scanned several times with the same scanning pattern, but for each scan, a given power fluctuation of the beam power is introduced, ranging from zero percent fluctuation up to fifty percent relative to the maximum power.

Without enabling the inference of this additional power factor σ_k, it was not possible to reconstruct the cases with large fluctuation, while the others did converge to a Siemens star-like object but possessed a degraded reconstruction quality and artifacts. When the power factor training was enabled, it was possible to reconstruct each case even in the presence of substantial intensity fluctuations. The linear relationship between the retrieved and input power factors demonstrates that the power fluctuations were corrected using this method.

In conclusion, we presented an effective way to mitigate large source intensity fluctuations associated with HHG source instabilities by a simple computational approach for correcting intensity fluctuations in ptychography. Although this approach does not take possible variation of the of the shape of the various probe modes into account, it can reduce intensity stability requirements for table-top HHG-based ptychography.

BIBLIOGRAPHY

1. Rodenburg, J. M. Ptychography and related diffractive imaging methods. *Advances in imaging and electron physics* **150,** 87–184 (2008).
2. Odstrčil, M. *et al.* Ptychographic coherent diffractive imaging with orthogonal probe relaxation. *Optics express* **24,** 8360–8369 (2016).
3. Yao, Y., Liu, C. & Zhu, J. Compensation for the setup instability in ptychographic imaging. *Optics Express* **25,** 11969–11983 (2017).
4. Popmintchev, T., Chen, M.-C., Arpin, P., Murnane, M. M. & Kapteyn, H. C. The attosecond nonlinear optics of bright coherent X-ray generation. *Nature Photonics* **4,** 822–832 (2010).
5. Karst, M. *et al. Multipass cell post-compression at 515 nm as an efficient driver for a table-top 13.5 nm source* in *EPJ Web of Conferences* **287** (2023), 08008.
6. Kirsche, A. *et al.* Continuously tunable high photon flux high harmonic source. *Optics Express* **31,** 2744–2753 (2023).
7. Loetgering, L., Witte, S. & Rothhardt, J. Advances in laboratory-scale ptychography using high harmonic sources. *Optics Express* **30,** 4133–4164 (2022).
8. Boutu, W., Ducousso, M., Hergott, J.-F. & Merdji, H. Overview on HHG high-flux sources. *Optical technologies for extreme-ultraviolet and soft X-ray coherent sources,* 63–78 (2015).
9. Leitner, T. *et al.* Shot-to-shot and average absolute photon flux measurements of a femtosecond laser high-order harmonic photon source. *New Journal of Physics* **13,** 093003 (2011).
10. Maltezopoulos, T. *et al.* A high-harmonic generation source for seeding a free-electron laser at 38 nm. *Applied Physics B* **115,** 45–54 (2014).
11. Goh, S. *et al.* Single-shot fluctuations in waveguided high-harmonic generation. *Optics express* **23,** 24888–24902 (2015).
12. Künzel, S. *et al.* Shot-to-shot intensity and wavefront stability of high-harmonic generation. *Applied optics* **54,** 4745–4749 (2015).
13. Zhou, J., Peatross, J., Murnane, M., Kapteyn, H. & Christov, I. Enhanced high-harmonic generation using 25 fs laser pulses. *Physical Review Letters* **76,** 752 (1996).
14. Volkov, M. *et al.* Reduction of laser-intensity-correlated noise in high-harmonic generation. *Optics express* **27,** 7886–7895 (2019).
15. Klas, R., Kirsche, A., Tschernajew, M., Rothhardt, J. & Limpert, J. Annular beam driven high harmonic generation for high flux coherent XUV and soft X-ray radiation. *Optics Express* **26,** 19318–19327 (2018).

16. Clark, J. N. & Peele, A. G. Simultaneous sample and spatial coherence characterisation using diffractive imaging. *Applied Physics Letters* **99** (2011).

17. Abbey, B. *et al.* Lensless imaging using broadband X-ray sources. *Nature Photonics* **5,** 420–424 (2011).

18. Thibault, P. & Menzel, A. Reconstructing state mixtures from diffraction measurements. *Nature* **494,** 68–71 (2013).

19. Whitehead, L. *et al.* Diffractive imaging using partially coherent x rays. *Physical review letters* **103,** 243902 (2009).

20. Parks, D., Shi, X. & Kevan, S. Partially coherent x-ray diffractive imaging of complex objects. *Physical Review A* **89,** 063824 (2014).

7

QUANTITATIVE DENSITY RETRIEVAL OF GAS JETS FOR HIGH HARMONIC GENERATION WITH A COMPACT SCHLIEREN IMAGING SYSTEM

This work describes the implementation of a compact schlieren imaging technique for quantitatively measuring atomic density profiles in a gas jet-based high harmonic generation (HHG) source. This technique enables a quantitative comparison between HHG light sources, taking into account different nozzle geometries, backing pressures, and vacuum systems. The simplicity of schlieren imaging makes it a suitable standardized inspection tool for gas jet-based HHG sources. Several gas jet profiles at different backing pressures were analyzed with this method while capturing HHG spectra with an EUV spectrometer.

7.1. INTRODUCTION

High-order harmonic generation (HHG), driven by high-power laser systems, have seen impressive advancements in recent years [1, 2]. The typical low efficiency of HHG in the EUV and Soft X-Ray regime leads to the need of more powerful drive lasers with shorter pulse duration. The introduction of, for example, Chirped Pulse Amplification (CPA) [3], high pulse energy femtosecond lasers (like titanium sapphire lasers), and more recently, the availability of commercial ytterbium-doped fiber lasers [4–8] has enabled the generation of coherent extreme ultraviolet (EUV) light in the range of a few micro Watts. This has resulted in table-top EUV sources with sufficient photon flux for scientific applications like coherent imaging [1, 9–11] (as demonstrated in Chapter 5), spectroscopy [12] and even industrial applications [13, 14]. Despite these advancements, there is still a demand for higher photon fluxes to improve acquisition times and system stability, which calls for further optimization efforts in HHG based EUV sources.

As stated in Chapter 3, the HHG process depends on the response of a single atom to an applied electric field by the drive laser [15–17]. From the semi-classical point of view, the ponderomotive energy is mainly relevant for the maximum photon energy as described in Chapter 3. This ponderomotive energy depends on the wavelength and power of the drive laser [18]. On the macroscopic scale, a collection of single atoms need to emit the generated higher harmonics coherently through phase matching. Phase matching is a balancing process of induced phase mismatch between the generated harmonics and the drive laser due to, for example, the focusing geometry of the drive laser or the refractive index differences of the gas jet or the generated plasma[19]. The focusing geometry of the drive lasers and the medium length within the field combined with the atomic density strongly affects the phase matching conditions [18, 20–22]. Especially the focusing geometry becomes of importance for Ytterbium-doped fiber lasers with their relatively lower energy pulses compared to Nd:YAG lasers, which requires tighter focusing and therefore a strong phase profile. Optimizing the phase matching conditions results in a higher output of coherent harmonics and therefore an improved conversion efficiency.

The theoretical understanding of the optimal geometry for the HHG medium and focusing of the drive laser continuously increases [15], however there are a wide range of HHG systems available and it is not trivial to compare them. They vary from low-pressure capillaries [23–25] and cells [26, 27] to both pulsed and continuous high-pressure gas jets [28, 29]. Note that higher harmonics can also be produced in solids and liquids [30–32], but gas-based systems are more common due to their relatively higher photon fluxes, higher photon energies and their relative simplicity. In this work we only focus on continuous gas jet based systems.

In order to make a comparison between different light sources and their efficiency, it is desirable to compare the number of atoms which interact with the laser field given that the parameters of the drive laser and the medium are different amongst different systems. Therefore there is a need to retrieve the medium volume and atomic density in a given HHG system. Defining the medium length in capillaries and low pressure cells is rather straight forward as the dimensions are known and the gas is contained within a

fixed volume. In this case the pressure can be directly measured with a pressure gauge to retrieve the gas density using the ideal gas law. For gas jets however, this can be a bit more of a challenge as the gas is freely injected into a vacuum system and therefore not enclosed within a well defined volume. The gas density profile within the medium depends on the nozzle geometry, backing pressure and vacuum pumping speed. As these can differ significantly per HHG system, it is hard to compare systems with only the knowledge of the backing pressure.

Interferometry based methods are able to retrieve the density due the introduced optical path difference caused by the difference in the refractive index of the gas jet [18, 33–37]. However, interferometry approaches can be quite tricky to implement due to vibrations introduced through the scroll pumps, turbo molecular pumps and the gas line feeding the gas jet itself. Other phase retrieval methods could possibly be applied to retrieve the density profile but those methods usually come with a computational overhead which is not ideal for online monitoring.

A different approach has been proposed [38], which associates the observed plasma intensity with a set of reference measurements. First, the vacuum chamber is saturated to a certain pressure of interest, i.e. there is no gas jet but an increased static pressure. A plasma is created at this static pressure and an image is acquired. The peak brightness of the plasma is associated with the static pressure. This is repeated for a set of pressures to populate a look-up table (LUT) which can be used to reference the observed plasma intensity with the LUT during HHG. Although this approach circumvents interferometry, it has quite some limitations. First of all, the technical inconvenience that, if a gas jet pressure above 1 bar is desired, one would have to saturate the entire vacuum chamber to a positive pressure difference. Most vacuum chambers (especially those with glass windows) are not designed for positive pressure differences and could therefore damage the vacuum system. On a more fundamental level, this approach requires accurate knowledge of the intensity profile of the drive laser within the gas jet in all three spatial dimensions as it is hard to differentiate a change in laser power and a change in pressure in the gas jet. On top of that, this calibration process has to be repeated as soon as the settings of the drive laser have been changed.

In this work, we demonstrate a compact method, based on schlieren imaging, to retrieve the atomic density profile in a gas jet based HHG source, which could potentially be used to compare and optimize the efficiency of HHG light sources.

7.2. SCHLIEREN IMAGING

Schlieren[1] imaging systems have been widely applied to visualize fluctuations in the density of gases, from aerodynamics of airplanes [39] to gas flows in industrial applications [40]. This technique exploits the fact that the density of these gases ρ affects the refractive index n of the medium, described by the Gladstone-Dale (GD) relation [41],

$$n = \kappa\rho + 1. \tag{7.1}$$

[1] The word 'schlieren' refers to the German word for 'streak'.

The κ factor in Eq. 7.1 represents the Gladstone-Dale constant of a particular gas, which has been experimentally determined [42] to be $0.1574 \cdot 10^{-3}$ m^3 per kg for argon and a wavelength of 694 nm. In a gas mixture, the total refractive index is calculated by summing the contributions of each individual gas, each characterized by its own specific term $\kappa_i \rho_i$. When light passes through a medium with a density gradient, i.e. a gradient in the refractive index, the light rays are refracted by a certain angle ε. The introduced deflection angle ε can be geometrically derived for an object with given thickness Δz, see Fig. 7.1, by taking two points x_1 and x_2 located Δx from each other with associated refractive indices n_1 and n_2 and the speed of light in vacuum c (as used in the figure),

$$\Delta\varepsilon = \frac{n_0}{n_1 n_2} \frac{n_1 - n_2}{\Delta x} \Delta z, \tag{7.2}$$

where n_0 represents the ambient refractive index and is assumed to be equal to one. By taking the limit where the differences become infinitesimally small, the equation simplifies to:

$$\frac{\partial \varepsilon}{\partial z} = \frac{1}{n_0} \frac{\partial n}{\partial x}. \tag{7.3}$$

In order to retrieve the total induced angle deviation by an object with a thickness z, we have to integrate along the z axis,

$$\varepsilon = \frac{1}{n_0} \int \frac{\partial n}{\partial x} \mathrm{d}z. \tag{7.4}$$

This equation is the mathematical basis for schlieren imaging [43]. For a 2D schlieren object of length z with a constant gradient for the refractive index, this integral can be simplified by multiplying the gradient with the total length. For an axis-symmetric schlieren object, like gas jets, an Abel-transform [44, 45] should be applied or for more complex 3D flows, a tomographic Radon approach can be performed [46, 47].

In a schlieren imaging systems this behaviour, as described by Eq. 7.4, is exploited by either blocking or allowing the refracted light rays to pass, creating contrasts which correlate with the gradient of the refractive index. The simplest form is illustrated in Fig. 7.1, where the light beam that is deflected moves away from the knife edge, resulting in more photons reaching the observer. The amount of beam deflection can be retrieved as a contrast $C(x)$,

$$C(x) \propto S \int \frac{\partial n}{\partial x} \mathrm{d}z, \tag{7.5}$$

with S being the sensitivity of the schlieren system. Therefore this suggests that the schlieren methodology is a relatively simple and straightforward approach to retrieve the refractive index profile of a gas target.

7.3. HIGH HARMONIC GENERATION EUV BEAMLINE WITH INTEGRATED COMPACT SCHLIEREN IMAGING SYSTEM

In this work we apply the imaging system on a gas jet based HHG source. The HHG source is driven by a Ytterbium-doped fiber laser with a center wavelength at 1030 nm at

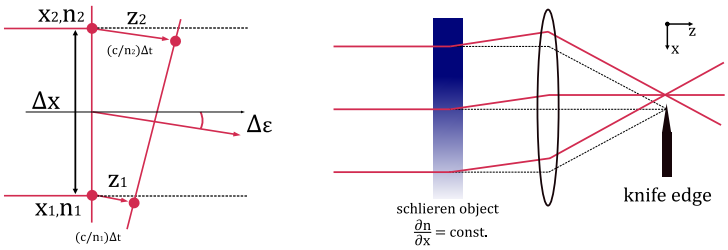

Figure 7.1: Light rays which passes through an schlieren object get deflected due to the gradient in the refractive index, which can be derived geometrically. A schlieren imaging system introduces contrast by placing a knife edge in the beam path, selectively blocking or allowing more photons to pass depending on the gradient of the refractive index.

a repetition rate of 600 kHz and set to at an average power of 50 W before compression. After non-linear compression, with a power efficiency of 68%, by a Krypton-filled hollow core fiber and a set of chirped mirrors, the light is focused into a vacuum chamber with a plano-convex lens of 80 mm. The focus is placed between a copper nozzle piece with an opening aperture of 300 micrometer and a gas catcher. The nozzle is pressurized with argon up to 10 bar. A gas catcher is placed on the opposite side of the nozzle about 400 micrometer away. The gas catcher is directly attached to a scroll pump to ensure that the vacuum level maintains below 10^{-2} mbar when the argon gas is injected into the vacuum system. An ambient pressure of 10^{-6} mbar is reached without gas injection.

When the argon gas jet interacts with the high-power infrared laser, as shown in Fig. 7.3, a plasma forms in which higher harmonics up to the EUV regime are produced. These harmonics then travel to a second vacuum chamber, where the driving laser is separated from the Extreme Ultraviolet (EUV) light through a set of Brewster mirrors. Any residual IR light is blocked by an aluminum foil of 200 nanometer thick. The resulting EUV light can be analyzed using an offline EUV spectrometer, as illustrated in a 3D rendering in Fig. 7.2.

To obtain the density profile of the gas jet in the HHG system, a schlieren system has to be implemented perpendicular to the infrared (IR) beam and the gas jet. Common designs for schlieren imaging include the Toepler double lens system [48] and the Z-type schlieren system [40, 49], which uses two parabolic mirrors. These methods utilize a collimated beam to illuminate the schlieren object, with the light passing through the object only once. The second lens in these setups is used to form an image of the light source at the location of a knife edge. Then, a camera equipped with an objective lens captures the image of the object.

However, these configurations require a vacuum chamber equipped with two aligned windows (entry and exit window), which is not present in the current vacuum chamber. Integrating a standard single-pass schlieren system in such an system is not an option. Therefore, a double-pass, single optic schlieren system, as shown in Fig. 7.2, is chosen instead [40]. This alternative approach is more feasible for the existing vacuum chamber configuration and double passing the jet enables higher sensitivity or a smaller form

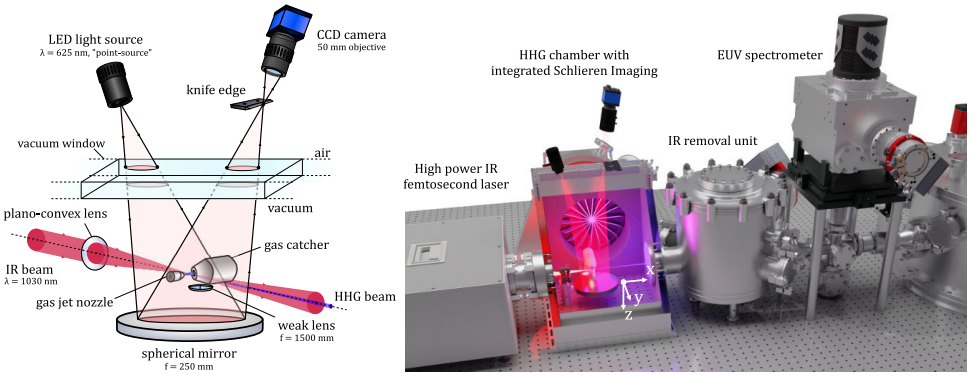

Figure 7.2: **Left:** A schematic overview of the compact schlieren imaging setup within a high harmonic generation vacuum chamber. The drive laser is focused between the gas jet nozzle and gas catcher resulting in a plasma where the higher harmonics are generated. A spherical mirror with a focal length of 250 mm is placed just below the gas jet which is illuminated by a LED light source which acts as a "point source". The back reflected light forms an image of the light source outside the vacuum chamber, where a knife edge is placed. A CCD camera with a 50 mm objective and two times extender captures the light and is focused onto the gas jet. **Right:** A 3D render of the High Harmonic Generation source with an integrated schlieren setup, showing the cross-section of the vacuum chamber where the HHG source resides. The generated harmonics propagate to the next vacuum chamber where the drive laser is separated from the EUV light. The generated EUV light can be inspected with an offline EUV spectrometer.

factor [33].

A spherical mirror with a focal length (f = 250 mm) is placed just below the gas jet and gas jet system in the vacuum chamber. Note that this is significantly shorter compared to typical schlieren system where optics in the order of meters are not uncommon [50–52]. The mirror is not mounted and rests on the bottom plate of the chamber. The mirror is illuminated close to normal incidence with a monochromatic LED light source (λ = 625 nm) which is placed outside the vacuum chamber. The back reflected light by the spherical mirror leaves the vacuum chamber through the same window where an image is formed of the LED source. At this point a knife is placed in a plane which is parallel with the gas jet and perpendicular to the beam direction of the drive laser. A CCD camera (SVS-Vistek ECO445M) with a 50 mm camera objective (Edmund Optics F2.0/50 mm 59873) combined with a C-mount 2x extender (Computar EX2C) is focused onto the gas jet and gas catcher assembly. A schematic overview of the system can be found in Fig. 7.2. For systems which have a relative small window size one can implement a beamsplitter between the LED light source and the camera to illuminate the mirror at normal incidence. This approach comes at the costs of a reduced intensity captured by the camera.

7.4. RESULTS

As shown in Fig. 7.3, the schlieren camera captures both the gas jet nozzle (in the top of the field of view) and the gas catcher (in the bottom of the field of view) after a manual rotation and cropping of the raw image. When argon is injected into the vacuum

chamber, a contrast can be observed between the nozzle and catcher, as illustrated in Fig. 7.3. To compensate for the uneven background, a series of 500 reference images were captured in the absence of any gas, i.e. these images are intended to be used as background frames. These images have been averaged and subtracted from the frames which contain the gas jet, isolating the schlieren contrast. See the inset in Fig. 7.3 and Fig. 7.5.

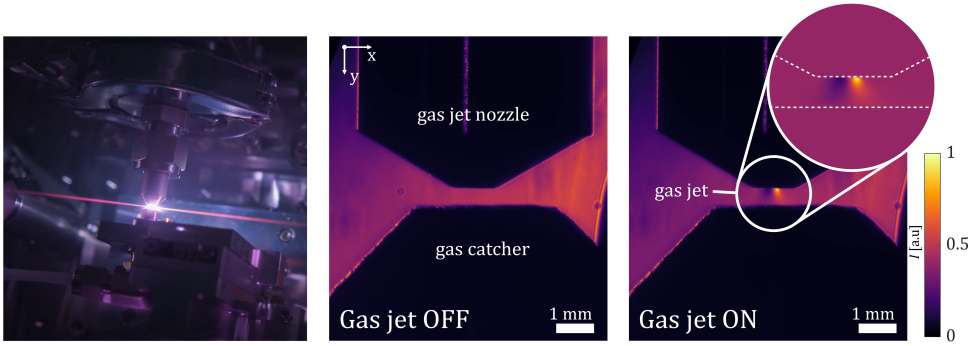

Figure 7.3: **Left:** The high power IR beam is focused between the gas jet nozzle and the gas catcher, leading to a plasma which can be observed through the vacuum window. **Center:** In the schlieren imaging system we focus onto the gas catcher and gas jet nozzle. The background is not uniform due to slightly non-uniform illumination. This can be corrected by subtracting a background image, i.e. a reference image without a gas target. **Right:** When the gas jet is turned on, a contrast can be observed. The contrast can be enhanced and corrected for non-homogenities in the background by subtracting the background image. The background corrected image is shown in the circular inset. The dashed white lines mark the location of the nozzle and gas catcher.

The gray values measured by the imaging system are proportional to the gradient of the refractive index in the gas jet via the induced deflection angle ε. The retrieved gray values are not intrinsically quantitative as the contrast also dependent on system specific parameters such as knife edge placement and focal lengths of the used optics. Calibration of these gray values can be achieved, following the method proposed by [53], by placing a weak lens at the same plane as the gas jet. The weak lens refracts the light ray at a defined angle ε as,

$$\tan\varepsilon = \frac{r}{f} \approx \varepsilon, \tag{7.6}$$

where r represents a radial point within the lens aligned with the knife edge, and f the focal length of the weak lens. In the vacuum chamber of the HHG source, a lens with a diameter of 12.7 mm and a focal length of 1500 mm is placed, as shown in Fig. 7.2. By applying Eq. 7.6 along with the known focal length and radius of the lens, the dynamic range of the schlieren system can be determined if the full dynamic range of the camera is utilized. This results in a maximum calibration range of ±4.2 mrad. The range of the system mainly depends on the dynamic range of the camera and how much light is cut-off with the knife edge.

A set of 500 images were captured of the weak lens in the schlieren system with an exposure time of 5 ms and averaged. A linear response along the x-direction, perpendicular

to the knife edge, is observed in the schlieren image as shown in Fig. 7.4. The response is fitted with a linear function to retrieve a calibration contrast curve C to convert the gray values to deflection angles, where the slope defines the sensitivity S. The actual dynamic range and resolution of the schlieren system, as shown in Fig. 7.4, is ±2.1 mrad with a resolution of 16.5 µrad respectively considering a relatively low dynamic range of the CCD camera (8-bits).

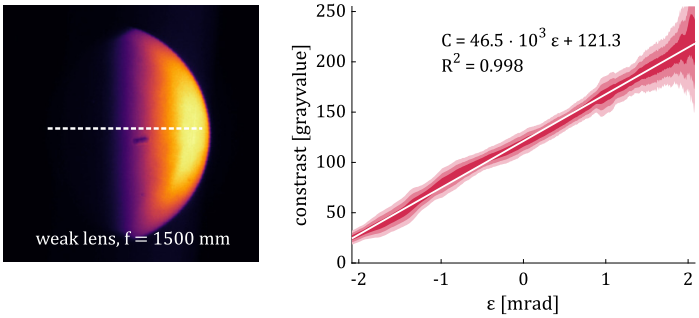

Figure 7.4: A weak lens, with a focal length of 1500 mm, is placed in the field of view of the schlieren imaging system. A linear gradient can be observed across the lens due to the introduced angular deflection. With a known focal length of the lens, a measured contrast or gray value C can be associated to an introduced deflection angle ε in order to calibrate the schlieren imaging system.

A schlieren contrast is measured for an argon gas jet as shown in Fig. 7.5, with a backing pressure of 4 bar in this particular image. An indication of the shape of the density profile can be retrieved by numerically integrating the measurements along the x axis, as schlieren visualizes the gradient of the refractive index or the atomic density (Eq. 7.4). In this case, as intuitively expected, the profile shows features of a Gaussian-like profile. Instead of integrating the data itself, the first order derivative of a Gaussian is fitted to the data. This is used to reconstruct a fitted Gaussian profile and is repeated for each line in the y-direction in the measured dataset, yielding a full reconstructed jet profile as shown in Fig. 7.5.

The light propagates through the gas jet, which has a certain thickness along the z axis. The measured contrast corresponds to a projection function of the refractive index gradient. In the case of an axis-symmetric gas flow it is common to apply the Abel inversion transform [33, 54–57]. This transform is used to retrieve the radial profile of the gas jet from the projection. The Abel inversion transform is defined as

$$n(r) - n_0 = \frac{1}{S} \int_r^\infty \frac{C(x)}{\pi \sqrt{x^2 - r^2}} \mathrm{d}x, \tag{7.7}$$

where n_0 is the ambient refractive index (assumed to be one), r the radial location in the jet, x the horizontal location in the projection and C the measured contrast. The Abel transform and its inversion are linked to the Radon transform, where the Radon transform does not have the axis symmetry requirement [58, 59]. Although the Radon transform is a bit overkill for this application (as it usually is applied to non-rotational

symmetric targets with a set of images acquired symmetrically around the target), it is directly supported in software packages such as Matlab [60] making it easier to implement. The inverse Radon transform has therefore been utilized instead. This approach led to the reconstruction of the refractive index profile, as depicted in Figure 7.5. With a backing pressure of 4 bar, the peak refractive index retrieved in the jet is 1.00028, which corresponds to approximately 1.07 bar, using the Gladstone-Dale relation (see Equation 7.1). The pressure can be converted to an atomic density by using the ideal gas law (assuming room temperature) and the molar mass of argon. This methodology has been repeated for backing pressures from 2 up to 10 bar with steps of 1 bar.

The pressure profile of the retrieved gas jet, as determined from measurements, show that the peak pressure decreases exponentially from the point of the gas jet nozzle. This decay in pressure is more pronounced near the gas catcher, which could be attributed to the enhanced pumping efficiency of the gas catcher. Further, a linear correlation is observed between the peak pressure within the gas jet and the backing pressure.

These measurements have been performed without higher harmonics being generated, i.e. no plasma is present. Estimating the atomic density within the interaction medium would ideally be matched with the infrared laser field. We repeat the measurements with the plasma and use the brightness of the plasma to define an interaction volume. The width of the volume is defined by $1/e^2$ width relative to the peak plasma brightness. The perimeter of the plasma is then overlapped onto the schlieren images to indicate the region where the plasma is present, as shown in Fig. 7.7 and marked by the solid white lines.

The total amount of argon atoms within the retrieved volume per backing pressure increases linearly with the backing pressure. The plasma is located in the center of the gas jet both in x and z, as can be seen in Fig. 7.7. The generated higher harmonics in the gas jet propagate downstream to the EUV spectrometer, after removing the drive laser through grazing incidence plates and aluminum foils, as shown in Fig. 7.2. The intensity of most higher harmonics between 18 and 28 nanometer continue to increase with atomic density, with the exception of the higher harmonic orders 41 (λ =25 nm),

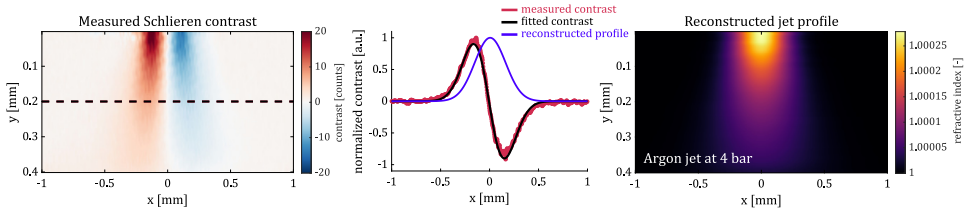

Figure 7.5: **Left:** A knife is placed parallel to the gas jet to visualize the gradient perpendicular to the knife, i.e. the gradient proportional to the refractive index of an argon gas jet in the x-direction. **Center:** The derivative of a Gaussian function is fitted for each pixel row. We show an example at y = 0.2 mm (dashed black line in left image) in the center image where the measured contrast (shown in red) is fitted (black solid line). Using the retrieved parameters a Gaussian profile can be reconstructed as indicated by the purple line. **Right:** This process is repeated for the entire gas jet length. After an inverse Radon transform combined with the sensitivity of the schlieren system, the refractive index of the gas jet is reconstructed.

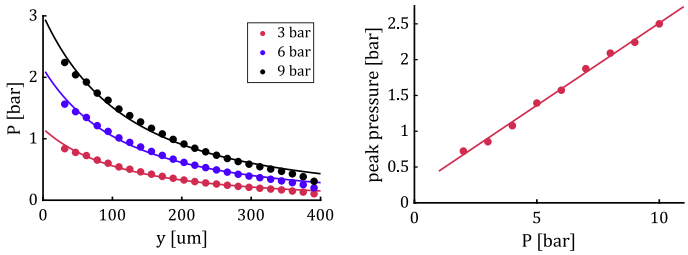

Figure 7.6: The peak pressure in the retrieved gas jet pressure profile drops off exponentially starting from the gas jet nozzle at y = 0. A slightly stronger drop off is observed closer to gas catcher, possibly due to the gas catcher which is attached to a vacuum pump. The maximum peak pressure within the entire gas jet, i.e. closest to the nozzle at y = 0, increases linearly with the backing pressure behind the nozzle.

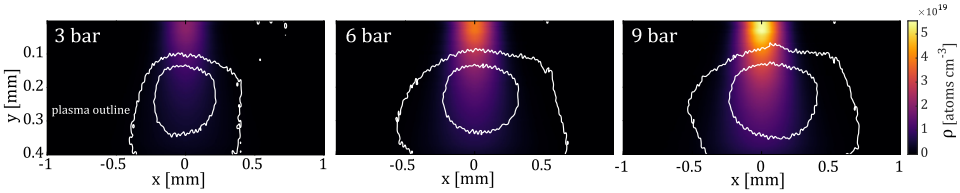

Figure 7.7: Reconstructed density profiles in atoms per cm^3 of an argon gas jet with a backing pressure of 3, 6 and 9 bar. For reference purposes, using the ideal gas law, 1 bar argon at room temperature has a density of $2.47 \cdot 10^{19}$ atoms per cm^3. The white outlines represents the size of the observed plasma at a given backing pressure when the gas jet is exposed to the fundamental drive laser[2]. The center white line represents the half of the observed peak plasma brightness (FWHM) and the second line refers to the $1/e^2$ value of the peak brightness.

43 (λ =24 nm) and 51 (λ =20 nm) which seem to saturate after approximately $4.5 \cdot 10^{14}$ atoms within the defined plasma volume.

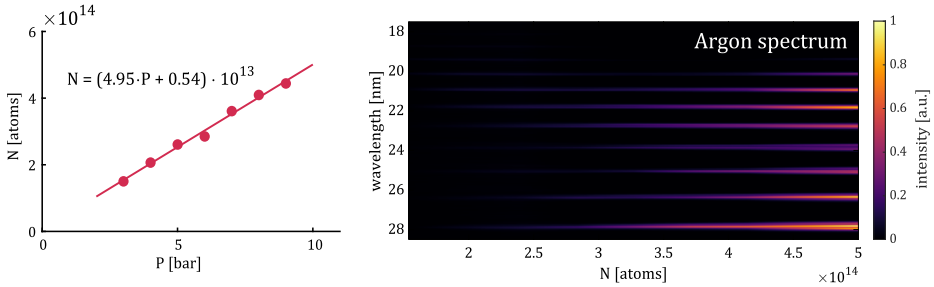

Figure 7.8: **Left:** The number of atoms present in the plasma volume grows linearly with the backing pressure. **Right:** The generated higher harmonics in the plasma propagate towards an EUV spectrometer placed downstream. A spectrum is acquired for wavelengths between 18 and 28 nanometer (equal to harmonic orders 37 and 55) for each backing pressure. Using the schlieren methodology, the intensity per harmonic order is compared to the number of atoms or gas density within the gas jet rather than the backing pressure giving a better representation of the source dynamics.

7.5. CONCLUSION

A compact metrology tool, based on schlieren imaging, has been implemented for quantitative retrieval of atomic density profiles in gas jet-based high harmonic generation (HHG) sources. Schlieren imaging offers a simplified approach compared to vibration-sensitive methods like interferometry and can serve as a suitable standardized tool for HHG sources and enables a fair comparison between different HHG sources. This allows for a comprehensive comparison and optimization of HHG light sources, as it directly retrieves the atomic density within the interaction media used for high harmonic generation.

Various gas jet profiles with different backing pressures were retrieved through a double-pass schlieren system with a single spherical mirror with a focal length of 250 mm. The mirror has been illuminated with a 625 nm LED light source, acting as a point source, of which an image was formed outside the vacuum chamber where a knife edge is placed to create a contrast. The schlieren image of the gas jet was observed with a CCD camera.

As the schlieren methodology by itself is not a quantitative approach, therfore some calibration is required. This has been achieved by introducing a known gradient through the use of a weak lens to associate the measured gray values to angular deviations due to refraction by a schlieren object. A deflection angle can be resolved within ± 2.1 mrad with a resolution of 16.5 µrad. After a Radon inversion (or Abel inversion), the jet profile can be retrieved in terms of the refractive index and therefore pressure or atomic density using the Gladstone-Dale relation.

The nozzle in the vacuum system was fed by backing pressures ranging between 2 and 10 bar, where a linear relationship between the peak pressure within the gas jet and its backing pressure were observed. Furthermore, an exponential decay in the peak pressure in the gas jet is observed starting from the nozzle. A steeper drop off is observed as the flow approaches a vacuum-pumped gas catcher. This demonstrates the influence of the nozzle and the vacuum system on the shape and behavior of the gas jet and thus shows that comparing gas jet based sources can be challenging without retrieving the atomic density profile of the gas jet.

The brightness of the plasma produced when exposing the gas jet to the high-power drive laser can serve as a basis for estimating the volume of the medium used in the high harmonic generation process. With the obtained density measurements and volume, the number of atoms present within the interaction volume of the laser field and the medium can be estimated.

BIBLIOGRAPHY

1. Loetgering, L., Witte, S. & Rothhardt, J. Advances in laboratory-scale ptychography using high harmonic sources. *Optics Express* **30,** 4133–4164 (2022).
2. Boutu, W., Ducousso, M., Hergott, J.-F. & Merdji, H. Overview on HHG high-flux sources. *Optical technologies for extreme-ultraviolet and soft X-ray coherent sources,* 63–78 (2015).
3. Strickland, D. & Mourou, G. Compression of amplified chirped optical pulses. *Optics communications* **55,** 447–449 (1985).
4. Boullet, J. *et al.* High-order harmonic generation at a megahertz-level repetition rate directly driven by an ytterbium-doped-fiber chirped-pulse amplification system. *Optics letters* **34,** 1489–1491 (2009).
5. Feehan, J. S. *et al.* Efficient high-harmonic generation from a stable and compact ultrafast Yb-fiber laser producing 100 μJ, 350 fs pulses based on bendable photonic crystal fiber. *Applied Physics B* **123,** 1–12 (2017).
6. Gebhardt, M. *et al. Soft x-ray high order harmonic generation driven by high repetition rate ultrafast thulium-doped fiber lasers* in *Fiber Lasers XVII: Technology and Systems* **11260** (2020), 84–89.
7. Tschernajew, M. *et al. High repetition rate high harmonic generation with ultra-high photon flux* in *Laser Applications Conference* (2020), JTh2A–21.
8. Kirsche, A. *et al.* Continuously tunable high photon flux high harmonic source. *Optics Express* **31,** 2744–2753 (2023).
9. Tanksalvala, M. *et al.* Nondestructive, high-resolution, chemically specific 3D nanostructure characterization using phase-sensitive EUV imaging reflectometry. *Science Advances* **7,** eabd9667 (2021).
10. Porter, C. L. *et al.* General-purpose, wide field-of-view reflection imaging with a tabletop 13 nm light source. *Optica* **4,** 1552–1557 (2017).
11. Eschen, W. *et al.* Material-specific high-resolution table-top extreme ultraviolet microscopy. *Light: Science & Applications* **11,** 117 (2022).
12. Luu, T. T. *et al.* Extreme ultraviolet high-harmonic spectroscopy of solids. *Nature* **521,** 498–502 (2015).
13. Porter, C. *et al. Soft x-ray: novel metrology for 3D profilometry and device pitch overlay* in *Metrology, Inspection, and Process Control XXXVII* **12496** (2023), 412–420.
14. Lin, N., Den Boef, A. J., Roobol, S. B., Mathijssen, S. G. J. & Geypen, N. *HHG source, inspection apparatus and method for performing a measurement* US Patent 10,816,906. Oct. 2020.

15. Weissenbilder, R. *et al.* How to optimize high-order harmonic generation in gases. *Nature Reviews Physics* **4,** 713–722 (2022).

16. Krause, J. L., Schafer, K. J. & Kulander, K. C. High-order harmonic generation from atoms and ions in the high intensity regime. *Physical Review Letters* **68,** 3535 (1992).

17. Corkum, P. B. Plasma perspective on strong field multiphoton ionization. *Physical review letters* **71,** 1994 (1993).

18. Altucci, C. *et al.* Influence of atomic density in high-order harmonic generation. *JOSA B* **13,** 148–156 (1996).

19. Grant-Jacob, J. *et al.* Gas jet structure influence on high harmonic generation. *Optics Express* **19,** 9801–9806 (2011).

20. L'Huillier, A., Schafer, K. & Kulander, K. Higher-order harmonic generation in xenon at 1064 nm: The role of phase matching. *Physical review letters* **66,** 2200 (1991).

21. Popmintchev, T., Chen, M.-C., Arpin, P., Murnane, M. M. & Kapteyn, H. C. The attosecond nonlinear optics of bright coherent X-ray generation. *Nature Photonics* **4,** 822–832 (2010).

22. Salieres, P., L'Huillier, A. & Lewenstein, M. Coherence control of high-order harmonics. *Physical Review Letters* **74,** 3776 (1995).

23. Gaudiosi, D. M. *et al.* High-order harmonic generation from ions in a capillary discharge. *Physical review letters* **96,** 203001 (2006).

24. Couch, D. E. *et al.* Ultrafast 1 MHz vacuum-ultraviolet source via highly cascaded harmonic generation in negative-curvature hollow-core fibers. *Optica* **7,** 832–837 (2020).

25. Reagan, B. *et al.* Enhanced high-order harmonic generation from Xe, Kr, and Ar in a capillary discharge. *Physical Review A* **76,** 013816 (2007).

26. Chen, M.-C. *et al.* Spatially coherent, phase matched, high-order harmonic EUV beams at 50 kHz. *Opt. Express* **17,** 17376–17383. https://opg.optica.org/oe/abstract.cfm?URI=oe-17-20-17376 (Sept. 2009).

27. Vodungbo, B. *et al.* Polarization control of high order harmonics in the EUV photon energy range. *Opt. Express* **19,** 4346–4356. https://opg.optica.org/oe/abstract.cfm?URI=oe-19-5-4346 (Feb. 2011).

28. Paul, P.-M. *et al.* Observation of a train of attosecond pulses from high harmonic generation. *Science* **292,** 1689–1692 (2001).

29. Klas, R., Eschen, W., Kirsche, A., Rothhardt, J. & Limpert, J. Generation of coherent broadband high photon flux continua in the XUV with a sub-two-cycle fiber laser. *Optics Express* **28,** 6188–6196 (2020).

30. Burnett, N., Baldis, H., Richardson, M. & Enright, G. Harmonic generation in CO2 laser target interaction. *Applied Physics Letters* **31,** 172–174 (1977).

31. Ghimire, S. & Reis, D. A. High-harmonic generation from solids. *Nature physics* **15,** 10–16 (2019).

32. Luu, T. T. *et al.* Extreme–ultraviolet high–harmonic generation in liquids. *Nature communications* **9,** 3723 (2018).

33. Karatodorov, S. *et al.* Multi-pass probing for high-sensitivity tomographic interferometry. *Scientific Reports* **11,** 15072 (2021).

34. Malka, V. *et al.* Characterization of neutral density profile in a wide range of pressure of cylindrical pulsed gas jets. *Review of Scientific Instruments* **71,** 2329–2333 (2000).

35. Hansen, A. *et al.* Supersonic gas-jet characterization with interferometry and Thomson scattering on the OMEGA Laser System. *Review of Scientific Instruments* **89** (2018).

36. Avtaeva, S. V., Gubin, K. V., Trunov, V. I. & Tuev, P. V. Algorithm for supersonic gas jet density profile retrieval from interferometric measurement. *JOSA A* **36,** 910–917 (2019).

37. Couperus, J. P. *et al.* Tomographic characterisation of gas-jet targets for laser wakefield acceleration. *Nuclear Instruments and Methods in Physics Research Section A: Accelerators, Spectrometers, Detectors and Associated Equipment* **830,** 504–509 (2016).

38. Comby, A. *et al.* Absolute gas density profiling in high-order harmonic generation. *Optics express* **26,** 6001–6009 (2018).

39. Settles, G., Brandt, A. & Miller, J. *Full-scale schlieren imaging of shock waves for aviation security research* in (Sept. 1998).

40. Settles, G. S. & Hargather, M. J. A review of recent developments in schlieren and shadowgraph techniques. *Measurement Science and Technology* **28,** 042001. https://dx.doi.org/10.1088/1361-6501/aa5748 (Feb. 2017).

41. JH Gladstone, T. D. Researches on the refraction, dispersion, and sensitiveness of liquids (1863).

42. Ben-Dor, G. & Whitten, B. T. *Interferometric techniques and data evaluation methods for the UTIAS 10cmx18cm hypervelocity shock tube* tech. rep. (Citeseer, 1979).

43. Settles, G. Schlieren and Shadowgraph Techniques: Visualizing Phenomena in Transparent Media (Springer-Verlag, Berlin, Germany, 2001). *European Journal of Mechanics - B/Fluids* **21,** 493 (Dec. 2002).

44. Jonassen, D. R., Settles, G. S. & Tronosky, M. D. Schlieren "PIV" for turbulent flows. *Optics and Lasers in Engineering* **44,** 190–207 (2006).

45. Settles, G. S. & Hargather, M. J. A review of recent developments in schlieren and shadowgraph techniques. *Measurement Science and Technology* **28,** 042001 (2017).

46. Raffel, M. Background-oriented schlieren (BOS) techniques. *Experiments in Fluids* **56,** 1–17 (2015).

47. Ishino, Y. *et al.* 3D-CT (computer tomography) measurement of an instantaneous density distribution of turbulent flames with a multi-directional quantitative schlieren camera (reconstructions of high-speed premixed burner flames with different flow velocities). *Flow, Turbulence and Combustion* **96,** 819–835 (2016).

48. Barnes, N. F. & Bellinger, S. L. Schlieren and Shadowgraph Equipment for Air Flow Analysis. *J. Opt. Soc. Am.* **35,** 497–509. https://opg.optica.org/abstract.cfm?URI=josa-35-8-497 (Aug. 1945).

49. Kook, S., Le, M. K., Padala, S. & Hawkes, E. R. *Z-type schlieren setup and its application to high-speed imaging of gasoline sprays* tech. rep. (SAE Technical Paper, 2011).

50. Boselli, M. *et al.* Schlieren high-speed imaging of a nanosecond pulsed atmospheric pressure non-equilibrium plasma jet. *Plasma chemistry and plasma processing* **34,** 853–869 (2014).

51. Bradley, J. W. *et al.* Schlieren photography of the outflow from a plasma jet. *IEEE Transactions on Plasma Science* **39,** 2312–2313 (2011).

52. Gerold, J., Vogl, P. & Pfitzner, M. New correlation of subsonic, supersonic and cryo gas jets validated by highly accurate schlieren measurements. *Experiments in fluids* **54,** 1–15 (2013).

53. Hargather, M. J. & Settles, G. S. A comparison of three quantitative schlieren techniques. *Optics and Lasers in Engineering* **50.** Advances in Flow Visualization, 8–17. ISSN: 0143-8166. https://www.sciencedirect.com/science/article/pii/S014381661100159X (2012).

54. Kogelschatz, U. & Schneider, W. Quantitative schlieren techniques applied to high current arc investigations. *Applied Optics* **11,** 1822–1832 (1972).

55. Agrawal, A. K., Albers, B. W. & Griffin, D. W. Abel inversion of deflectometric measurements in dynamic flows. *Applied Optics* **38,** 3394–3398 (1999).

56. Xiong, Y., Kaufmann, T. & Noiray, N. Towards robust BOS measurements for axisymmetric flows. *Experiments in Fluids* **61,** 178 (2020).

57. Traldi, E. *et al.* Schlieren imaging: a powerful tool for atmospheric plasma diagnostic. *EPJ Techniques and Instrumentation* **5,** 1–23 (2018).

58. Tan, D. J., Edgington-Mitchell, D. & Honnery, D. Measurement of density in axisymmetric jets using a novel background-oriented schlieren (BOS) technique. *Experiments in Fluids* **56,** 1–11 (2015).

59. Kak, A. C. & Slaney, M. *Principles of computerized tomographic imaging* (SIAM, 2001).

60. Matlab. *Radon transform MathWorks* https://nl.mathworks.com/help/images/ref/radon.html [Accessed: (02-01-2024)]. Matlab Mathworks.

8

Conclusion

8.1. CONCLUSION

A major part of the work in this thesis is described in Chapter 4 and concerns the design and implementation of the EUV lensless imaging beamline. The EUV beamline consists of a compact High Harmonic Generation (HHG) source powered by a commercial 100 W Ytterbium-doped fiber laser, producing pulses initially at 300 fs with an average power of 100 Watt. With a Krypton-filled hollow core fiber and chirped mirrors, these pulses are compressed to roughly 30 fs. The compression is needed for better phase matching conditions and to minimize ionization effects (like absorption) for a better conversion efficiency from IR to EUV light. Higher harmonics can be generated with Argon or Neon at around 18 nm and 13.5 nanometers, respectively.

After filtering out the IR beam while preserving the higher harmonics, a set of multi-layer mirrors isolate a narrow bandwidth of the spectrum around 18 nanometers (for the case of Argon). A Ruthenium-coated ellipsoidal mirror focuses the selected harmonic onto the sample after an alignment procedure using a sensitivity matrix approach described in Chapter 4.5. The sample is situated in an assembly of slip-stick piezo stages for probe scanning and sample alignment, ensuring high precision and stability. After the probe interacts with the sample, the field can freely propagate towards the EUV-sensitive camera.

In Chapter 5, we have demonstrated a ptychography approach with the EUV beamline using an automatic-differentiation (AD) framework with TensorFlow for reflective EUV diffractive imaging aimed towards semiconductor metrology. A patterned region of roughly 100 µm by 100 µm on a silicon substrate with gold structures has been illuminated with a probe containing two harmonics of 17.30 nm and 17.93 nm. In some parts of the region, 50 nm wide lines are observable and well-aligned compared to an acquired SEM image. Considering an imaging NA of 0.17 at 18 nm wavelength, 50 nanometers is close to the diffraction limit. A reconstructed structure height of the patterned Au structures of 23.6 ± 0.62 nm agrees well with the 20 nm nominal design height and the height retrieved from an atomic force microscope (AFM) measurement of 22.8 ± 1.45 nm.

The ptychography signal processing platform, called PtychoFlow, can incorporate multiple probe modes when encountering reduced spatial coherence. This is usually the case in high-harmonic generated EUV sources due to instabilities like beam pointing. Ptychoflow can simultaneously optimize for multiple experimental parameters, such as wavelength, propagation distance, scanning positions and source intensity instabilities (as shown in Chapter 6), making the framework adaptable in case of poor calibration. TensorFlow allows for GPU-accelerated optimizers to be utilized for improved performance compared to other open-source ptychography approaches.

Careful tuning of the hyperparameters, such as the learning rates of the probe, object or regularization, is required. This can be a rather time-consuming iterative process when reconstructing a new data set with an uncalibrated illumination system (i.e. propagation distance, wavelength, probe size or wavefront). Fortunately, we have to do this only once in industrial applications where initial conditions are better calibrated or the samples are somewhat similar.

Although modern AFM's can reach sub-nanometer resolution, in some cases EUV ptychography can be a better metrology approach than an AFM. Relatively large field of views (of about 100 microns) can be covered in a shorter measurement period with a comparable spatial resolution of an AFM, as shown in Chapter 5. However, more time has to be spent on the reconstruction of the sample when using ptychography adding computational overhead.

Implementing EUV ptychography in a **high-volume** metrology tool seems unlikely due to the scanning nature of ptychography. However, it might be a suitable candidate to complement other EUV metrology applications such as EUV scatterometry. A well-defined illumination field in scatterometry is necessary, which can be challenging to retrieve in the EUV regime. Applying ptychography on a known, well-defined calibration target allows the reconstruction of a complex-valued probe and the associated propagation distance and wavelength, which can be used as an input for scatterometry. In semiconductor applications, the intended "optimal" shape any patterned structure in e.g. a photo-resist layer for lithography is well known. This information can be used as a-priori knowledge for the structure that is subject to its ptychographic analysis. When combined with the above calibration step for system parameters, the throughput time of a ptychographic analysis can be significantly reduced.

Additionally, the reconstructed complex-valued field of the probe enables metrology of the illumination optic, as demonstrated in Chapter 5. By back-propagating the probe field to the pupil plane where it originates from, we identified significant defects in the ellipsoidal mirror, particularly in mid-spatial frequencies. Traditionally, this type of analysis would require removing the optic from the system for surface metrology, such as interferometry. However, ptychography allows for inline metrology within the tool itself, possibly even further simplified by using a well-calibrated sample.

8.2. FUTURE WORK

When performing ptychography in a reflection geometry, one needs to correct for the conical distortion in the diffraction patterns using Tilted Plane Correction (TPC). Adding this step directly into the AD framework, like aPIE [1], could allow for optimization of the angle of incidence (and other two rotation axes of the sample). Currently, this is done manually with prior knowledge of the sample. For example, when a grating or similar target is illuminated in a scan, we can manually tune the angle parameters until a 'straight' pattern is observed. Implementing it directly into the AD framework could allow for on-the-fly tilt correction and relieve calibration efforts.

Adding more spatial frequencies to the probe could help for better convergence and higher resolution reconstruction [2]. The defects in the ellipsoidal mirror already add quite some unintentional structure to the probe but come at the cost of an enlarged probe. If the mirror gets replaced by an optical system with lower defects, one could consider adding spatial frequencies to the probe with a transmission phase mask close to the sample. Alternatively, the ellipsoidal mirror could be replaced with custom diffractive optics or a meta lens [3] to illuminate the sample with a designed structured probe.

So far, we only assumed a 2D case with a thin single-layer sample relative to the wave-

length. When illuminating thicker samples, where the thin sample assumption no longer holds, it gets more challenging to perform ptychography. A multi-slice approach, like 3PIE [4–6], or a full 3D forward model in the ptychography loop could be implemented, but this would require more advanced scans than used in this thesis, like adding sample rotation or sweeping a range of angles of incidence[7, 8].

Some hardware improvements of the EUV beamline have already been suggested in Section 4.6 but are worth mentioning again. The current method of compressing 300 fs drive laser pulses to 30 fs using a hollow core fiber (HCF) and chirped mirrors are effective but relatively lossy (30 to 40 percent) and challenging to optimize, especially at full power due to the thermal load and self-focusing effects. Alternative techniques like multi-pass gas cell compression or loose focusing in low-pressure gas merit exploration. Additionally, incorporating motorized mirrors for more controlled fiber coupling and addressing beam stability post-compression are necessary improvements. The long-term stability, repeatability, and reliability of the IR system, and thus the EUV system, must be improved to allow for long-term experiments and to converge to a matured low-volume metrology tool.

Along with long-term experiments comes the control of contamination in the vacuum system due to hydrocarbon cracking when exposed to EUV light. Methods like bake-out steps, using cryogenic 'cold fingers', and potentially plasma cleaners could reduce the level of hydrocarbons.

Replacing the last mirror before the HHG chamber with an annular mirror could increase EUV throughput as it makes the IR removal unit obsolete which costs about half of the EUV power. This method also offers benefits in terms of polarization control, allowing for arbitrary polarization of the drive laser and EUV beam.

The gas jet nozzle assembly should be upgraded with a closed-loop piezo stage assembly for improved repeatability. The gas catcher should either be added to the assembly or have a dedicated control system to minimize the gas load in the HHG chamber.

The 5DOF sample stage assembly could be improved by adding two more manually or motorized controlled stages in parallel to the optical table. This would allow for precise placement of the 5DOF assembly to the focus of the EUV beam. Minor errors can be compensated with the piezo-driven stages of the 5DOF assembly, but significant errors require external movement.

Recently, CMOS technology has become available for the EUV regime [9], which employs significantly higher read-out rates (up to 300 MHz and 75 frames per second for CMOS cameras compared to 4 MHz and 0.1-1 frames per second for CCDs) where a mechanical shutter is not necessarily required anymore. It additionally allows for faster and better high-dynamic range measurements due to the quick read-out rate and reduced blooming/bleeding effects due to saturation compared to CCD cameras [10].

BIBLIOGRAPHY

1. De Beurs, A. *et al.* aPIE: an angle calibration algorithm for reflection ptychography. *Optics Letters* **47,** 1949–1952 (2022).
2. Odstrčil, M., Lebugle, M., Guizar-Sicairos, M., David, C. & Holler, M. Towards optimized illumination for high-resolution ptychography. *Optics express* **27,** 14981–14997 (2019).
3. Ossiander, M. *et al.* Extreme ultraviolet metalens by vacuum guiding. *Science* **380,** 59–63 (2023).
4. Maiden, A. M., Humphry, M. J. & Rodenburg, J. M. Ptychographic transmission microscopy in three dimensions using a multi-slice approach. *JOSA A* **29,** 1606–1614 (2012).
5. Shimomura, K., Suzuki, A., Hirose, M. & Takahashi, Y. Precession x-ray ptychography with multislice approach. *Physical Review B* **91,** 214114 (2015).
6. Suzuki, A. *et al.* High-resolution multislice x-ray ptychography of extended thick objects. *Physical review letters* **112,** 053903 (2014).
7. Holler, M. *et al.* High-resolution non-destructive three-dimensional imaging of integrated circuits. *Nature* **543,** 402–406 (2017).
8. Holler, M. *et al.* Three-dimensional imaging of integrated circuits with macro-to nanoscale zoom. *Nature Electronics* **2,** 464–470 (2019).
9. Instruments, O. *Oxford Instruments Andor Marana-X sCMOS* https://andor.oxinst.com/products/high-energy-detection/marana-x-scmos [Accessed: (02-01-2024)]. Oxford Instruments Andor.
10. Eschen, W. *et al.* High-speed and wide-field nanoscale table-top ptychographic EUV imaging and beam characterization with a sCMOS detector. *Optics Express* **31,** 14212–14224 (2023).

ACKNOWLEDGEMENTS

Just like everything, my PhD journey eventually had to come to an end. The project resulted in a newly build EUV beamline and eventually this dissertation as an outcome. I most definitely did not achieve this all by myself as quite some people where there to help me in many ways for which I am gratefull for. First of all I would like to start with my promotor **Wim Coene**. Wim, I am very thankful for the opportunity, the support, patience and trust you have put in not just me but the entire "LINX team" in Delft. I have thoroughly enjoyed your style of leadership & management and of course your stories about your birding adventures accompanied with beautiful photos. Fortunately, there will be many more opportunities to see your new photos at my next opportunity in Veldhoven! I also want to thank **Paul Urbach** to introduce me to the LINX project when I was still a master student working on my MEP with Jeff in the Optics Research Group and of course for your input and review of my work during the project.

Secondly, I want to thank **Yifeng Shao**. As I have stated before in this thesis, eventually hardware had to meet with software! Without your dedication to your beloved PtychoFlow package, the EUV and visible light hardware would have just generated some nice diffraction images! I enjoyed our teamwork, the drinks & dinners, traveling to conferences, discussions, and your obsession with your cats. I will even miss the occasional messages at 2 AM in the early morning saying *'Are you using the GPU??'*. I wish you all the best with your endeavors with AIMS and PtychoFlow!

Of course, I would like to thank **Roland Horsten**. I'm really glad to have had you as a technician in our project. You needed few words to understand want I needed (and I hope vice versa). I think we can be happy with what we have achieved. Working on such a project comes with significant challenges and risks, particularly on the day when the drive laser completely obliterated the gas jet nozzle and some optics, contaminating the vacuum vessel, which was a major setback for me. But your positive mindset, can-do mentality, and support helped me a lot through those moments. Besides the technical stuff, also the ability of you and Thim to bring people together and take a break should not be underestimated! Besides their technical support, technicians are pretty much the glue (or the grease on the pizza box ;-)) of the research group.

Sander Senhorst, you joined the team a bit later in the LINX project but quickly showed that you are a great PhD candidate capable of continuing the project both on the hardware and the software fronts! I wish you all the best and hope you can generate interesting results to demonstrate the issues associated with 3D problems with EUV light and of course solve them!

I also would like to thank **Christina Porter**. I do not think I could have asked for a more appropriate external contact (or "third supervisor") with your knowledge and experience

on EUV ptychography and HHG sources! Your PhD work resulted into an inspiration of this thesis and resulting beamline, thank you! The weekly meetings we have had in the last couple of years during my PhD were incredibly helpful. You've opened doors within ASML during the project, provided resources, and gave me the confidence to take certain steps. Excited to continue working together!

We had quite a few partners within the LINX project with whom we worked together extensively. **Jacob Seifert** and **Allard Mosk** for their work and collaboration on PtychoFlow. I would like to thank the people at ARCNL/VU Amsterdam, including, but not exclusively, **Stefan Witte**, **Antonios Pelekandis**, and **Mengqui Du**. From the University of Twente, I would like to thank **Bert Bastiaens** and **Klaus Boller** for their help during the starting period of LINX when the EUV source was delivered and their work on the EUV beam analyzer. Thank you to the colleagues at TU Eindhoven, **Martijn Beurden**, **Stefan Eijsvogel**, and **Roeland Dilz** for their contributions.

Then I would like to thank my colleagues who also directly contributed to my work reported in this thesis. I want to thank **Sergei Pyatchenkov** for his work on the LabVIEW control program driving the stages in the vacuum vessel. **Thim Zuidwijk**, for helping me with vacuum equipment, optics and your keen eye on safety. **Thomas Scholte**, your addition to the research group as a whole is very valuable, especially with your 3D printing skills and general knowledge! I would also like to thank **Wouter Erades** and **Adrian Gutierrez Gonzalez** and their contribution during their bachelor internship and master end project respectively.

My project required the support and contribution from technicians outside the borders of the Optics Research Group. **Youp van Goozen** and **Ruud van Tol** contributed and helped me out a lot with the design of the EUV beamline, especially with their focus on high-end vacuum systems, for which I am very thankful. **Johan van der Cingel** always helped me out by quickly loaning vacuum equipment or thinking about solutions if I bumped into a vacuum-related issue. If you need help with some smaller metalwork, follow the loud hard rock music in the C-wing and you will find **Ron Hoogerheide**. I would also like to thank our partners at TNO, in particular, **Ruud Schmidt** and **Andrea Scardaoni**, for their support by fabrication of samples, finding more in-kind support during the project or squeeze in some extra time to fabricate a new sample.

And of course, I would like to thank my fellow PhD candidates and postdocs in the Optics Research Group. Let's start with my office mates **Thomas van der Sijs**, **Dmytro Kolenkov**, and **Thomas Kotte** for the never-ending inside jokes. Dmytro, unfortunately, I do want to correct the claim to the ping-pong and basketball throne, it is mine! **Luuk Zonneveld**, **Alex Heemels** and **Thomas van der Sijs** for working together on the Optics Chapter Delft. A key part of an enjoyable PhD are the friday afternoon drinks, so keep them going **Luuk Zonneveld**, **Anubhav Paul** and **Bruno Lopez Rodriguez**! I would like to thank **Hui Wang**, **Sarika Soman**, **Zizheng Li**, **Jan de Graaff**, **Reint Koppert**, **Yanhui Ji**, **Dingding Ren**, **Naresh Sharma**, **Behnoosh Babaghorbani**, **Shrouk Eid Zaki Ahmed**, **Mischa Mykhaylov**, and **JP Narag** for the fun times! I also won't forget the PhDs and postdocs who already left the research group: **Jila Rafigdhoost**, **Po-Ju Chen**, **Peiwen Meng**, **Paolo Ansuinelli**, **Zheng Xi**, **Lauryna Šiaudinytė**, and **Xukang Wei**. Thanks again to all

my fellow PhDs and postdocs and good luck with your (academic) careers!

I also extend my thanks to the staff of the Optics Research Group: **Aurèle Adam** for his openness and enthusiasm, **Iman Esmaeil Zadeh** for his dedication (to science and Lord of the Rings), **Omar El Gawhary** and **Jian-Rong Gao** for their contagious excitement when telling stories, **Silvania Pereira** for her support and actively working on the PhD-in-4 issue, and **Chris Christie** for his support on the financial aspect. I especially want to express my gratitude to **Lidija Nikolic** for ensuring that everything runs smoothly, not just for me but for the entire group.

Behind the scenes, I also received full support. **My mother José**, **Michel**, **Nadia & Ghazi**, **Liset & Siem**, and **Björn**, thank you all for always believing in me from the start! Last but definitely not least, of course I am thankful for the incredible support from **Zhaoyang**! For motivating me when I wasn't very productive anymore. For dealing with me when I was lacking sleep and spare time or my grumpiness if things did not go the way I wanted. But also for celebrating with me during the successful moments!

Thank you all!

APPENDIX A

A.2. POISSON DISK SAMPLING

There are several scanning methodologies to choose from when planning a ptychography scan across an object of interest as discussed in Chapter 5. The examples given in Chapter 5 are grid scan, random sampling, Fermat spiral and Poisson disc sampling. For random sampling we consider a region R and we want to generate N points randomly within R, we can simply choose N random coordinates within the bounds of R. This process is straightforward and easy to implement but may result in non-uniform distributions with clusters of points or gaps between them due to the lack of constraints. This could be improved by defining a normal grid first and then perturb it which some random value. Although it does not suffer from the repeating patterns like a normal grid scan, it could still result in a non-uniform distribution.

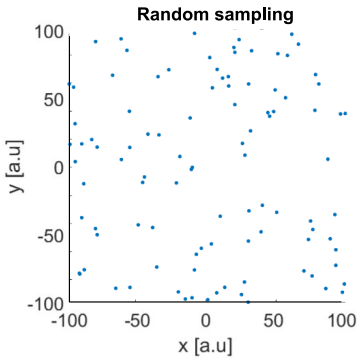

Figure A.1: Random sampling inside region R leads to non-uniform sampling when the number of samples are relatively low. A minimal overlap of neighbouring probes can not be guaranteed if this would be used as input for the scan positions of a probe in a ptychography experiment.

Poisson disk sampling, as shown in Fig. A.2, on the other hand, ensures a more uniform distribution by enforcing a minimum distance constraint between points. The algorithm iteratively places points in the region R, ensuring that each new point is at least a set distance away from all existing points. This constraint prevents clustering and results in a more even distribution of points across the space.

With this feature it is also possible to assign different distance constraints for certain regions and therefore sampling densities across the target. This could be interesting when scanning a large field of view, where densely patterned areas with small features could be sampled with a higher density while "empty" areas on the sample can be sampled with a low density limiting the total acquired frames during a scan.

A

In terms of computational complexity, random sampling is generally simpler and faster to implement since it involves generating points independently. Poisson disk sampling, in contrast, requires a little more computational overhead due to the iterative process of ensuring the minimum distance constraint. The extra overhead is however negligible as it only need to be performed once before a scan is preformed.

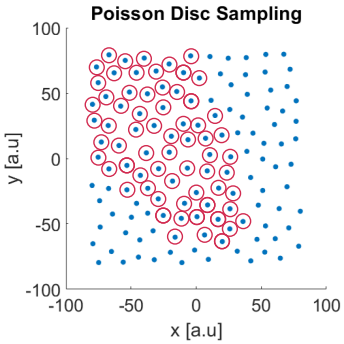

Figure A.2: Each point which is sampled with Poisson disk sampling is at least a set distance r away from all other points to avoid clustering. The radius in this case is demonstrated by the red ring around certain points.

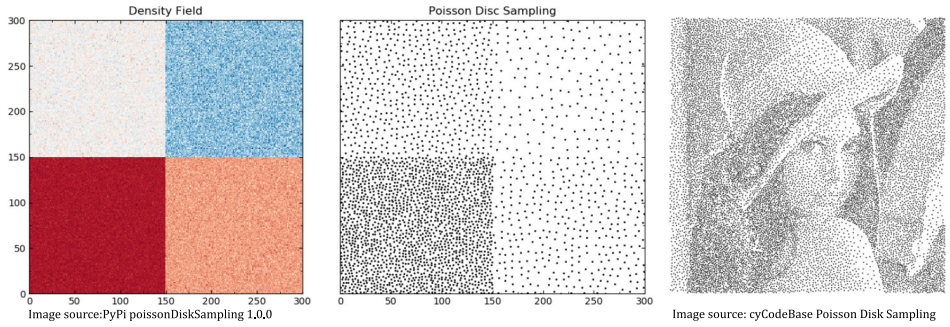

Figure A.3: Different sampling densities across a region R can be achieved by varying the minimum radius spatially. With prior knowledge of the sample some areas could be scanned with a higher density allowing for more overlap in ptychograpy. For example using the sample design as an input to generate a scanning grid, much like what has been done with a Lenna test image as shown in the image on the right. Left and middle image courtesy of *PyPi poissonDiskSample 1.0.0 library*. The image on the right is courtesy of *cyCodeBase*.

APPENDIX B

EUV BEAMLINE SYSTEM OVERVIEW

B.1.1. FIBER SYSTEM PERFORMANCE BEFORE COMPRESSION

Parameter	Nominal value	Comment
Center wavelength	1030 nm	
Pulse duration	350 fs to 5 ps	
Repetition rate	50 kHz - 19 MHz	Can be set to integer values of the oscillator 19 MHz
Average power	100 W	For repetition rate higher than 500 kHz
Pulse energy	< 200 uJ	for repetition rate below 500 kHz
Beam quality M2	<1.2	

B.1.2. FIBER SYSTEM PERFORMANCE AFTER COMPRESSION

Parameter	Nominal value	Comment
Center wavelength	1030 nm	
Pulse duration	30 fs	
Repetition rate	50 kHz - 19 MHz	Typically 660 kHz
Average power	< 68 W	Achieved at 600 kHz
Pulse energy	> 100 uJ	
Beam quality M2	<1.2	

B.1.3. EUV BEAMLINE THROUGHPUT AT 18 NANOMETER

Parameter	Nominal value	Comment
Est. photonflux at source @ 18 nanometer	10^{11} photons/s	Back-calculated to gas jet
Reflectivity Brewster windows	0.513	Coated with Nb2O5, SiO2
Transmission double stack aluminium filter	0.56	Taken from CXRO database
Reflectivity AlZr mirror NTT-AT	0.2	
Reflectivity Ru ellipsoidal mirror NTT-AT	0.82	
Reflectivity silicon substrate	9.50E-03	At a grazing AOI at 20 degrees
Reflectivity gold	0.42	At a grazing AOI at 20 degrees
Est. photoflux at sample	$4.71 \cdot 10^{9}$ photons/s	
Est. photoflux from pure silicon sample	$4.48 \cdot 10^{7}$ photons/s	
Est. photoflux from pure gold sample	$2 \cdot 10^{9}$ photons/s	

APPENDIX C

C.1. LOSSLESS EUV AND SXR PHOTONFLUX SENSING

Many optical metrology systems can be generalized into three basic modules: illumination, sample interaction, and detection. These types of metrology systems rely on the photon flux stability of the light source as it is not possible to differentiate photon flux changes in detected intensities due to the fact that another part of the sample is illuminated. Therefore, the photon flux illuminating the sample has to be monitored to normalize the measured intensities in the detector after interaction with the sample.

In most cases, this can be solved by picking off a small portion of the beam utilizing a beamsplitter or secondary reflections. This approach is quite viable and sufficient for situations where photons are abundant or where beamsplitters are relatively efficient. Unfortunately, the latter two requirements are often not met in short-wavelength systems such as table-top Extreme UV (EUV) light sources based on High Harmonic Generation (HHG). Even though these HHG systems have become more efficient over time [1, 2], the generated short-wavelength photons remain rather scarce and thus quite precious. In addition, beam splitters in this wavelength regime are relatively inefficient making them costly for typical low powered HHG beamlines. [3]

Here we describe a cheap and straightforward method based on ejected electrons from the photo-electric effect to sense the photon flux with components inherently found in most Extreme UV metrology systems based on High Harmonic Generation. Since this technique utilizes components that are already present within such a beamline, it does not result in any additional losses in the photon flux [4] unlike beamsplitters.

Our EUV/SXR metrology beamline contains application-specific optical elements like the IR removal mirrors or multi-layer mirrors. However, generic components can be found in similar beamlines such as the metallic transmission filters or focusing optics [5–9]. These objects enable us to measure the photon flux which impinges on the conductive surfaces of the object. The high-energy photons are energetic enough to release electrons from the surface through the photoelectric effect. These electrons will end up somewhere within the vacuum chamber and the majority will end up in a common electrical ground (like the electrically grounded wall of the vacuum chamber). Therefore, a photon-induced current can be measured on the conductive surface of the mirrors and filters which can be used as a reference in metrology experiments.

As this approach does not yield any spectral information, similar to a photodiode, the location of the sensing optical object would ideally be as close a possible to the target. The optimal location in our beamline would be the last optical element, i.e. the ellipsoidal mirror, as only a single harmonic hits this surface. All the light reflected from the mirror propagates towards the sample. However, in this paper, we demonstrate this

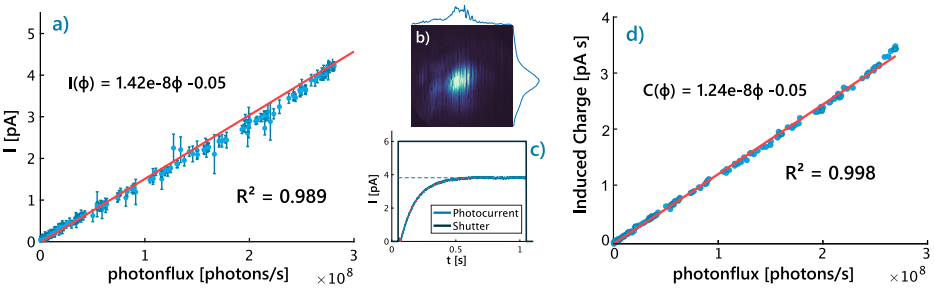

Figure C.1: A "steady-state current" is found by fitting an exponential function to an acquired signal during a complete exposure as indicated in **c)** and compared to the photon flux measured on the CCD in **b)**. Repeating this for a different photon flux, up to $3 \cdot 10^8$ photons per second, results in the linear relation between the photon current and photon flux as shown in **a)**. However, the output power of the source fluctuates during a measurement, making the steady state current an unreliable method to determine the photon flux. Integrating the current during the entire exposure, including the rise time of the detector, is able to compensate these effects as shown in **d)**.

method on a 200 nm thin aluminum transmission filter instead. Our beamline has a set of two metallic filters, which are needed to suppress the IR light sufficiently. For this demonstration, we add a third aluminum filter in between the mechanical shutter and the sample. In this way, we illuminate the filter with a single harmonic rather than with a broadband beam.

The aluminum filter is only 200 nm thick and thus delicate, making it hard to attach an electrical contact directly onto the foil. So instead, the foil is mounted on a steel ring and is sandwiched between two steel washers, on which we directly soldered an electrical contact with a bare wire, i.e. without shielding. An electrical resistance of 3.1 Ω was measured between the electrical contact and the foil mount. The photon current is amplified by a variable low-noise preamplifier, which output is sampled at 30 kHz by an Analog-to-Digital converter (ADC).

The metallic filter is exposed to a single harmonic with a center wavelength of 18 nanometer as soon as the mechanical shutter opens. It takes some time for the current in the foil to settle to a "steady-state current" $I_{\max}$ of 4.5 pA, see Fig. C.1c, with an average time constant τ of 144 ± 11 ms making it a rather slow sensor.

In order to calibrate the measured current to a photon flux, we use the reflection of a bare silicon sample, which is captured by the CCD placed at the end of the beamline, see Figure C.1b. After the exposure of one second, the integrated counts can be converted to a photon flux. This value is used as a reference to the measured current and is found to be $2.69 \cdot 10^8$ photons per second for 3.9 pA. Note that the captured image of the CCD is after reflection with a silicon sample, meaning that the actual flux hitting the foil is higher than measured with the CCD. The photon-induced current during the entire exposure is integrated, meaning we find a total build-up charge on the foil, which is a better representation of the total photon flux hitting the camera during an exposure.

By varying the photon flux of the EUV source we can fined a linear relation found be-

tween the build-up charge and the photon flux, see Fig. C.1d. This demonstrates that it could be used as an online photon flux monitoring tool.

This method is rather quick-and-dirty as an electrical wire without any shielding is used to connect the preamplifier and the sensor while measuring these small currents. This is never really a good idea as it can lead to parasitic signals from external sources. The mechanical shutter is driven by an electromagnetic coil to actuate the shutter blades. This coil induces a significant parasitic signal in the unprotected wire due to electromagnetic coupling. The inductive parasitic signal contributes 121 ± 8 ms to the total time constant of the sensor found in Fig. C.1c of 140 ms and therefore the main contributor to the long rise time of the sensor. These external signals can be reduced by replacing the bare wire with a shielded coaxial wire.

BIBLIOGRAPHY

1. Popmintchev, T., Chen, M.-C., Arpin, P., Murnane, M. M. & Kapteyn, H. C. The attosecond nonlinear optics of bright coherent X-ray generation. *Nature Photonics* **4.** https://doi.org/10.1038/nphoton.2010.256 (Dec. 2010).
2. Rothhardt, J., Tadesse, G. K., Eschen, W. & Limpert, J. Table-top nanoscale coherent imaging with XUV light. *Journal of Optics* **20,** 113001. https://doi.org/10.1088/2040-8986/aae2d8 (Oct. 2018).
3. Kishimoto, M. *et al.* Intensity correlation measurement system by picosecond single shot soft x-ray laser. *Review of Scientific Instruments* **81,** 013905. eprint: https://doi.org/10.1063/1.3280173. https://doi.org/10.1063/1.3280173 (2010).
4. Grilj, J., Sistrunk, E., Koch, M. & Gühr, M. *A beamline for time-resolved extreme ultraviolet and soft x-ray spectroscopy* 2013. arXiv: 1312.5399 [physics.atm-clus].
5. Ku, Y.-S. *et al.* EUV scatterometer with a high-harmonic-generation EUV source. *Opt. Express* **24,** 28014–28025. http://www.osapublishing.org/oe/abstract.cfm?URI=oe-24-24-28014 (Nov. 2016).
6. Porter, C. L. *et al.* General-purpose, wide field-of-view reflection imaging with a tabletop 13 nm light source. *Optica* **4,** 1552–1557. http://www.osapublishing.org/optica/abstract.cfm?URI=optica-4-12-1552 (Dec. 2017).
7. Wachulak, P., Bartnik, A., Jarocki, R. & Fiedorowicz, H. Characterization of multi-jet gas puff targets for high-order harmonic generation using EUV shadowgraphy. *Nuclear Instruments and Methods in Physics Research Section B: Beam Interactions with Materials and Atoms* **285,** 102–106. ISSN: 0168-583X. https://www.sciencedirect.com/science/article/pii/S0168583X12002649 (2012).
8. Tadesse, G. K. *et al.* High speed and high resolution table-top nanoscale imaging. *Opt. Lett.* **41,** 5170–5173. http://www.osapublishing.org/ol/abstract.cfm?URI=ol-41-22-5170 (Nov. 2016).
9. Jansen, G. S. M., Rudolf, D., Freisem, L., Eikema, K. S. E. & Witte, S. Spatially resolved Fourier transform spectroscopy in the extreme ultraviolet. *Optica* **3,** 1122–1125. http://www.osapublishing.org/optica/abstract.cfm?URI=optica-3-10-1122 (Oct. 2016).

APPENDIX D

D.1. LENSLESS IMAGING GALLERY WITH EXTREME UV LIGHT

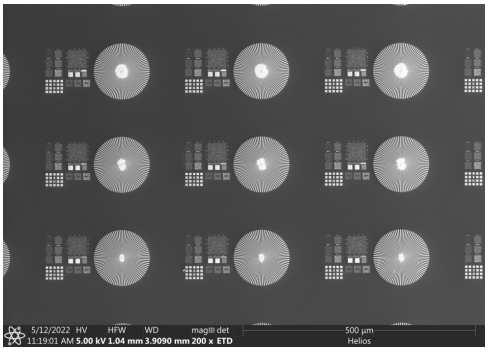

Figure D.1: A sample has been fabricated by TNO containing a variety of structures from a Siemens star, chirped gratings and Manhattan like structures. Several copies (10-by-10) have been made of the same sample with difference dosages during the e-beam lithography step.

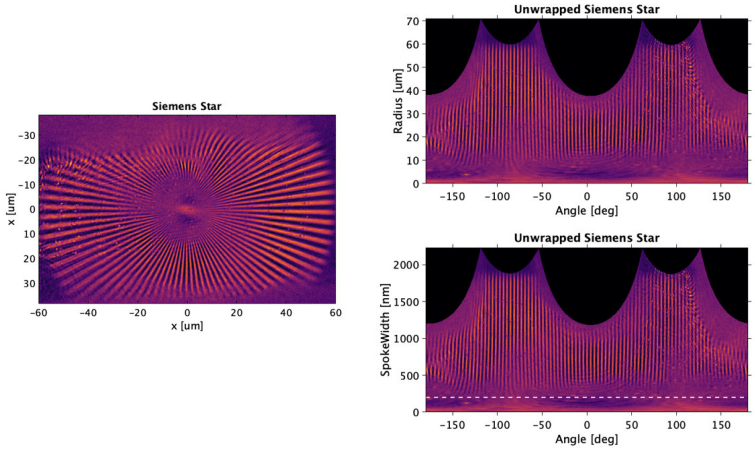

Figure D.2: A ptychography reconstruction of a golden Siemens star on a silicon substrate, measured at a 70-degree incidence angle and illuminated with 18 nm light. The right column shows the same reconstruction in polar coordinates, where the star's radius (top figure) is linked to spoke width (bottom figure), allowing for a quick assessment of spoke reconstruction quality along the radial direction.

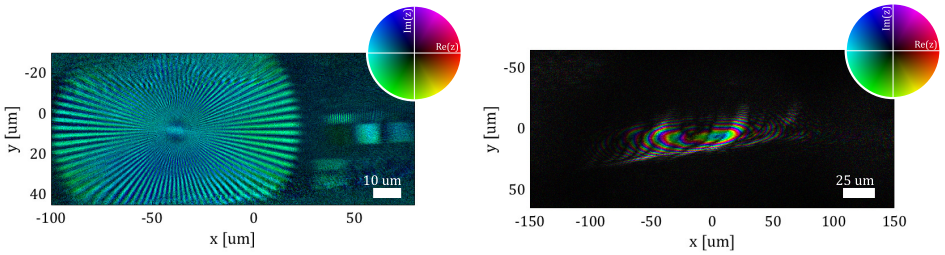

Figure D.3: A ptychography reconstruction of the same Siemens as shown in Fig. D.2, but from a different scan and in a complex representation where the brightness represents the amplitude and the hue represents the phase of the object. The associated reconstructed probe is shown on the right.

D

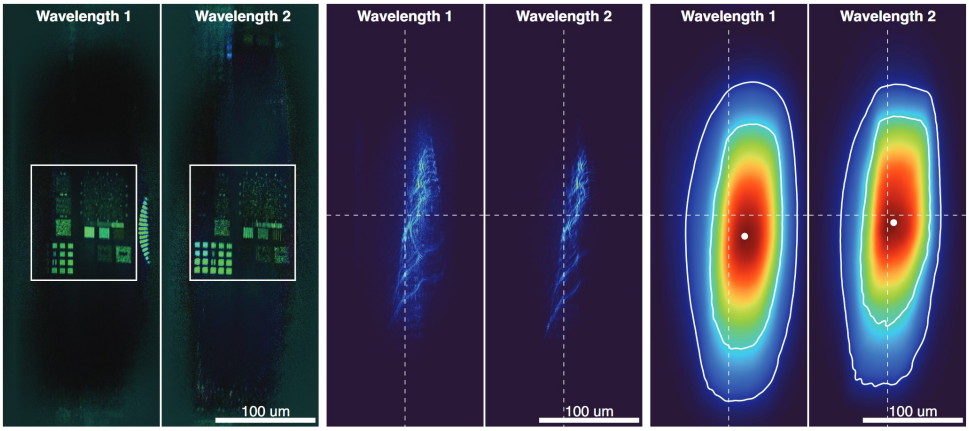

Figure D.4: A ptychography reconstruction as shown in Chapter 5 in the left two images. The middle two images show the reconstructed probes for the two illumination modes. The probes are heavily aberrated by the defects of the ellipsoidal mirror combined with misalignment which is not necessarily a problem for ptychography to deal with. The right two images represent the intensity distribution in the scanned area on the sample, computed with the reconstructed probe intensities and the scanning positions. The white contours mark the areas illuminated by 75% and 95% of the EUV photons.

D.2. LENSLESS IMAGING GALLERY WITH VISIBLE LIGHT IN REFLECTION MODE

A parallel lensless imaging system has been built for visible light, as discussed in Chapter 6, making experiments easier due to the lack of vacuum requirements. Numerous experiments in reflection and transmission were conducted, with selected results shown in figure captions. A replica of the EUV sample from Chapter 5 was upscaled to optical wavelengths (about 30 times larger). The gold layer on the silicon wafer is 50 nm thick, resulting in low phase contrast but high amplitude contrast due to the absorption properties of gold and silicon in the visible range.

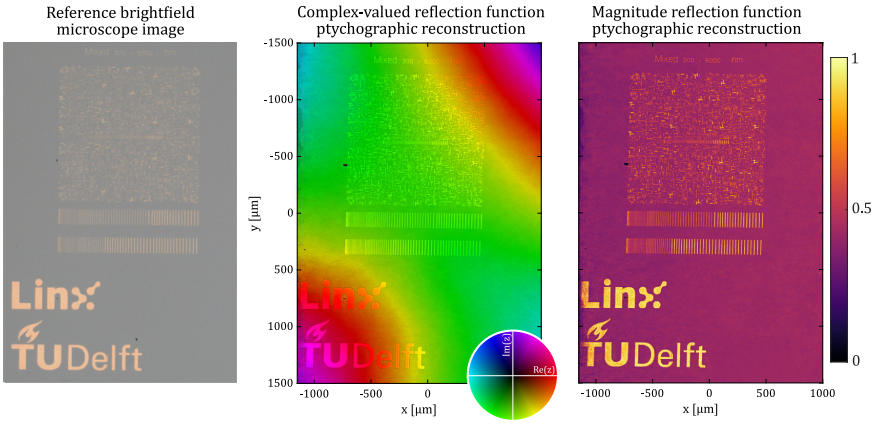

Figure D.5: Mixed 'Manhattan'-like structures, a chirped grating and the logo of LINX and the TU Delft are patterned on top of a silicon wafer. A ptychography scan has been performed in reflection at 45 degrees angle of incidence using light with a wavelength of 660 nanometer. The reconstruction compares well to the conventional brightfield microscope image on the left.

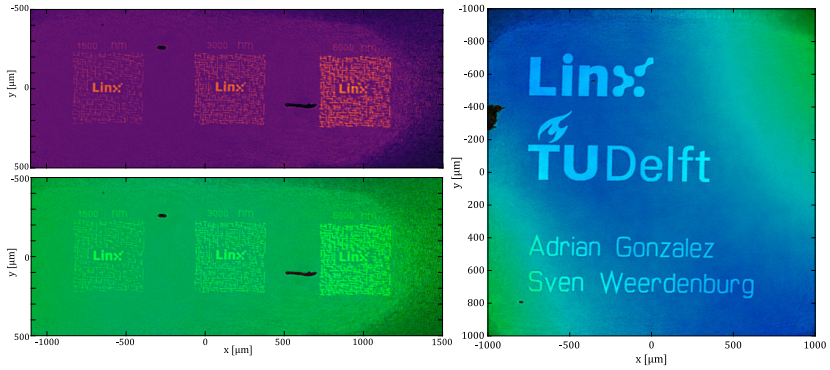

Figure D.6: Another scan has been performed on the same sample but of different regions. The LINX logo is surrounded by Manhattan-like structures with different linewidths from 1.5 micron up to 6 micron with a NA of 0.18.

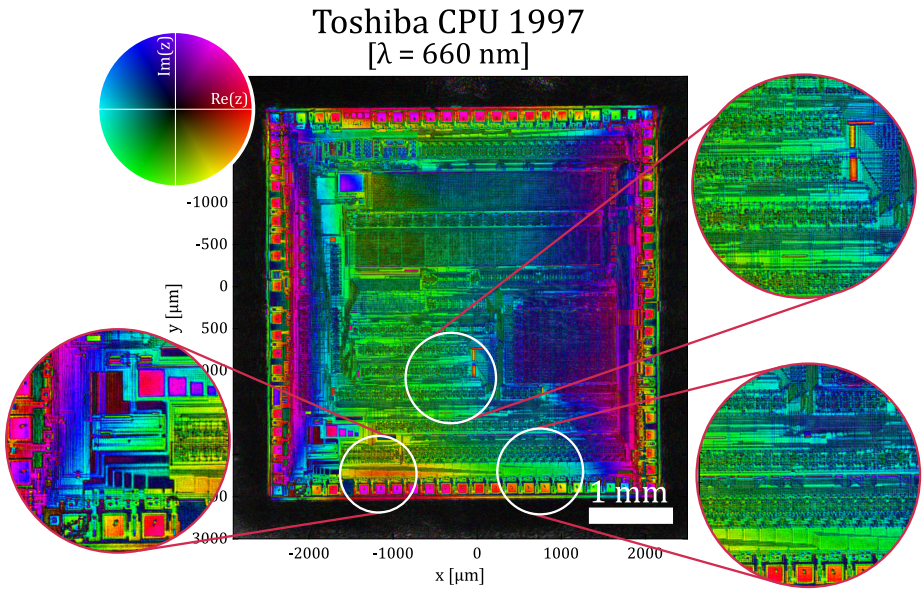

Figure D.7: A 5x5 mm Toshiba chip die (1997) was scanned in reflection at a 45-degree incidence angle with 660 nm illumination. The reconstruction clearly shows circuit lines through phase (hue) and amplitude (intensity) information, with visible wire-bonding contact pads around the chip's perimeter. A global phase profile reveals a non-flat surface across the chip.

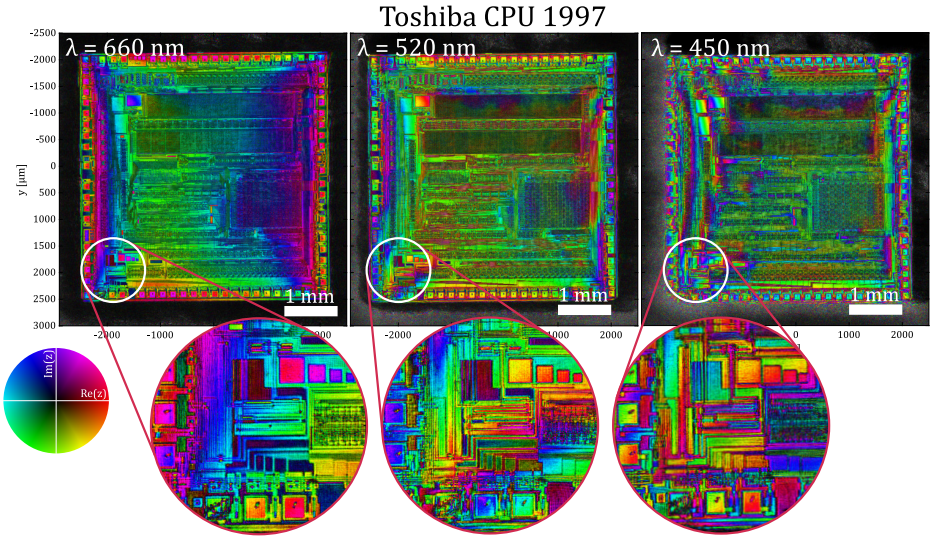

Figure D.8: The chip was scanned separately with three different wavelengths: 660 nm, 520 nm, and 450 nm. The global phase wraps across the sample increase with the wavelength.

D.3. LENSLESS IMAGING GALLERY WITH VISIBLE LIGHT IN TRANSMISSION MODE

The visible light setup as shown in Chapter 5 can be easily configured to a transmission setup by swapping the sample holder. The sample holder can magnetically hold a microscope slide which can be scanned in x and y. Most of the figures below are reconstructions from experimental datasets on this setup using commercially available prepared microscope slides and test targets.

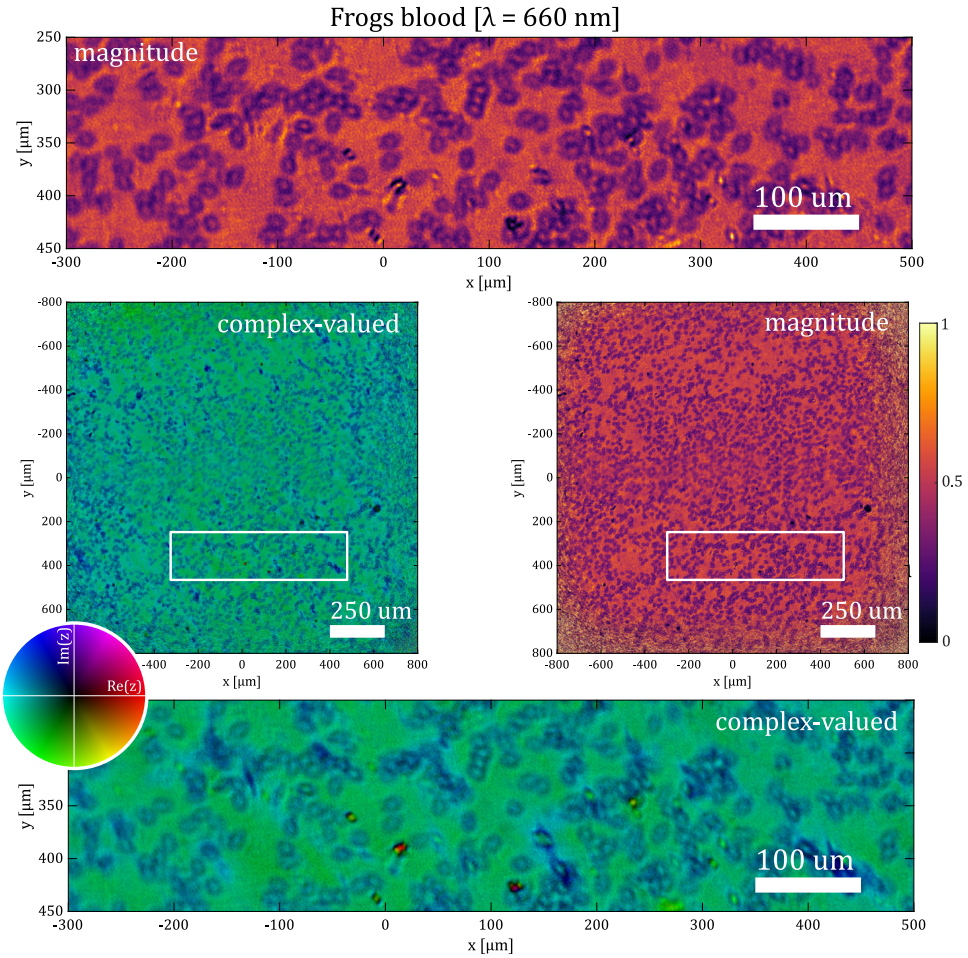

Figure D.9: Frog blood cells have been scanned in a 800 by 800 micron region with a illumination probe with a wavelength of 660 nanometer. The reconstruction of the entire region is shown in the center row. The two images represent the reconstruction in amplitude and phase (complex valued) and amplitude only. The top and bottom show a close up within the white boxes, clearly showing the individual blood cells. There does seem to be an artifact present in the center of the large field of view, where a blurry 'copy' seems to be present. The origin of this effect is not really understood, which would require further investigation.

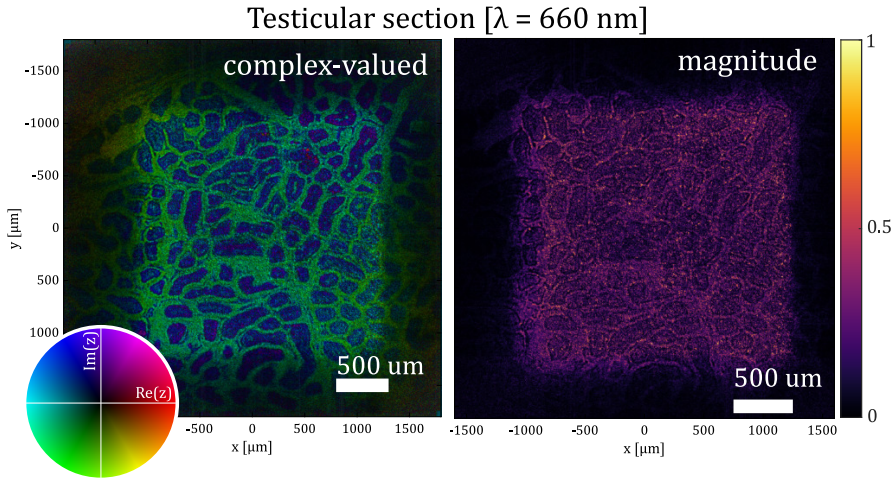

Figure D.10: A testicular section has been scanned in transmission. The target has a very low amplitude contrast as shown in the reconstructed magnitude image on the right. However, as we also retrieve the phase with ptychography we can observe a strong contrast in the complex-valued image (the hue equals phase and brightness the amplitude) on the left.

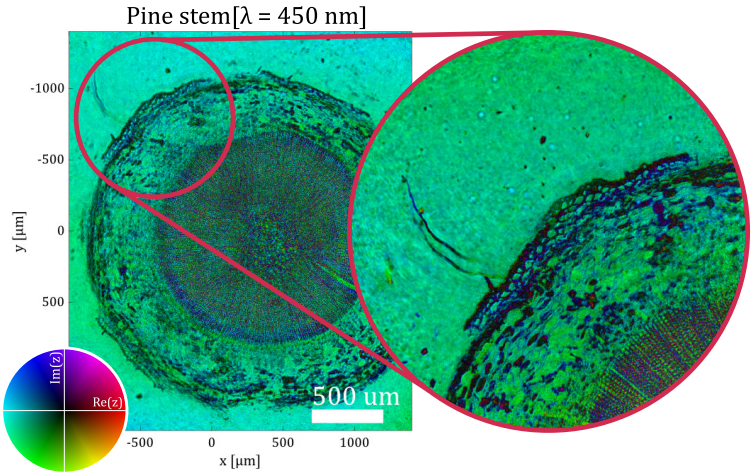

Figure D.11: A complex-valued reconstruction of a pine stem in transmission with blue light with a wavelength of 450 nanometer. The center ring consists of tiny tubes of 5 micron in diameter which transport water through the stem.

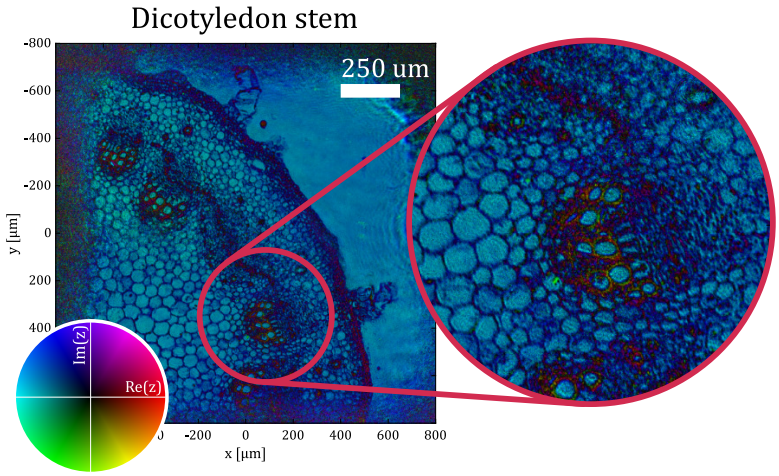

Figure D.12: A reconstruction of a dicotyledon stem in transmision with 450 nanometer of light. The individual structural cells in the stem can be observed. More phase contrast (yellow and purple colors in the cell walls) can be observed in the vascular bundles as shown in the inset.

CURRICULUM VITÆ

Sven Weerdenburg

18-05-1995 Born in Zoetermeer, The Netherlands.

EDUCATION

Sep '12–June '16 **Bachelor of Science (BSc)**, cum laude, Engineering Physics
Thesis: Characterization of hyperspectral imaging systems for earth observations
The Hague University of Applied Sciences, The Netherlands

Sep '16–June '17 **Premaster**, Applied Physics
Delft University of Technology, The Netherlands

Sep '17–Sep '19 **Master of Science (MSc)**, Applied Physics
Thesis: Optical phase retrieval through two color reflectometry
Delft University of Technology, The Netherlands

Oct '19–Mar '24 **Doctor of Philosophy (Ph.D)**., Applied Physics
Delft University of Technology, The Netherlands

Thesis: A lensless approach to semiconductor metrology with Extreme UV through High Harmonic Generation
Promotor: Prof. dr. W.M.J.M. Coene
Copromotor: Prof. dr. H.P. Urbach

INDUSTRY

2015 **Airbus Defence and Space Netherlands, Leiden**
Thermal engineering internship - Multilayer insulation

2016 **Cosine measurement systems, Warmond**
Remote sensing internship - HyperScout sattelite

2016–2019 **Mapper Lithography, Delft**
Part-time student employee - Wafer table engineering

2024 **Bright Society, Eindhoven**
Design engineer at ASML

LIST OF PUBLICATIONS

Peer-reviewed publications

4. **S. Weerdenburg**, Y. Shao, W. Coene, *Positional intensity correction in ptychography*,(2025).[submitted]

3. S. Senhorst, Y. Shao, **S. Weerdenburg**, R.C. Horsten, C.L. Porter, W. Coene, *Mitigating tilt-induced artifacts in reflection ptychography via optimization of the tilt angles*, Optics Express (2024)

2. **S. Weerdenburg**, R.C. Horsten, W. Coene, *Pressure profile retrieval of gas jets through Schlieren for EUV High Harmonic Generation applications*, (2024).[submitted]

1. Y. Shao[†], **S. Weerdenburg**[†], J. Seifert[†], H.P. Urbach, A.P Mosk, W. Coene, *Wavelength multiplexed Multi-mode EUV Reflection Ptychography based on Automatic-Differentiation*, Light: Science & Applications, Nature Publications (2024).

† = equal contributor

Non peer-reviewed publications

3. **S. Weerdenburg**, Y. Shao, W. Coene, *Automatic focusing of EUV mirror through sensitivity analysis for lensless imaging applications*, arXiv (2025).

2. **S. Weerdenburg**, R.C. Horsten, W. Coene, *Lossless EUV and Soft X-Ray photonflux sensing in optical surfaces*, arXiv (2024).

1. [†]**S. Weerdenburg**, *Coherent diffractive imaging: a lensless approach to EUV and Soft X-Ray Microscopy (article)*, Dutch Society for Precision engineering (DSPE) Journal: Mikroniek Nr.4 (2022).

† = published as cover article

Proceedings and conference talks

7. **S. Weerdenburg**, Y. Shao, S. Senhorst, R.C. Horsten, W. Coene, *Wafer metrology using automatic differentiation ptychography on an EUV High Harmonic Generation platform*, PTB VUV & EUV metrology conference, Berlin, Germany (2023).

6. **S. Weerdenburg**, Y. Shao, R.C. Horsten, W. Coene, *Wafer metrology using automatic differentiation ptychography on an EUV High Harmonic Generation platform*, International Microscopy Congress, Busan, South Korea (2023).

5. **S. Weerdenburg**, Y. Shao, R.C. Horsten, W. Coene, *EUV diffractive imaging in reflection for wafer metrology using HHG source and automatic differentiation based ptychography*, Optica Imaging Congress, Boston, USA (2023).

4. **S. Weerdenburg**, Y. Shao, R.C. Horsten, W. Coene, *EUV diffractive imaging for wafer metrology with HHG source using automatic differentiation based ptychography algorithm*, Face2Phase, Delft, The Netherlands (2022).

3. M. Tschernajew, S. Hädrich, R. Klas, M. Gebhardt, R. Horsten, **S. Weerdenburg**, S. Pyatchenkov, W. Coene, S. Breitkopf, J. Rothhardt, T. Eidam, J. Limpert, *Ultra-high photon flux high-harmonic generation*, Optica High-brightness Sources and Light-driven Interactions Congress, Budapest, Hungary (2022).

2. **S. Weerdenburg**, Y. Shao, R.C. Horsten, W. Coene, *Reflection Ptychography via Auto Differentiation on a High Harmonic EUV beamline*, Optica High-brightness Sources and Light-driven Interactions Congress, Budapest, Hungary (2022).

1. M. Tschernajew, S. Hädrich, R. Klas, M. Gebhardt, R. Horsten, **S. Weerdenburg**, S. Pyatchenkov, W. Coene, S. Breitkopf, O. Herrfurth, J. Rothhardt, T. Eidam, J. Limpert, *High repetition rate high harmonic generation with ultra-high photon flux*, OSA Laser Congress 2020 (ASSL, LAC), Quebec, Canada (2020).

Poster presentations

8. **S. Weerdenburg**, Y. Shao, R.C. Horsten, W. Coene, *EUV diffractive imaging in reflection for wafer metrology using HHG source and automatic differentiation based ptychography*, NWO Physics at Veldhoven 2021.

7. **S. Weerdenburg**, Y. Shao, R.C. Horsten, H.P. Urbach, W. Coene, *EUV diffractive imaging in reflection for wafer metrology using HHG source and automatic differentiation based ptychography*, Dutch Society of Precision Engineering - Gala 2023.

6. **S. Weerdenburg**, Y. Shao, R.C. Horsten, W. Coene, *Reflective lensless microscopy with a tabletop High Harmonic Generation Coherent EUV source*, Dutch Society of Precision Engineering - Conference 2023.

5. **S. Weerdenburg**, Y. Shao, J. Seifert, R.C. Horsten, W. Coene, *EUV diffractive imaging in reflection for wafer metrology using HHG source and automatic differentiation based ptychography*, Optics Netherlands Event ASML 2022.

4. **S. Weerdenburg**, Y. Shao, R.C. Horsten, W. Coene, *Reflective Lensless Microscopy with a Table-Top High Harmonic Generation EUV Source*, Dutch Photonics Event 2023.

3. **S. Weerdenburg**, Y. Shao, R.C. Horsten, W. Coene, *EUV diffractive imaging in reflection for wafer metrology using HHG source and automatic differentiation based ptychography*, QUNOM 2023.

2. **S. Weerdenburg**, Y. Shao, R.C. Horsten, H.P. Urbach, W. Coene, *EUV wafer metrology via reflective ptychography with a High Harmonic Generation Source*, AMO, Egmond aan Zee, Netherlands 2023.

1. **S. Weerdenburg**, Y. Shao, R.C. Horsten, W. Coene, *Reflective Lensless Microscopy with a Table-Top High Harmonic Generation EUV Source*, Dutch Optics Kick-Off event, Netherlands 2020.

Other

3. **S. Weerdenburg**, † *2nd Place - OPTICA (OSA) yearly photo contest 2022*, OPTICA (OSA) - Optics & Photonics 2022.

2. *A lensless approach to EUV and soft X-ray microscopy (news item)*, Dutch Society for Precision engineering (DSPE) Journal news.

1. *TU Delft builds EUV-based metrology tool*, Bits & Chips December 2021.

† = photo of the high harmonic generation system, as used for the thesis cover